Tricks and tips for faster small-scale swimming: Complex fluids and elasticity

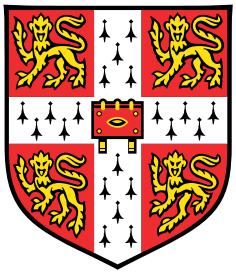

Emily E. Riley

Department of Applied Mathematics and Theoretical Physics
University of Cambridge

This dissertation is submitted for the degree of
Doctor of Philosophy

Magdalene College

September 2017

Declaration

This dissertation is submitted for the degree of Doctor of Philosophy. I hereby declare that this dissertation is the result of my own work and includes nothing which is the outcome of work done in collaboration except as declared in the Acknowledgements and specified in the text. It is not substantially the same as any that I have submitted, or, is being concurrently submitted for a degree or diploma or other qualification at the University of Cambridge or any other University or similar institution. I further state that no substantial part of my dissertation has already been submitted, or, is being concurrently submitted for any such degree, diploma or other qualification at the University of Cambridge or any other University or similar institution.

Emily E. Riley
September 2017

Acknowledgements

First and foremost, I would like to acknowledge and thank my supervisor Eric Lauga, for his continuous support, and his unwavering positivity through my almost constant frowning or worrying. He has supported me greatly with ideas and advice, and was always willing to help. Secondly, I would like to thank my collaborator Debasish Das, whose ability to code ceaselessly, lead to successful results presented in the penultimate chapter of this thesis. Furthermore I thank the EPSRC for funding this thesis.

Additionally I would like to thank all of the Biological Physics and Mechanics group, past and present, for all the illuminating presentations and helpful questions at Biolunches. I am grateful for the helpful comments and suggestions in ad-hoc discussions by the kettle or over lunch. Additional thanks to the friends and fellow group members who proof read chapters of my thesis: Tamsin Spelman, Pierre Haas, François Peaudecerf, Kirsty Wan and Francesco Boselli.

Finally I would like to thank the people in my life who have indirectly contributed to my doctorate. Firstly, my partner Alex for listening to each of my post-work day analyses and much needed cups of tea. Secondly all those at MAUL, for their encouragement and the confidence that only a stack of broken boards can bring. Final thanks are to my parents for their unending support and love, and my friends, both near and far, for keeping me company in the trenches and on the dance-floor.

Abstract

Many cells exploit the bending or rotation of flagellar filaments in order to self-propel in viscous fluids. Often swimming occurs in complex, nonlinear fluids, e.g. mucus. Furthermore even in simple Newtonian fluids, if swimming appendages are deformable then locomotion is subject to fluid-structure interactions. The fundamental question addressed in this thesis is how exactly locomotion is impacted, in particular if it is faster or slower, with or without these effects.

First we study locomotion in shear-thinning and viscoelastic fluids with rigid swimming appendages. Following the introductory Chapter, in Chapter 2 we propose empirical extensions of the classical Newtonian resistive-force theory to model the waving of slender filaments in non-Newtonian fluids, based on experimental measurements for the motion of rigid rods in non-Newtonian fluids and on the Carreau fluid model. We then use our models to address waving locomotion in shear-thinning fluids, and show that the resulting swimming speeds are systematically lowered – a result which we are able to capture asymptotically and to interpret physically. In Chapter 3 we consider swimming using small-amplitude periodic waves in a viscoelastic fluid described by the Oldroyd-B constitutive relationship. Using Taylor's swimming sheet model, we show that if all travelling waves move in the same direction, the locomotion speed of the organism is systematically decreased. However, if we allow waves to travel in two opposite directions, we show that this can lead to enhancement of the swimming speed, which is physically interpreted as due to asymmetric viscoelastic damping of waves with different frequencies. A change of the swimming direction is also possible.

Secondly we consider the affect of fluid-structure interactions. In Chapter 4, we use Taylor's swimming sheet model to describe an active swimmer immersed in an Oldroyd-B fluid. We solve for the shape of an active swimmer as a balance between the external fluid stresses, the internal driving moments, and the passive elastic resistance. We show that this dynamic balance leads to a generic transition from hindered rigid swimming to enhanced flexible locomotion. The results are physically interpreted as due to a viscoelastic suction increasing the swimming amplitude in a non-Newtonian fluid and overcoming viscoelastic damping. In Chapter 5 we consider peritrichously flagellated bacteria, such as *Escherichia coli*. The rotation of each motor is transmitted to a flexible rod called the hook which in turns transmits it to a helical filament, leading to swimming. The motors are randomly distributed over the body of the organism, and thus one expects the propulsive forces from the filament to almost cancel out leading to negligible swimming. We show that the transition to swimming is an elasto-hydrodynamic instability arising when the flexibility of the hook is below a critical threshold.

Table of contents

1

Introduction

Micro-scale biological locomotion is crucial. From finding new food sources and evading predators for individual swimmers, to fertilisation and flow induction in multicellular organisms [1]; the generation of fluid flows at the micro-scale is an important and interesting field of study, dating all the way back to the advent of the microscope and the first observations of bacteria and spermatozoa by van Leeuwenhoek [2].

Below the millimetre scale, viscous effects tend to dominate and macro-scale methods of propulsion that rely on inertial momentum transfer are often ineffective. This viscosity dominated regime is described mathematically by small values of the Reynolds number: the ratio of inertial to viscous forces. A variety of small prokaryotic (bacteria/archaea) and eukaryotic (animals/plants/algae) organisms exploit these viscous forces in order to self-propel. For continuous motion in this low-Reynolds world, a swimmer must move its body periodically and constantly expend work on the fluid, while doing so in a time irreversible manner to overcome the limits of the low Reynolds environment where flow is time-independent [3]. For swimmers with back-and-forth motion, the viscous drag during the power stroke must be greater than that during the recovery stoke, and it is this drag anisotropy that leads to locomotion. This is achieved, for example, by the rotation of rigid helical flagella filaments [4] or by the propagation of planar travelling waves along a flexible flagellum [5].

We begin with a short overview of the main modelling techniques with a focus on flagellar-based locomotion. Then, we introduce in further detail the two flagella types found in nature: the whip like eukaryotic flagella; and the rotary bacteria flagella. We finish with an overview of swimming in non-Newtonian fluids.

Fig. 1.1 Wild-type planar wave motion of *Caenorhabditis elegans* swimming in a bulk Newtonian fluid; (a) single image of *C. elegans* reprinted from Ref. [6], (b) overlaid images of *C. elegans* with swimming, and (c) a series of swimming strokes through a half-cycle, both (b) and (c) reprinted from Ref. [7].

1.1 Modelling flagella

Our fundamental understanding of swimming organisms has increased dramatically with the advancement of imaging techniques and computing power for more realistic numerical simulations [8]. We focus on flagellar-based locomotion for which there is a wealth of work, but we note that these flagellar-based modelling approaches are also applicable to whole-body undulations such as for the nematode *Caenorhabditis elegans* shown in Fig. 1.1, membrane motion, and biomimetic swimmers [8].

Taylor's swimming sheet [9] and Taylor's cylindrical swimmer [10] models consider small-amplitude perturbations of a sheet or cylinder away from a flat, zero-amplitude state. Both models represent the flagellar filament as an infinite swimmer (along the swimming direction) with periodic motion along its body. In Taylor's swimming sheet model planar wave motion is modelled by an infinite planar sheet with no head where deflections can either occur perpendicular to the sheet or along the sheet representing transverse and longitudinal waves respectively. Similarly for Taylor's cylindrical swimmer transverse and longitudinal waves are possible, where transverse modes are in the plane perpendicular to the cylinder axis and longitudinal modes are along the cylinder axis. The swimming speed is then calculated as a series expansion of the amplitude of the swimmer relative to its wavelength, with later extensions to arbitrarily large expansions [11]. Taylor's swimming sheet is confined to planar-wave motion due to its reduced dimensionality, whereas Taylor's cylindrical swimmer is applicable to three dimensional motion.

Beyond these infinite-swimming models, small-amplitude perturbations can also be considered on the surface of a sphere, namely the squirmer model [12]. These models allow calculation of the swimming speed of finite swimmers where the swimmer surface is covered in many short flagella, often termed cilia, that beat sequentially as

metachronal waves. The spherical squirmer model consists of a spherical body with a deformable surface such that the amplitude of these surface deformations is much smaller than the size of the swimmer. Originally proposed by Lighthill [13], subsequent improvements have been made and applied to ciliated surfaces where the tips of the cilia create the deformable surface [12]. A more detailed review and an application of the squirmer model is given in Ref. [14]. However, analytic results are still confined to small amplitudes. To escape this limit, we must move to asymptotically thin flagella.

Rod-like flagellar appendages are used by both eukaryotic [15] and prokaryotic [16] cells, as well as man-made swimmers [17], in order to induce propulsion in the absence of inertia. Due to the difference in drag coefficients for rods moving in a fluid perpendicular vs. parallel to their long axis, the time reversibility is effectively also broken for travelling wave-like motion of the appendages of swimmers, which allows for the generation of propulsion [18]. Although flexible planar wave motion of eukaryotes and rigid rotation of helical prokaryotic flagella evolved separately billions of years ago, they both take advantage of this anisotropy in drag via the large aspect ratio of their flagella [19].

In order to describe swimming induced by long, slender flagella, resistive-force theory was proposed over 60 years ago [20, 21] and has subsequently been improved upon [22]. The basic idea is to approximate the perturbation induced by the flagellum on the fluid as a line of flow singularities as point forces. For a radius of curvature of the flagellar waveform much larger than the diameter of the flagellum, and at leading-order in the aspect ratio of the flagellum, the local velocity linearly determines the local force density on the flagellum. The drag can then be decomposed into the perpendicular and parallel components in this local region [8, 23]. Corrections to resistive-force theory have been made to improve its accuracy by increasing the number of terms in the expansion, thereby analytically including hydrodynamic interactions between different portions of the flagellum in a systematic fashion [24, 25]. Further refinements include slender-body theory [22, 26], which provides greater accuracy leading to better qualitative and quantitative approximations [27] compared to resistive-force theory, but typically requires numerical evaluation.

While resistive-force theory is only valid asymptotically, and is only accurate logarithmically, it has been shown to be a good approximation in many instances [28]. Resistive-force theory provides analytical insight on the kinematics of swimming at large amplitudes, as relevant to real flagellar motion. For this reason, it provides good intermediary modelling between simple small-amplitude results and complex computations and has had great success in describing the locomotion of microorganisms in Newtonian fluids [29–31]. To escape these two asymptotic limits, the use of numerics

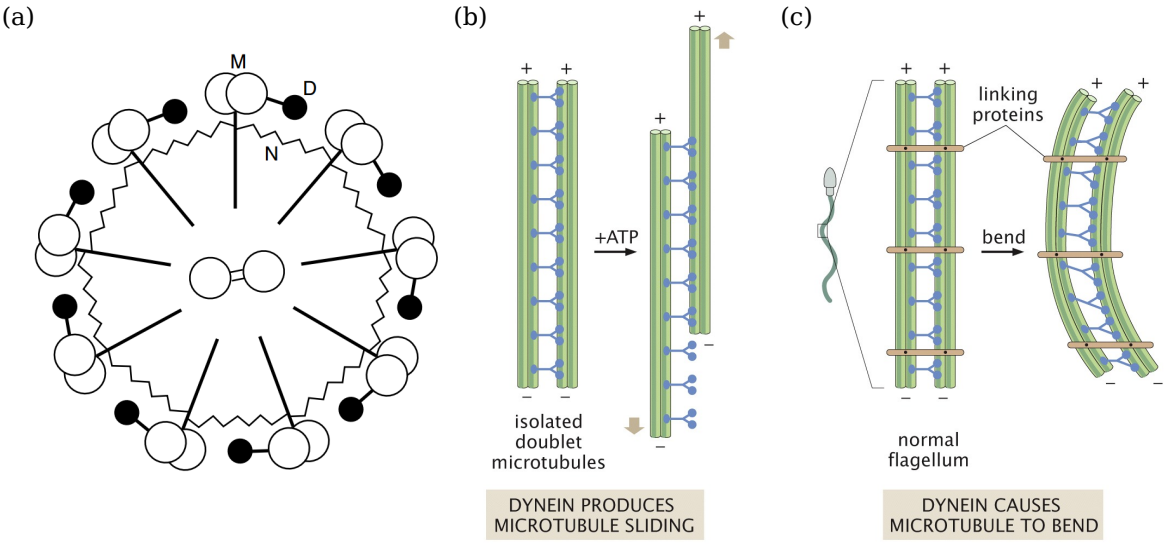

Fig. 1.2 The internal structure and force generation is shown: (a) Schematic of the eukaryotic flagellum axoneme: M labels the microtubule doublets, D the dynein motors and N the nexin springs (reprinted from Ref. [39]); schematic showing molecular motors (blue) stepping along microtubule doublets (green) based on doublet boundary conditions stepping produces either (b) sliding or (c) bending. Reprinted from Ref. [40]

is required. Boundary element methods [32, 33], bead-spring models and multi-particle collision dynamics [34] have all been used to model many different swimmers.

1.2 Eukaryotic flagella

Egg fertilisation [35], embryonic symmetry breaking [36] and airway clearing [37], imperative for our own eukaryotic existence and survival, all require flagellar-based low-Reynolds flow generation. Further away from our multi-organ mammalian world, eukaryotic flagella are used by algae, micro-plankton, and parasites [38]. There are two main types of eukaryotic swimming appendages, flagella and cilia. They are similar in structure hence are typically catagorised based on their length and number, with cilia being shorter and more numerous [38].

The structure of the flagellum is built from microtubules encased in an outer membrane. At the outer edge of the axoneme (flagellar cytoskeleton), each microtubule is linked to another creating a doublet. There are nine of these doublets at the outer perimeter of the flagella cross section, with spokes pointing towards two unlinked central microtubules [39]. This creates the aptly-named “9+2” axoneme, shown in Fig. 1.2. Actuation of flagella is generated by the action of molecular motors distributed along

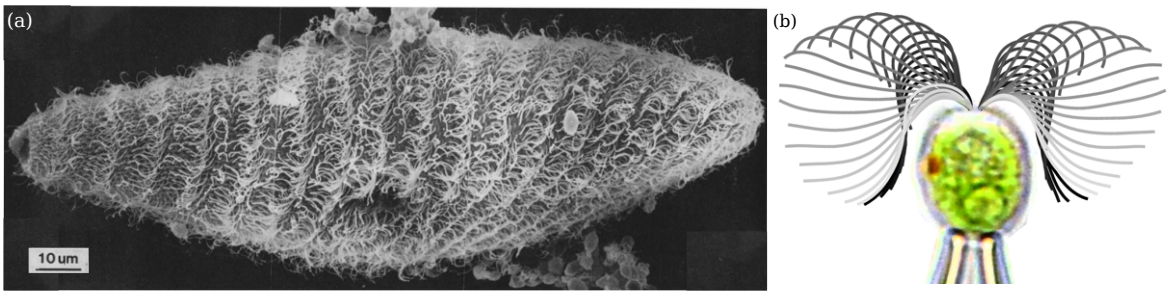

Fig. 1.3 (a) A scanning electron microscopy image of *Paramecium* showing that its surface is covered by many short cilia, reprinted from Ref. [41]. (b) *Chlamydomonas* uses its two leading flagella to pull itself through the fluid. The beat pattern is shown black to grey. Photo courtesy of K.Y. Wan.

the length of the flagellum. These dynein motors connect two outer doublets together and by stepping, they slide the doublets relative to each other. Due to the fixed-end condition, this sliding causes the flagellum to bend [39]. This same actuation can lead to many different flagellar beats, including planar wave swimmers and helical waves. Different flagellar gaits have also been observed on the same swimmer, depending on its environment [38].

Flagellated swimmers typically have one or two flagella, compared to ciliates (Fig. 1.3a) that can have thousands of cilia [8]. The most widely studied flagellar swimmers include the green alga *Chlamydomonas* (Fig. 1.3b) which has two flagella that pull the cell forward through the fluid, and spermatozoa (Fig. 1.4) that have one flagellum located at their ends that pushes the head forward. We focus here on swimming with a single flagellum for which there are two main approaches one can take.

Firstly, by considering the shape of the swimmer as fixed in the flow, the swimming speed is calculated via hydrodynamics only, this is termed rigid swimming. By matching the shape of the swimmer to waveforms found experimentally, good agreement has been found between resistive-force theory calculations and spermatozoa swimming [21]. As experimental techniques improve, we gain more accurate flagellar waveforms in two and three dimensions [43] to insert into these rigid-swimmer models. As well as empirically modelling flagellar waveforms, these rigid swimmers have been used to explore optimal flagellar waveforms [32], swimming in complex fluids [44], and interactions with other swimmers [45].

Secondly, beyond this rigid limit, the flagellar motion can be calculated as a balance of the active internal stresses created by molecular motor forces, passive elastic stresses, and hydrodynamic drag forces [46]. Active swimming was first studied by Machin to

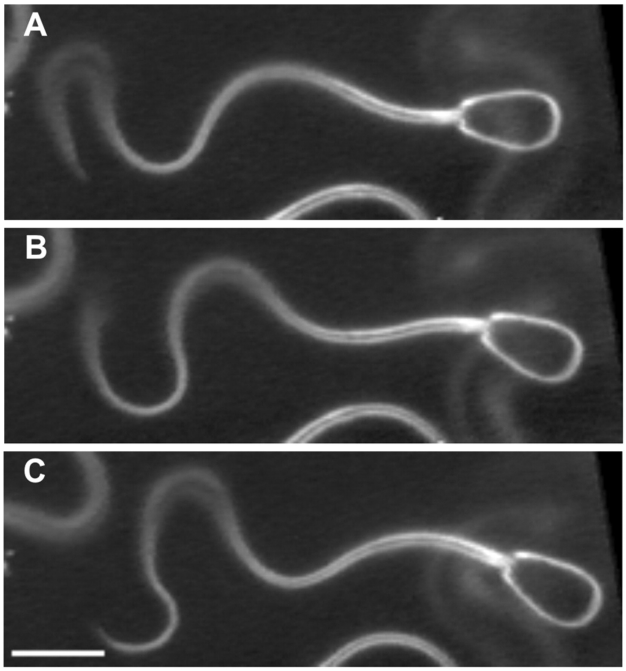

Fig. 1.4 Three successive video images 200 ms apart, showing bend propagation in a typical singleton spermatozoon. scale bar 10 μm. Reprinted from Ref. [42].

predict that the observed flagellar waveforms are due to actuation along the whole length of the flagellum [47]. The simplest models ignore the details of the internal structure and force generation and treat the filament as a simple Euler–Bernoulli beam, with a sinusoidal internal actuation [8]. Subsequent improvements have been made to include more detailed modelling of the passive [48] and active [49] deformations. As in the rigid swimming model, extensions have been made to study optimisation [50], swimmer interactions [51] and motion in complex fluids [52]. But due to the fluid-structure interaction, there are further physical effects that can be probed, namely interactions with boundaries, external flow fields, and synchronisation with other swimmers [33, 43]. These models can be difficult to compare with biological swimmers as it is still unknown how the swimmer can modulate its beat based on its environment. Experimental studies have probed the actuation of planar wave swimmer *C. elegans* [53], and human spermatozoa [54] in fluids of varying viscosities, and shown little change in the swimming speed, whereas for a simple flexible swimmer we would predict a decrease in flagellar swimming speed due to reduced amplitude [55].

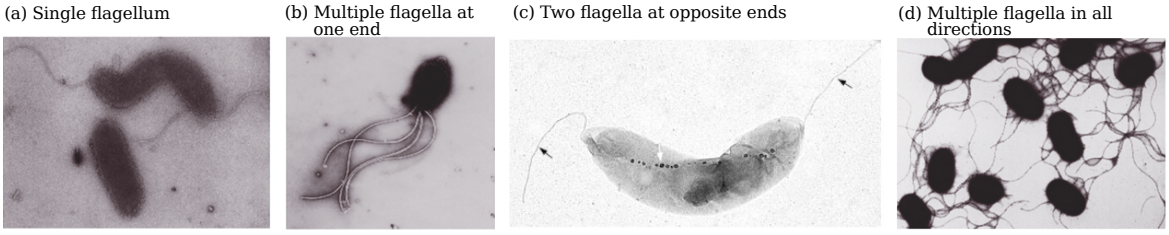

Fig. 1.5 Electron microscope image of different types of flagellar arrangement schemes (a) Monotrichous bacteria *e.g. Vibrio cholerae* and *Idiomarina loihiensis* (shown), (b) lophotrichous *e.g. Vibrio fischeri* (shown), (c) amphitrichous *e.g. Magnetospirillum magneticum* (shown) and (d) peritrichous *e.g. Escherichia coli* and *Salmonella enterica serovar Typhimurium* (shown). (a), (b) and (d) reprinted from Ref. [56] and (c) reprinted from Ref. [57].

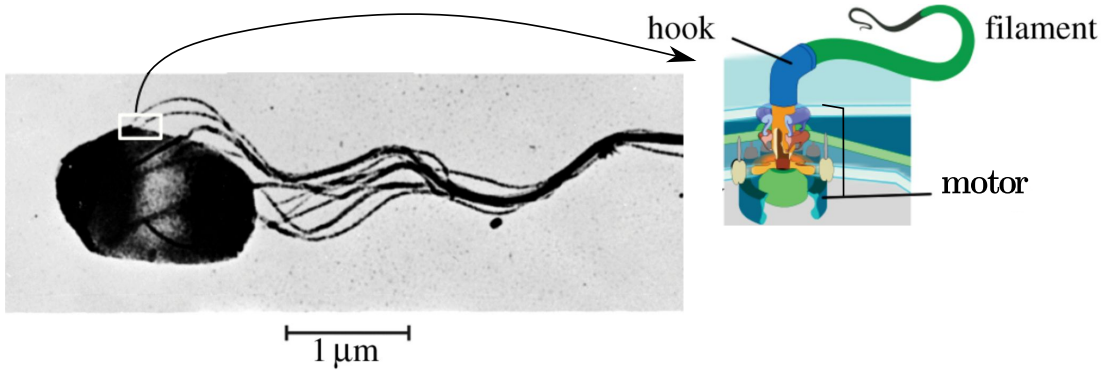

Fig. 1.6 Electron microscope image of *Salmonella* bacterium showing the bundle formed of many flagellar filaments. Each flagellar filament rotates due to the rotary motor embedded in the cell surface at its base, and these two components are connected via the hook. Reprinted from Ref. [62].

1.3 Bacteria

Bacteria dominate our planet. They are by far the most abundant and widely-spread organisms, with the ability to live in extreme and hostile environments [58]. Due to their large numbers they have the power to change our atmosphere [59], our soil, and even our bodies [58], despite their microscopic size. Hence many aspects of bacteria are widely studied.

Many bacteria propel themselves in order to respond to environmental cues. This is either achieved using surface forces at fluid-solid boundaries [60] or using rotary motors in bulk fluid environments [61], with the four flagellar arrangement types shown in Fig. 1.5. These rotary motors impose a torque normal to the surface of cell body. This torque is transmitted to the flagellar filament via a short elastic filament called

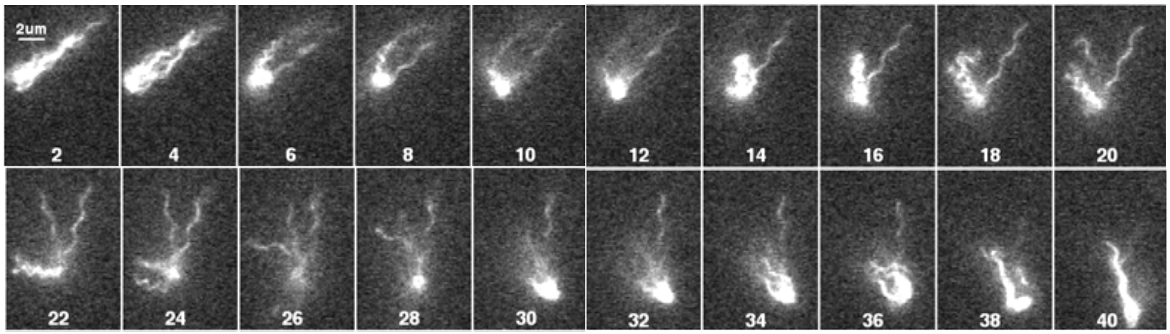

Fig. 1.7 Successive images of *E. coli* tumbling and the bacterium changes its direction. The time between the first and final image is ∼0.6 s. Reprinted from Ref. [65].

the hook, causing the filament to rotate, shown in Fig. 1.6. The hook is described as a universal joint as it is flexible against bending, but stiff against torsion [63, 64]. The helical nature of the flagellar filament means this rotation is time-irreversible and the bacteria is able to overcome the limits of its viscosity-dominated environment. The flagellar filament has eleven polymorphic forms, the "normal" swimming form of the helical filament is left-handed and rotates counter-clockwise (looking from the flagellum to the cell) propelling the swimmer cell-first [65, 66]. This type of swimmer is known as a pusher, as the trust force is generated behind the cell body, with fluid drawn in from the side of the cell and pushed out at either end of the cell [67]. Conversely, if the same left-handed helix were to rotate in the opposite direction then the cell would swim flagella first and be a puller, where fluid is pulled in at the head and tail of the swimmer and expelled at the sides, though this is confined to amphitrichous bacteria [57] (Fig. 1.5c).

Escherichia coli, *Bacillus subtilis* and *Salmonella typhimurium* are all pusher swimmers that have many helical flagella. The flagella typically gather or bundle at one end of the body during swimming. These bacteria are known as peritrichously-flagellated bacteria, shown in Fig. 1.5d, typically having 3 to 30 flagella, which can grow from any point on the cell body surface, and their distribution is somewhat random [68, 69]. The advantage of many flagella is not increased propulsion speed [70], but they facilitate direction changes through tumbling. This occurs when one or more of the rotary motors of the flagella slows down [71] or reverses its direction [65, 72] causing the bundle to break-up. When the motors return to their swimming state and the bundle reforms, the bacteria swims in a new swimming direction, as shown in Fig. 1.7. Through adapting their frequency of tumbling, bacteria are able to direct their motion towards more favourable environments.

Theoretical work on self-propelled bacteria has studied many different swimming behaviours including collective motion, interactions with surfaces, and swimming in non-Newtonian fluids [61]. For a free-swimming peritrichous bacteria there are two main modelling tactics: either the bundle is treated as a single flagellar filament, or the bundle is formed from a small number of filaments. For the first tactic the position of the flagellar "bundle" is fixed relative to the cell body. These helical swimmers have been modelled with resistive-force theory [73, 74] and slender-body theory [27], with the flagellar axis aligned with the swimming axis. Alternatively, for off-axis flagella motion, boundary element method has been used [75]. In studies modelling multiple flagella, the run-and-tumble motion of *E. coli* has been recreated and near-field flow fields captured both with bead-spring modelling [76] and multi-particle collision dynamics [77]. Both studies use typical *E. coli* swimmer parameters and include the polymorphic transformations that the bacteria flagella can undergo when under strain, *e.g.* from motor reversal [65, 66]. Further insights into the bundling process has been found by varying the motor torque on one of three total flagella and the distances between them, capturing the range of parameters for which the bundle is stable [34]. Boundary element methods are also able to recreate bundling and has been used to compare propulsive efficiency and energetic efficiency [78]. These multiple filament studies allow the flagellar filament to rotate relative to the cell body, via the bacteria hook.

Crucial for bundle formation and hence successful swimming is the hook. If the hook is stiffened then bacteria end up stuck in tumble positions and barely swim [79]. Furthermore macroscopic experiments on rotating helices show hook elasticity is crucial for helical filaments to synchronise and intertwine [80]. The hook flexibility has also been shown to be important for singly flagellated bacteria, causing unstable swimming if the hook is too flexible [81] and enabling a flicking motion for fast changes in swimming directions [82].

With this overview of the two main types of flagellar propulsion and the models used to study them, we are now equipped to review their motion in non-Newtonian fluids. Before this we will give a brief review of the non-Newtonian effects found in biological fluids.

1.4 Non-Newtonian fluids

Non-Newtonian fluids do not follow Newton's law of viscosity. The stress-deformation relationship is thus no longer a simple linear relationship between the stress and strain,

with the viscosity as the proportionality constant [83]. These nonlinear effects often arise when the molecules or particles immersed in the fluid are large enough or interact sufficiently their neighbours to affect the flow dynamics. Many biologically-relevant fluid environments have shear-dependent viscosities, and display elastic effects, since they contain proteins and other polymers. These non-Newtonian biological fluids include lung mucus, cervical mammalian mucus [84] and soil [85]. Studied in this thesis are shear-thinning fluid properties and viscoelastic fluid properties. We note that these two effects can often occur together, in particular in biological fluids [86].

Shear-thinning fluids are within the subset of generalised Newtonian fluids, where the linear stress-strain relationship is replaced by a nonlinear relationship. These fluids have no memory of the previous flow dynamics. For shear-thinning fluids, the viscosity decreases as the shear-rate is increased [83]. Shear-thinning fluids are typically modelled as a power-law or Carreau fluids. The simplest being a power law fluid model wherein the viscosity is proportional to the shear-rate to the power of the shear-thinning index. The shear thinning index is unity for a Newtonian fluid, less than unity for a shear-thinning fluid and greater than unity for a shear-thickening fluid. Although a power law model well describes some thinning behaviour it struggles to capture low and high shear rates. To avoid the viscosity tending to zero at large shear rates and to capture Newtonian behaviour at low shear-rates we move to the Carreau model. Here the viscosity is constant at small shear-rate until a critical shear-rate is reached. Once this critical shear-rate is reached the viscosity decreases (increases) as a power-law for shear-thinning (-thickening) fluids.

Viscoelastic fluids have elastic and viscous effects. These elastic effects arise from polymers immersed in the fluid that act as entropic springs. The combination of viscous and elastic effects thus means that the fluid can have a memory of past deformations [83, 87]. The simplest models consider spring and dash-pots connected in series (Maxwell model) or parallel (Kelvin–Voigt). Although these are useful models to capture certain fluid behaviors such as stress relaxation and creep, they are not connected to the microscopic structure of the fluid and hence only capture some viscoelastic fluid effects. To model the polymers immersed as a continuum fluid bead-spring dumbbells model the immersed polymers. These Oldroyd-B-like fluids can be rigorously derived from the microscopic details of the immersed dumbbells [87]. More complicated fluids models, such as Geisekus [87] and Phan-Thien-Tanner [83] fluids, consider both shear-thinning and viscoelastic effects. The motion of swimmers in these fluids creates stresses and strains that, due to the nonlinear effects of the fluid, can drastically alter the swimming kinematics.

1.5 Motion in non-Newtonian fluids

The vast majority of work on swimming at low Reynolds number has focused on swimmers moving in Newtonian fluids. However, *in vivo*, many self-propelled organisms progress through non-Newtonian fluids. Examples include the motion of cilia in lung mucus [37], nematodes travelling though soil [88], bacteria in their host's tissue [89], and spermatozoa swimming though cervical mammalian mucus [35]. An important question is how this transition from a Newtonian to a non-Newtonian fluid affects the dynamics and kinematics of micro-swimmers.

1.5.1 Falling in non-Newtonian fluids

The study of bodies moving in non-Newtonian fluids has a long and rich history. Analytical studies on the motion of rigid spheres in non-Newtonian fluids have been conducted using a variety of shear-thinning models including power-law [90], Carreau [91] and Ellis [92]. Although exact solutions can be found, the results reported from power-law fluid models often do not agree with one another, nor with experimental results [90]. Greater success and agreement with experiments has been obtained with the Carreau and Ellis fluid models [90]. Analytical studies in this case, expand the results about the Newtonian result with a small amount of non-Newtonian effects for the Carreau fluid and extremum principles for the Ellis model [91, 92], while numerical approaches required fitting external parameters to the data (*i.e.* Carreau [93]).

As studies branch away from rigid spheres in infinite fluids, the complexity of calculations increases again due to orientation considerations, and past theoretical studies mostly rely on numerics. In non-Newtonian fluid mechanics, empirical fitting is a key modelling approach. Due to the nonlinear nature of the fluid, parameters are often fit to certain shear-thinning indices, other rheological properties, or shape parameters, allowing prediction of behaviour in a variety of shear-thinning fluids. While it was shown analytically that the Stokes paradox vanishes for cylinders in power-law fluids [94], attempting to extend this to Carreau fluids has proved problematic. Furthermore, the majority of the work on rods and cylinders in non-Newtonian fluids has focused on small but finite Reynolds numbers, motivated by industrial applications. In the low Reynolds flow limit the drag coefficients calculated numerically show reduction compared to those calculated in a Newtonian fluid [95, 96], similar to experimental results [97], where both motion of cylinders orientated parallel and perpendicular to their motion was investigated. The role of the aspect ratio of cylindrical rods has been studied in inelastic and elastic fluids, showing that drag coefficients reduce by about one

order of magnitude over aspect ratios ranging from 1/150 to 1/10 [98]. Semi-empirical predictions yield qualitative agreement, but overestimate the drag coefficient [99, 100]. Comparable studies have also probed wall effects [95, 101], different cross-sections [102], and interactions between particles [103].

This thesis primarily studies shear-thinning and viscoelastic fluid effects. However there has also been a wealth of work on motion in a variety of other non-Newtonian fluid types. For example, enhanced swimming was predicted theoretically to take place in gels [104], yield stress fluids [105], phase separated fluids [106], and granular media [107]. Furthermore, swimming in inhomogeneous media with larger obstacles has been probed experimentally [108] and theoretically [109].

1.5.2 Swimming in viscoelastic fluids

Experimental studies have not yet reached a clear consensus on whether viscoelasticity increases or decreases swimming velocities. Instead a range of results has been reported for different kinematics and rheological properties. An experiment imitating Taylor's classic swimming sheet [9] in rotational (planar) geometry shows an increased locomotion in a Boger (constant-viscosity, elastic) fluid [110]. Similarly, the locomotion of flexible-tailed swimmers was also shown to be enhanced in a Boger fluid [111]. In contrast to these two studies, solutions of long flexible polymers with strong elasticity and no shear-thinning lead to a decrease in *C. elegans* swimming speed [112], and no change in the swimming speed of the bi-flagellate *Chlamydomonas reinhardtii* despite a change in swimming kinematics [113]. In the case of locomotion using helical flagella, small-amplitude helices always go slower, but for larger amplitudes, a modest increase is possible [114]. Furthermore, the motion of *E. coli* has been shown to be both enhanced [115] and hindered [116] in viscoelastic fluids. We note that for these experiments the bacterium size is comparable to that of the immersed elastic molecules, hence polymer details become more important compared to macro-scale rheology.

Previous theoretical studies addressing viscoelasticity have considered a variety of kinematics, including undulatory motion [44], helical rotation [117], squirming [118, 119], and three-sphere models [120]. Methods that are ineffectual in a Newtonian fluid due to reversibility [3], such as flapping [121] or solid body rotation [122], can also be exploited in a non-Newtonian setting to induce propulsion [123, 124].

Computationally the presence of a surrounding elastic structure, and non-Newtonian stresses were shown to lead to faster and more efficient swimming [125]. Numerical simulations also demonstrated that for high-amplitude motion polymeric Oldroyd-B fluids [117, 126, 127] could lead to faster locomotion. In these studies, enhanced swimming

has been predicted to occur as either due to end effects and stress singularities [126], or only for large-amplitude swimming [117]. In particular, using simulations on finite swimming sheets, it has been shown that front-back stress asymmetry together with swimmer flexibility leads to increased swimming speeds [127].

Analytical work on locomotion by waving focuses on small-amplitude motion. For a planar wave swimmer, asymptotic results in the case of prescribed rigid swimming predicted a systematic decrease of the swimming speed for all constitutive models, including all Oldroyd-like fluids [44] and general linear viscoelastic fluid models [128]. A decrease also occurs in the case of helical small-amplitude motion [52, 129]. An increase is however observed for rigid small-amplitude swimmers if there is a mixture of forwards and backwards modes (Chapter 3) [130, 131], and flexible swimmers (Chapter 4) [132]. Beyond these single swimmer studies, two nearby swimmers also synchronise faster in an elastic fluid than in a Newtonian medium [133], and the collective motion of swimmers is altered based on the swimmer and fluid properties [134, 135].

1.5.3 Swimming in shear-thinning fluids

Most theoretical studies of motion in shear-thinning fluids focus on small-amplitude asymptotics. This includes small-amplitude perturbations of a variety of swimming modes of Taylor's swimming sheet [84] and squirming motion on a spherical surface [136]. Of course, real biological swimmers fall beyond the asymptotic small-amplitude limit. In order to probe theoretically large-amplitude motion in non-Newtonian fluids, complex numerical simulations are required, such as those performed on a variety of swimmer types in shear-thinning fluids [137] and swimming of a sheet in a Giesekus fluid that has both shear-thinning and viscoelastic fluid effects [138]. Between these complex numerical simulations and small amplitude asymptotics, the waving motion of asymptotically thin rods show a decrease in swimming speed (Chapter 2) [139]. Beyond isolated swimmers, gliding bacteria near boundaries have been shown to increase their swimming speed with increasing shear-thinning effects [140], and migration of swimmers in shear-thinning fluids is slower than in Newtonian or shear-thickening fluids [141].

Experimental results again appear contradictory, and the enhancement or hindering of a swimmer depends on the exact details of the fluid and swimmer. *C. elegans* swimming has been studied in three different complex fluids. Firstly, a shear-thinning and viscoelastic fluid which showed a dramatic increase in swimming speed when the concentration of polymers was increased above a certain threshold value [142]. Secondly, in fluids where only shear-thinning effects were present in a rod-like polymer solution *C. elegans* was found to either have no change in swimming speed despite

a change in swimming kinematics [143] with a decrease in energy expended by the swimmer [144]. Conversely an increase in swimming speed was found in a shear-thinning colloidal suspension [145]. An experiment imitating Taylor's classic swimming sheet [9] in rotational (planar) geometry shows a decrease in a shear-thinning fluid [110]. In comparison helical swimmers were found to have increased propulsion speeds in shear-thinning fluids, which is attributed to soft confinement [146] akin to theoretical results [106, 138].

1.6 Thesis outline

The next three Chapters of this thesis study swimming in non-Newtonian fluids. In Chapter 2 we focus on shear-thinning fluid effects and propose empirical extensions of the classical Newtonian resistive-force theory to model the waving of slender filaments in non-Newtonian fluids, based on experimental measurements for the motion of rigid rods in non-Newtonian fluids and on the Carreau fluid model.

Chapters 3 and 4 concern viscoelastic fluid effects on the swimming of a two-dimensional sheet. We first consider a rigid swimmer and show that if all travelling waves move in the same direction, the locomotion speed of the organism is systematically decreased. However, if we allow waves to travel in two opposite directions, we show that this can lead to enhancement of the swimming speed. Secondly we solve for the shape of an active swimmer as a balance between the external fluid stresses, the internal driving moments, and the passive elastic resistance. We show that this dynamic balance leads to a generic transition from hindered rigid swimming to enhanced flexible locomotion.

Finally, returning to Newtonian fluids, in Chapter 5 we consider peritrichously flagellated bacteria, such as *E. coli*. We show that the tumbling to swimming transition is the result of an elasto-hydrodynamic instability. We end with a brief conclusion and suggestions for further work.

2

An empirical non-Newtonian resistive-force theory

2.1 Introduction

Prompted by the success of resistive-force theory and the biological relevance of non-Newtonian fluids, it is natural to ask if it would be possible to derive a resistive-force theory for nonlinear fluids. For the application of biological swimmers, the fundamental physical problem concerns the force generation by beating flagella. Physically, we expect that flagella waving in shear-thinning fluids will experience two important effects [146]. One is a local influence due to changes in the viscosity. If a body is subject to a Stokes-like force law and the viscosity of the fluid decreases, then the local force will decrease [97], and swimmers will then experience either enhanced or decreased locomotion based on the detailed balance between drag and thrust. The second effect, more subtle, is nonlocal and due to the change in the flow field around the body. Bodies moving in shear-thinning fluids are expected to be surrounded by low-viscosity regions, themselves embedded in high-viscosity domains. This thus makes swimming in a shear-thinning fluid akin to swimming under (soft) confinement, which might lead to an increase of propulsion [106, 147]. In this Chapter we propose a theoretical model for swimming in shear-thinning fluids addressing the first, local, effect by building an empirical extension of resistive-force theory to complex fluids. Specifically, and similarly to recent work in granular media [148], we propose to use experimental results on rods falling in shear-thinning fluids to obtain estimates on the drag coefficients acting along slender bodies (§2.2). We then quantify the impact of these coefficients on waving locomotion (§2.3) and compare our predictions with recent experiments on *C. elegans* (§2.4).

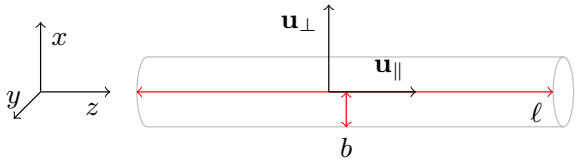

Fig. 2.1 A straight filament of length 2ℓ and cross-sectional radius b may translate in a fluid along its length (velocity $\mathbf{u}_\parallel$) or perpendicular to it ($\mathbf{u}_\perp$). The axis of the cylinder is along the $\hat{\mathbf{z}}$ direction while $\hat{\mathbf{x}}$ and $\hat{\mathbf{y}}$ are in the cross section.

2.2 Building a non-Newtonian resistive force theory

2.2.1 Methodology

The aim of this Chapter is to propose a new, nonlinear relationship between the velocity of a slender filament relative to a background fluid flow and the local hydrodynamic force density acting on it. We should point out at the outset that we are not deriving a rigorous mathematical model from first principles, as this is in fact virtually impossible due to the nonlinearity of the constitutive relationships, but instead seek to describe filament motion in shear-thinning fluids empirically.

Two approaches are used to calculate the non-Newtonian drag coefficients. The first one is an empirical fit to experimental measurements of sedimenting rods in shear-thinning fluids, and thus is directly built from experimental data. The second approach is an ad-hoc model based on the Carreau viscosity-shear-rate relationship. Since in shear-thinning fluids the shear viscosity of the fluid is a function of the shear-rate, we first need, in this case, a method to estimate accurately the local shear-rate around the moving filament. We do so by approximating the flow as locally Newtonian, allowing us to exploit elementary flow calculations. With this local, instantaneous value of the shear-rate, we can then incorporate the shear-thinning nature of the fluid though a correction to the Newtonian drag coefficients and therefore a nonlinear velocity-force relationship. For both approaches, we ensure that our methodology is consistent with the Newtonian limit and we carefully examine the limit in which we expect this approach to be valid.

2.2.2 Shear-rate around slender filaments

Newtonian flows near filaments

In order to estimate the shear-rates around moving filaments we make a locally-Newtonian assumption. To describe the drag on a slender filament we decompose the motion along the directions parallel and perpendicular to the local axis of the filament, leading to two drag coefficients. For simplicity consider a straight filament of cross-sectional radius b and length 2ℓ (Fig. 2.1). Following Lighthill's classical analysis [22], at leading order in the aspect ratio of the filament, the flow near the filament is described by a local, uniform line distribution of point forces and (potential) source dipoles along the centreline of the rod.

When the filament is translating along its symmetry axis, $\hat{\mathbf{z}}$, the flow around the cylinder is given by a linear distribution of point forces, with no need for dipoles, giving a relationship between the velocity field close to the filament, $\mathbf{u}_{\parallel}(x, y, z)$, and the force per unit length acting along the filament $f_{\parallel}\hat{\mathbf{z}}$, as [22]

$$\mathbf{u}_{\parallel}(x, y, z) = \frac{f_{\parallel}}{4\pi\eta_0}\left[\ln\left(\frac{4\ell^2}{r^2}\right) - 1\right]\hat{\mathbf{z}}, \tag{2.1}$$

where $r = \sqrt{x^2 + y^2}$ is the distance from the axis of the filament and η_0 is the Newtonian viscosity. At the surface of the cylinder $r = b$, the parallel drag coefficient, $c_{\parallel}$, is given by

$$\frac{f_{\parallel}}{u_{\parallel}|_{r=b}} \equiv c_{\parallel} = \frac{4\pi\eta_0}{\ln\left(4\ell^2/b^2\right) - 1}. \tag{2.2}$$

When the filament is translating perpendicular to its axis (here, the $\hat{\mathbf{x}}$ direction) then a combination of point forces and source dipoles are required to model the flow [22]. The velocity field near the filament is now given by

$$\mathbf{u}_{\perp}(x, y, z) = \frac{f_{\perp}}{8\pi\eta_0}\begin{pmatrix} \ln\left(\dfrac{4\ell^2}{r^2}\right) + \dfrac{b^2}{r^2} + \dfrac{2x^2}{r^2}\left(1 - \dfrac{b^2}{r^2}\right) \\ \dfrac{2xy}{r^2}\left(1 - \dfrac{b^2}{r^2}\right) \\ 0 \end{pmatrix}, \tag{2.3}$$

in the $(\hat{\mathbf{x}}, \hat{\mathbf{y}}, \hat{\mathbf{z}})$ coordinate frame where $f_\perp$ is the force acting on the filament per unit length. On the surface of the filament we have then

$$\mathbf{u}_\perp|_{r=b} = \frac{f_\perp}{8\pi\eta_0} \begin{pmatrix} \ln\left(\frac{4\ell^2}{b^2}\right) + 1 \\ 0 \\ 0 \end{pmatrix}, \tag{2.4}$$

i.e. the filament translates in the $\hat{\mathbf{x}}$ direction and the velocity is uniform around its surface. Similarly to the motion parallel to the filament axis the perpendicular drag coefficient, $c_\perp$, is given by

$$\frac{f_\perp}{u_\perp|_{r=b}} \equiv c_\perp = \frac{8\pi\eta_0}{\ln\left(4\ell^2/b^2\right) + 1}. \tag{2.5}$$

In order to extend these drag coefficients obtained for a straight filament to smooth curved filaments a relevant length ℓ over which the filament can be approximated as straight is required. In the application of resistive-force theory to travelling waves along sperm flagella, Gray and Hancock chose for ℓ the wavelength λ as the only relevant length scale along the swimmer but without mathematical justification [21]. In subsequent work, Lighthill showed mathematically by considering a periodic distribution of flow singularities that $\ell \approx 0.09\lambda$ was the relevant length scale along a periodic wave of wavelength λ [22]. This is the choice we make here to address waving motion with the understanding that other filament kinematics might require a different choice.

Shear-rates

In order to propose drag coefficients to use with the Carreau model (or any other shear-thinning empirical fluid model [83]) we require knowledge of the shear-rates in the fluid near the filament. In order to estimate shear-rates we again use Lighthill's calculations [22].

In case of parallel motion, we calculate the velocity gradient, $\nabla\mathbf{u}$, using Eq. (2.1). In cylindrical polar co-ordinates $(\hat{\mathbf{r}}, \hat{\phi}, \hat{\mathbf{z}})$ the only non-zero term is given by

$$\frac{\partial u_{z_\parallel}}{\partial r} = -\frac{f_\parallel}{2r\pi\eta_0}, \tag{2.6}$$

and thus the shear-rate tensor, $\dot{\boldsymbol{\gamma}}_{\parallel}$, is given by

$$\dot{\boldsymbol{\gamma}}_{\parallel} = -\frac{f_{\parallel}}{2r\pi\eta_0}\begin{pmatrix} 0 & 0 & 1 \\ 0 & 0 & 0 \\ 1 & 0 & 0 \end{pmatrix}. \tag{2.7}$$

For a filament moving locally in the direction perpendicular to its axis, the shear-rate tensor, $\dot{\boldsymbol{\gamma}}_{\perp}$, is obtained by taking the gradient of the flow in Eq. (2.3), such that

$$\dot{\boldsymbol{\gamma}}_{\perp} = \frac{f_{\perp}}{2r\pi\eta_0}\begin{pmatrix} \cos\phi(-1+b^2/r^2) & \frac{b^2}{r^2}\sin\phi & 0 \\ \frac{b^2}{r^2}\sin\phi & \cos\phi(1-b^2/r^2) & 0 \\ 0 & 0 & 0 \end{pmatrix}. \tag{2.8}$$

In order to capture how the viscosity changes near the filament, the total shear-rate near the filament is required. Indeed, a change in the viscosity due, for example, to a perpendicular motion will then affect the apparent viscosity for movement in the parallel direction, and vice versa. In other words, when the fluid is not Newtonian we can no longer consider perpendicular and parallel motions separately but need to include both solutions together. To find the total shear-rate, $\dot{\boldsymbol{\gamma}}_{tot}$, we exploit linearity and add the perpendicular and parallel solutions together to find on the filament $r = b$, the tensor

$$\dot{\boldsymbol{\gamma}}_{tot} = \frac{1}{2b\pi\eta_0}\begin{pmatrix} 0 & f_{\perp}\sin\phi & -f_{\parallel} \\ f_{\perp}\sin\phi & 0 & 0 \\ -f_{\parallel} & 0 & 0 \end{pmatrix}. \tag{2.9}$$

The first shear-rate invariant is zero at $r = b$, thus we calculate the second shear-rate invariant $|\dot{\boldsymbol{\gamma}}|^2 = \mathrm{tr}(\dot{\boldsymbol{\gamma}}^2)/2$ where tr refers to the trace of the tensor [83], such that

$$|\dot{\boldsymbol{\gamma}}|^2_{tot} = \frac{\sin^2\phi f_{\perp}^2 + f_{\parallel}^2}{(2b\pi\eta_0)^2}. \tag{2.10}$$

To find the average value of the shear-rate invariant around the surface of the cylinder we integrate around the cylinder axis (ϕ) and divide by 2π, and define the average shear-rate on the surface due to both perpendicular and parallel motion of the rod as

$$\dot{\gamma}_{avg} = \frac{\sqrt{f_{\perp}^2 + 2f_{\parallel}^2}}{2\sqrt{2}b\pi\eta_0}. \tag{2.11}$$

Note that beyond this local flow, hydrodynamic singularities far from the local portion of the filament also contribute to flow and shear-rates, but these will be at least $O(b/\ell)$

smaller, and are thus sub-dominant [22]. In the slender limit, the result in Eq. (2.11) gives therefore the leading-order value of the mean square shear-rate along the filament.

Finally, Eq. (2.11) relates the local shear-rate to the local force density. In order to be used in a resistive-force theory-type approach, we need instead to have a relationship between the shear-rate and the local velocity. To quantify the forces on the filament in a self-consistent fashion we write

$$f_\perp = c_\perp u_\perp, \text{ and } f_\parallel = c_\parallel u_\parallel, \tag{2.12}$$

and thus the average shear-rate around the rod is given by

$$\dot{\gamma}_{avg} = \frac{\sqrt{c_\perp^2 u_\perp^2 + 2c_\parallel^2 u_\parallel^2}}{2\sqrt{2}b\pi\eta_0}. \tag{2.13}$$

For a given velocity, we thus obtain that the locally-Newtonian assumption leads to a shear-rate independent of the viscosity, since both drag coefficients scale linearly with the viscosity (*i.e.* we get $\dot{\boldsymbol{\gamma}} \sim u/b$). We simplify the shear-rate by defining the shear-rate velocity as

$$u_{\dot{\gamma}} = \sqrt{u_\perp^2 + 2(c_\parallel^2/c_\perp^2)u_\parallel^2}, \tag{2.14}$$

such that

$$\dot{\gamma}_{avg} = \frac{c_\perp u_{\dot{\gamma}}}{2\sqrt{2}b\pi\eta_0}. \tag{2.15}$$

2.2.3 Notation

Depending on the model, shear-thinning fluids may be characterised by a number of rheological parameters. For example, for a Carreau-like fluid or a power-law-like fluid [83], one rheological parameter is the shear-thinning index, $0 < n < 1$, which describes by how much the viscosity reduces with increasing shear-rate ($n = 1$ being the Newtonian limit). A Carreau-like fluid is also characterised by the critical shear-rate, $1/\Gamma$, at which the fluid transitions from a Newtonian fluid, with viscosity η_0, to a shear-thinning fluid. In order to describe swimming through a non-Newtonian fluid, the Newtonian drag coefficients $(c_\parallel, c_\perp)$ are replaced by their non-Newtonian counterparts $(c_{NN_\parallel}, c_{NN_\perp})$. To quantify the non-Newtonian drag coefficients we introduce two correction factors, $(R_\parallel, R_\perp)$, defined as

$$R_\parallel = \frac{c_{NN_\parallel}}{c_\parallel}, \tag{2.16}$$

and,

$$R_{\perp} = \frac{c_{NN_{\perp}}}{c_{\perp}}. \tag{2.17}$$

If these drag coefficients are to describe motion in a shear-thinning fluid then they are likely to depend on the local shear-rate (and thus both local velocity and the Newtonian drag coefficients) in a nonlinear fashion, as well as on all the rheological parameters of the fluid and the geometrical parameters of the filament. We propose two empirical approaches in this paper, one based on experimental results and one based on the ad-hoc Carreau model. In order to distinguish between the correction factors in our two models below we use the subscript E to denote the correction factor derived from experiments while the subscript C will be used to denote the Carreau correction factor.

2.2.4 A non-Newtonian resistive-force theory from empirical data

We build our first empirical resistive-force theory from the experimental results of Ref. [97]. In this study, measurements were made of the sedimentation speed of rigid rods under gravity into a variety of fluids at low Reynolds numbers ($0.01 < \mathrm{Re} < 0.27$ based on their terminal velocity). The orientation of the rods was either aligned with gravity or perpendicular to it. The forcing from gravity is known and velocities are measured, allowing access to the drag coefficients. The rods used are a variety of materials (perspex, polyvinyl chloride, aluminium and stainless steel) with aspect ratios, $\alpha = d/L$, ranging from 1/10 to 1, where L is the rod length and d is the rod diameter. The non-Newtonian fluids in which the rods are dropped are shear-thinning viscoelastic fluids, with critical times ranging from 0 s$< \Gamma <$ 19 s, and shear-thinning indices spanning $0.6 < n < 1$ [97]. Rheometry data from Ref. [97] shows that the viscosity vs. shear-rate relationship for each of the five fluids probed can be described by the Carreau model, however they have non-zero first normal stress differences.

All results from Ref. [97] are reproduced in Fig. 2.2 where both perpendicular and parallel rod orientations are shown for all five non-Newtonian fluids. No systematic impact of the orientation of the rod on the experimental results is evident (specifically the change in the sedimentation velocity, i.e. the correction factor), suggesting therefore that correction factors are approximately independent of orientation in these experiments, $R_{E_{\perp}} \approx R_{E_{\parallel}} \equiv R_E$. Based on their data, the authors of Ref. [97] proceeded to

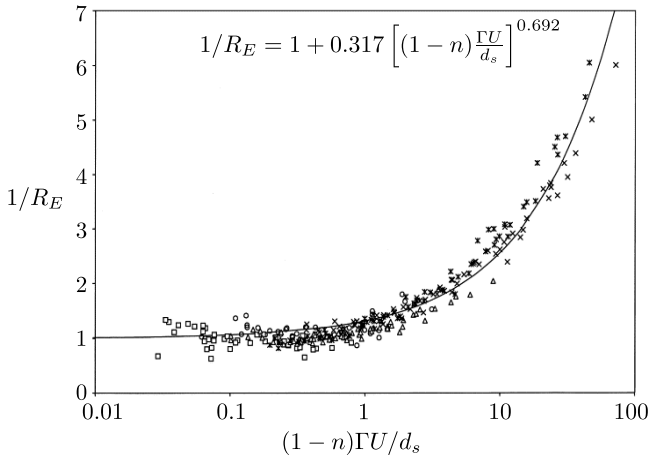

Fig. 2.2 Inverse of the drag coefficient correction factor, R_E, as obtained experimentally by measuring the sedimentation speed of cylindrical rods under gravity in a variety of shear-thinning fluids [97]. Results from both vertical ($\parallel$) and horizontal ($\perp$) rod orientations are shown and different fluids are marked by different symbols. Here n is the power index of the fluid, Γ^{-1} the critical shear-rate for transition to shear-thinning behaviour, U the velocity of the rod, and d_s a relevant length scale characterising the rod (see text). Inset: empirical formula, Eq. (2.18), proposed to fit all data [97]. Adapted and reprinted from Ref. [97].

propose an empirical formula fitting their data, namely a correction factor R_E given by

$$\frac{1}{R_E} = 1 + 0.317\left[(1-n)\Gamma\frac{|\mathbf{u}|}{d_s}\right]^{0.692}, \tag{2.18}$$

where n and Γ are as defined earlier, $|\mathbf{u}|$ is the magnitude of the rod velocity and $d_s = \sqrt[3]{3Ld^2}$ is the equivalent sphere diameter of the rods. From Ref. [97] the average error between their data points and the empirical best-fitting curve is 12%.

Based on this, we use the fit from Eq. (2.18) as our first empirical resistive-force theory in non-Newtonian fluids. Specifically we write that the non-Newtonian drag coefficients are given in this case by

$$c_{E_\perp} = R_E(|\mathbf{u}|)c_\perp, \quad c_{E_\parallel} = R_E(|\mathbf{u}|)c_\parallel, \tag{2.19}$$

and we choose $L = \ell$, in-keeping with the calculation of the shear-rate and the derivation of the Newtonian drag coefficients, in the expression for the effective rod diameter used in Eq. (2.18). Importantly, we note that Eq. (2.19) is fully consistent with Newtonian resistive-force theory in that for $n = 1$, or $\Gamma = 0$, we recover the Newtonian solution. Furthermore, Eq. (2.19) is consistent with experimental data shown in Fig. 2.2.

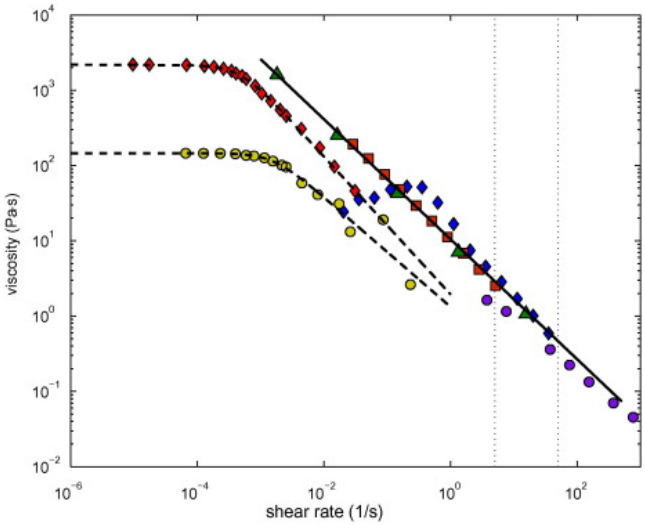

Fig. 2.3 Shear-thinning viscosity of mucus from published data. A variety of different mucus types including human cervical mucus, human lung mucus, human cervicovaginal mucus, pig small intestine mucus, and human sputum from a variety of different rheology measurement techniques including steady and oscillatory measurements and micro-rheology measurements. Reprinted from Ref. [84].

2.2.5 A non-Newtonian resistive-force theory from the Carreau model

We now attempt to build the second correction factor from a shear-thinning fluid model. We assume that the flow is locally Newtonian and thus we can employ the shear-rate from Eq. (2.15) in any shear-thinning fluid model. We confine ourselves to shear-thinning fluid models as our locally Newtonian assumption requires the fluid to have no memory of previous events. We choose the Carreau model which is a good fit to many biological shear-thinning fluids [84] (Fig. 2.3) and is used to fit rheology data microswimmer experiments in purely shear-thinning fluids [143]. In particular, we note that the shear-thinning data from all fluids in Ref. [97] fit well to the Carreau model. In a Carreau model, the viscosity of the fluid is given by

$$\eta = \eta_\infty + (\eta_0 - \eta_\infty)\left[1 + (\Gamma\dot{\gamma})^2\right]^{\frac{n-1}{2}}. \tag{2.20}$$

The model is well-behaved and shear-thinning for $0 < n < 1$. Here η_0 and η_∞ describe the fluid's Newtonian zero and infinite shear-rate viscosities, respectively. Since high

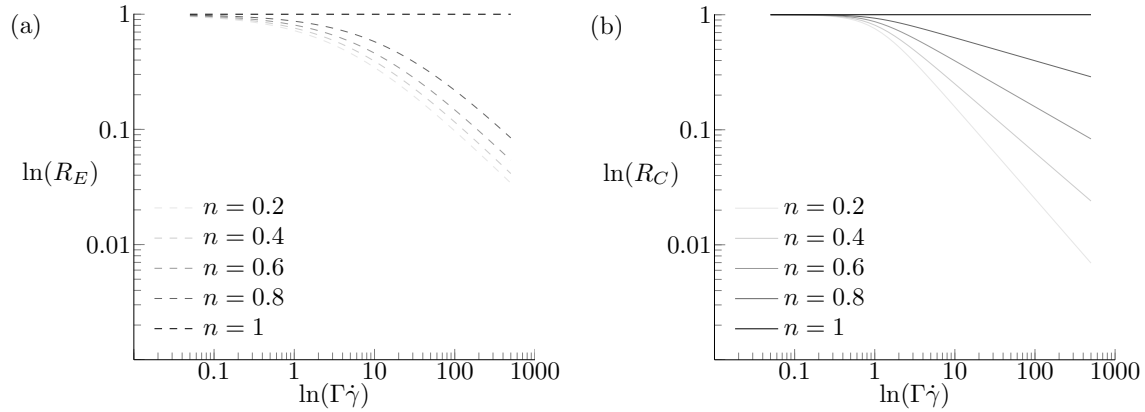

Fig. 2.4 Non-Newtonian correction factors as a function of the dimensionless flow shear-rate for the experimental results ((a) R_E) and the Carreau fluid model ((b) R_C). Increasing shear-thinning indices n are shown from light grey to dark grey with the Newtonian limit $n = 1$ shown in black.

shear-rates are unlikely to be reached, we set $\eta_\infty = 0$ so that the model simplifies to

$$\frac{\eta}{\eta_0} = \left[1 + (\Gamma\dot{\gamma}_{avg})^2\right]^{\frac{n-1}{2}}, \tag{2.21}$$

where $\dot{\gamma} = \dot{\gamma}_{avg}$. Together with Eq. (2.13), we describe the second correction factor as

$$R_C = \left[1 + \left(\frac{\Gamma c_\perp u_{\dot{\gamma}}}{2\sqrt{2}b\pi\eta_0}\right)^2\right]^{\frac{n-1}{2}}. \tag{2.22}$$

As a result, the Carreau non-Newtonian drag coefficients are defined by

$$c_{C_\perp} = R_C(u_\perp, u_\parallel)c_\perp, \quad c_{C_\parallel} = R_C(u_\perp, u_\parallel)c_\parallel, \tag{2.23}$$

with R_C from Eq. (2.22). Again, we note the Carreau correction factor is consistent with Newtonian resistive-force theory, and Eq. (2.19) reduces to unity when $n = 1$ or $\Gamma = 0$ to recover the Newtonian solution. Note that, contrary to the experimental non-Newtonian drag ratio, the Carreau maintains a difference between parallel and perpendicular orientations.

2.2.6 Comparison between the two models

We have proposed two methods to estimate non-Newtonian drag coefficients, one based on fitting experimental data (Eq. 2.19) and one based on using the classical empirical

Carreau model (Eq. 2.23). A comparison between the non-Newtonian correction factors for these two models is shown in Fig. 2.4 where we plot the correction factors as a function of the local dimensional shear-rate in the fluid (i.e. $\Gamma\dot{\gamma}$ for the Carreau model and $\Gamma|\mathbf{u}|/d_s$ in the case of the experiments). Both correction factors show the same qualitative behaviour decreasing with: an increased actuation shear-rate; an increased critical time Γ; and a reduced shear-thinning index n. As expected, the nonlinear dependence of R_C on n is stronger than the linear dependence in the case of R_E and there is thus a stronger reduction in drag with smaller values of n in that case.

Some important differences are however to be expected in the results. The empirical fit described by Ref. [97] was built from a small range of shear-thinning fluid parameters, thus in order to explore a wider range of n and Γ value we will push the experimental model past its true regime of validity. In comparison the Carreau fluid model is valid for all n and Γ values. We note also that Carreau fluids have zero first and second normal stress differences, whereas the fluids measure in Ref. [97] have non-zero first normal stress differences which increase with increasing shear rate indicating viscoelastic effects.

2.2.7 Regime of validity

The shear-rate calculated in Section 2.2.2 describes the local flow around the filament in the limit where it is asymptotically slender. In that case the relevant shear-rate near the rod is dominated by that induced by the local portion of the filament. In order for our local resistive-force theory to be self-consistent, the fluid viscosity around each section of the filament must only affected by the movement of said filament section. This requires the shear-rate at the cut-off distance ℓ away from the flagellum to be less than the critical shear-rate, $|\dot{\boldsymbol{\gamma}}_C| = 1/\Gamma$, at which the fluid becomes shear-thinning. The shear-rate scales as $\dot{\boldsymbol{\gamma}} \sim u_{\dot{\gamma}}/r$, hence the validity of our model is constrained to flows where

$$\frac{u_{\dot{\gamma}}}{\ell} \lesssim \frac{1}{\Gamma}. \tag{2.24}$$

For illustration purposes, let us consider the flagellar motion of a spermatozoon with beat frequency $\nu \sim 30$ Hz, wavelength $\lambda \sim 70$ μm [30], and flagella diameter $d \sim 100$ nm [8]. For a waving flagella the maximum velocity reached by any rod section is the wavespeed $V = \nu\lambda$, and $\ell = 0.09\lambda$. Using $u_{\dot{\gamma}} \approx V$ the constraint in Eq. (2.24) simplifies to the inequality $\Gamma\nu \leq 0.09$, and for the given swimmer the range of critical times our model can describe is given by $\Gamma \leq 3 \times 10^{-3}$ s. Alternatively, if the fluid properties are given the model is constrained by a maximum actuation frequency.

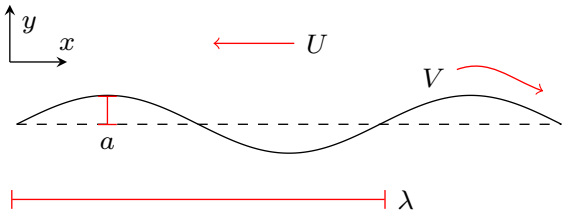

Fig. 2.5 Sinusoidal travelling waveform as a model for the locomotion of flagellated eukaryotic cell. Swimming, with speed U, is in the opposite direction to the travelling wave, with wavespeed V. See text for notation.

2.3 Locomotion of waving slender filaments

In order to illustrate the results given by our non-Newtonian resistive-force theory we apply in this section this modelling approach to study the waving of slender filament as a model for the locomotion of flagellated eukaryotes [22].

2.3.1 Setup

We consider the swimming of an infinite inextensible filament whose shape deforms as a planar sinusoidal waveform given in Cartesian coordinates by

$$y(x,t) = a\sin(2\pi x/\lambda - \omega t), \tag{2.25}$$

where a is the wave amplitude, ω the wave frequency and λ its wavelength. The x axis is the direction of propagation of the wave (see notation in Fig. 2.5). As a result of the waving motion, the filament undergoes locomotion in the $-x$ direction. Since the filament is infinite, the swimming speed is expected to be steady. We non-dimensionalise length scales by $\lambda/(2\pi)$ and times by ω^{-1}, hence the waveform equation simplifies to $y = \epsilon\sin(x-t)$, where $\epsilon = 2\pi a/\lambda$, such that the non-dimensionalised wavespeed $V = \lambda\omega/(2\pi) = 1$. The Newtonian drag coefficients are non-dimensionalised by the zero-shear viscosity.

For a slender flagellum the force per unit length exerted by the fluid on the flagellum, $\mathbf{f}$, is quantified by the non-Newtonian resistive-force theory as

$$\mathbf{f}_{E/C} = -\left[R_{E/C}c_{\parallel}\hat{\mathbf{t}}\hat{\mathbf{t}} + R_{E/C}c_{\perp}(\mathbf{I}-\hat{\mathbf{t}}\hat{\mathbf{t}})\right]\cdot\mathbf{u}, \tag{2.26}$$

where $\hat{\mathbf{t}}$ is the local tangent to the filament, $\mathbf{u}$ is the lab-frame velocity, and R_E (resp R_C) is the non-Newtonian correction factor for the Newtonian drag coefficients $(c_{\parallel}, c_{\perp})$ based on the experiments (resp. on the Carreau model). Classically, the non-dimensionalised

velocity of each point along the flagellum can be written in the laboratory frame as [22]

$$\mathbf{u} = (1 - U)\hat{\mathbf{x}} - q\hat{\mathbf{t}}(s), \tag{2.27}$$

where $q = \Lambda/\lambda > 1$ is the ratio between the wavelength Λ measured along the flagellum arc-length (s) and the wavelength λ measured along the x direction, $\hat{\mathbf{x}}$ is the unit vector along the direction of the traveling wave, and $U < 1$ the non-dimensionalised (unknown) swimming speed. In order to determine the value of U we enforce the free-swimming condition namely

$$\int_0^\Lambda \mathbf{f} \cdot \hat{\mathbf{x}} ds = 0, \tag{2.28}$$

with the other components being zero by symmetry. The force density along x, f_x, is given by

$$f_x = \mathbf{f} \cdot \hat{\mathbf{x}} = -R_{E/C} c_\perp \mathbf{u} \cdot \hat{\mathbf{x}} + (R_{E/C} c_\perp - R_{E/C} c_\parallel)(\mathbf{u} \cdot \hat{\mathbf{t}})(\hat{\mathbf{t}} \cdot \hat{\mathbf{x}}). \tag{2.29}$$

Using Eq. (2.27), the above simplifies to

$$f_x = R_{E/C} c_\perp (U - 1) + R_{E/C} c_\parallel q\hat{\mathbf{t}} \cdot \hat{\mathbf{x}} + (R_{E/C} c_\perp - R_{E/C} c_\parallel)(1 - U)(\hat{\mathbf{t}} \cdot \hat{\mathbf{x}})^2. \tag{2.30}$$

Furthermore we define a dimensionless critical time to complete our non-dimensionalisation, where Γ is rescaled to $\Gamma\omega$ (with identical notation retained for convenience) such that the Carreau correction factor becomes

$$R_C = \left[1 + \left(\frac{\Gamma c_\perp u_{\dot{\gamma}}}{2\sqrt{2}\pi b}\right)^2\right]^{\frac{n-1}{2}}, \tag{2.31}$$

where

$$u_{\dot{\gamma}}^2 = (1 - U)^2(\hat{\mathbf{x}} \cdot \hat{\mathbf{n}})^2 + 2\frac{c_\parallel^2}{c_\perp^2}\left((1 - U)\hat{\mathbf{x}} \cdot \hat{\mathbf{t}} - q\right)^2. \tag{2.32}$$

Similarly upon non-dimensionalisation the experimental correction factor becomes,

$$R_E = \left[1 + 0.317\left(\frac{(1 - n)\Gamma|\mathbf{u}|}{d_s}\right)^{0.692}\right]^{-1}, \tag{2.33}$$

where

$$|\mathbf{u}|^2 = [(1 - U) - q\hat{\mathbf{t}} \cdot \hat{\mathbf{x}}]^2 - (q\hat{\mathbf{t}} \cdot \hat{\mathbf{y}})^2. \tag{2.34}$$

The unit tangent and normal to this wave are further given by $\hat{\mathbf{t}} = (\cos\theta, \sin\theta)$ and $\hat{\mathbf{n}} = (-\sin\theta, \cos\theta)$ where θ is the angle between the swimming direction ($\hat{\mathbf{x}}$) and the local tangent to the flagellum ($\hat{\mathbf{t}}$). We now have four dimensionless constants we are able to vary: n and Γ describing the fluid; α describing the aspect ratio of the flagellum; and ϵ describing the amplitude of the waveform. The variables n and Γ enter only through the correction factor whereas α and ϵ enter into both the correction factor and the Newtonian calculation through the Newtonian drag coefficients $c_\perp$ and $c_\parallel$ which depend logarithmically on α, and ϵ through the integral over the arc-length s.

Note that, as discussed above, the resistive-force theory description is only valid when the viscosity changes are local, hence in non-dimensional values the range of viable critical times is $\Gamma \lesssim 0.6$, whose value is given for a typical spermatozoa flagella described in Section 2.2.7.

2.3.2 Numerical implementation and validation

In order to validate our numerical implementation, we first address Newtonian swimming. We compare our numerical implementation of Eq. 2.28 in the Newtonian limit to the analytic Newtonian result, namely [22]

$$U_N = \frac{\left(1 - c_\parallel/c_\perp\right)(1-\beta)}{1 - (c_\parallel/c_\perp - 1)\beta}, \tag{2.35}$$

where

$$\beta = \frac{1}{\Lambda}\int_0^\Lambda \hat{\mathbf{t}}\cdot\hat{\mathbf{x}}ds = \frac{1}{\Lambda}\int_0^\Lambda \cos^2\theta ds. \tag{2.36}$$

At small amplitude $\epsilon \ll 1$, the swimming speed limits to the asymptotic result

$$U_N = \frac{\epsilon^2(1 - c_\parallel/c_\perp)}{2c_\parallel/c_\perp}, \tag{2.37}$$

which agree with our numerics when ϵ decreases as shown in Fig. 2.6a. A closer agreement can be found for all values of ϵ by comparing our full numerical results to the swimming speed given in Eq. (2.35), where β is evaluated numerically. The comparison is show in Fig. 2.6b and therefore validates our numerical implementation of the free-swimming problem.

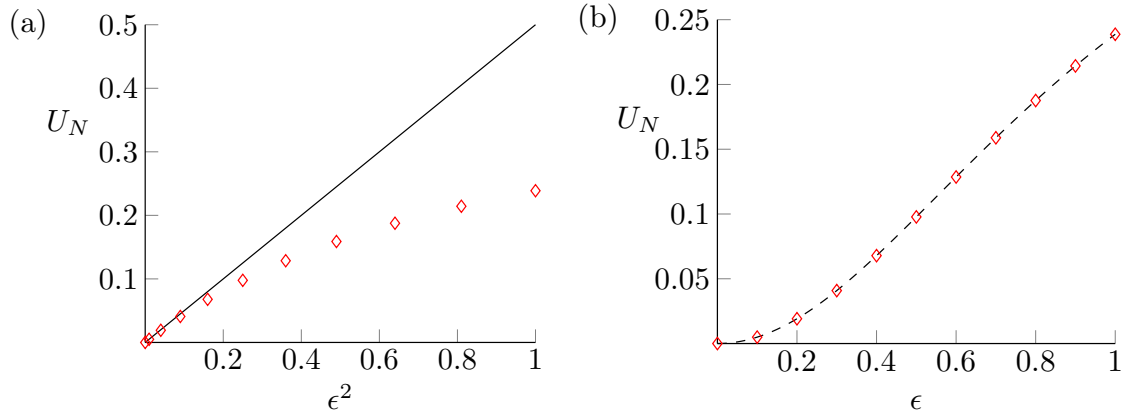

Fig. 2.6 The numerical Newtonian results are compared to the analytic Newtonian results, (a) small-amplitude analytical expansion of Eq. 2.37 (solid line, $\epsilon \ll 1$) compared to numerical results (red diamonds) and (b) Analytical result of Eq. (2.35) with β evaluated numerically (dashed line) compared to numerical results (red diamonds).

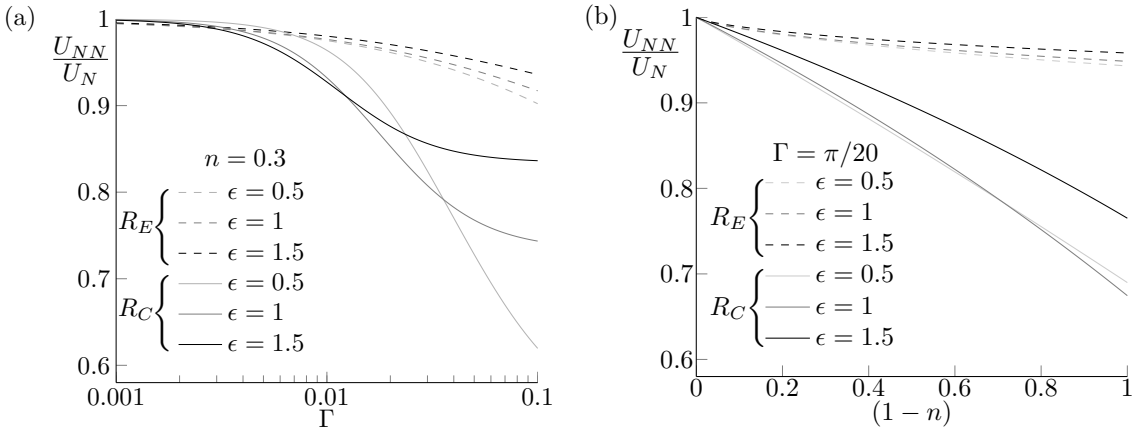

Fig. 2.7 Ratio between the non-Newtonian and Newtonian swimming speeds, U_{NN}/U_N, as a function of the properties of the fluid. (a) speed ratio with fixed $n = 0.3$ for a range of amplitudes ϵ plotted against the critical fluid time Γ. (b) speed ratio with fixed value of $\Gamma = \pi/20$ for a range of wave amplitudes ϵ plotted against the power index of the fluid, n. The swimming speed is always reduced in a shear-thinning fluid.

2.3.3 Non-Newtonian locomotion

We now follow a similar numerical approach to tackle the non-Newtonian problem, however as the integral depends on the velocity U, we must solve this iteratively, taking the Newtonian solution as the initial value from which we iterate. The main results are shown in Fig. 2.7 where we plot the ratio between the non-Newtonian swimming speed of the waving flagellum (U_{NN}) and the Newtonian one (U_N) as a function of the critical time of the fluid Γ (a) and as a function of the power index n (b). Results for the two models are superimposed: the Carreau approach is plotted in solid lines while the experimentally-based model is show in dashed line, each for a few different values of the wave amplitude ϵ.

While the Carreau and experimental models do not agree quantitatively, they both provide a similar physical picture. Under this modelling approach, swimming of a waving flagellum is always slower in a non-Newtonian fluid than in a Newtonian fluid, and all the more that the critical time Γ increases Fig. 2.7a or that the power index n decreases Fig. 2.7b. Both illustrate that, for a fixed geometry, the greater the non-Newtonian effects in the fluid the slower the resulting swimming speed.

We further see in Fig. 2.7 that the results for different wave amplitudes, ϵ, do not collapse onto the same curve; non-Newtonian swimming has therefore a different ϵ dependence from Newtonian swimming. To address this we plot the ratio of the swimming speeds against ϵ for a fixed Γ value and a range of power indices in Fig. 2.8. For both models, we observe a non-monotonic dependence of the swimming speed ratio on the wave amplitude ϵ. The swimming speed always deceases with ϵ for small amplitudes, reaches a minimum for the Carreau correction factor and experimental correction factor when $\epsilon \approx 1.2$ and $\epsilon \approx 0.6$ respectively (the precise value depends in fact on the fluid properties). Finally, at large amplitudes, the swimming speed ratio asymptotes again to $U_{NN}/U_N \approx 1$.

Unlike the Newtonian result, both non-Newtonian swimming speeds depend on the rod shape *i.e.* the value of α, as the correction factors depend on α in such a way that it cannot be factored out of the integral equation. As with Γ, both the experimental and Carreau model swimming speeds decrease monotonically with increasing α, showing that we would expect fatter swimmers to be hindered more by the shear-thinning fluid. These results are not shown here as they are qualitatively similar to the dependence on Γ in Fig. 2.7a.

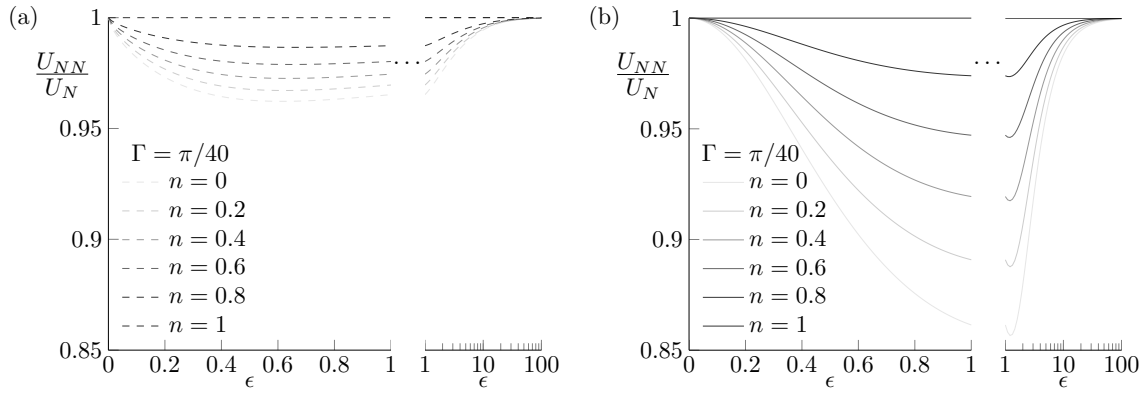

Fig. 2.8 Ratio of the non-Newtonian to Newtonian swimming speeds U_{NN}/U_N for fixed critical time $\Gamma = \pi/40$, for a range of power indices n as a function of the flagellum amplitude ϵ, (a) experimental model (R_E) and (b) Carreau model (R_C).

2.3.4 Asymptotic results

In order to understand further the systematic decrease in swimming speed compared to the Newtonian results we turn to considering the impact of a small amount of non-Newtonian rheology to the fluid. The transition between a Newtonian fluid and a shear-thinning fluid occurs for fluids with a finite critical time and with a shear-thinning index below unity. In the experimental correction factor, both terms $(1-n)$ and Γ appear as a single factor $\chi_E \equiv [(1-n)\Gamma]^{0.692}$. In the Carreau model we must assume that $(1-n)$ is small to ensure that the non-Newtonian effects are small. Since $(1-n)$ only appears as a power in the correction factor R_C, the lowest order non-zero term is $\chi_C \equiv (1-n)\Gamma^2$.

We can then expand mathematically both empirical models about the small parameters χ_E and χ_C respectively, leading to swimming with speeds written at first order as $U_{NN}^{(E)} \approx U_0 + \chi_E U_1^{(E)}$ and $U_{NN}^{(C)} \approx U_0 + \chi_C U_1^{(C)}$ respectively. At zeroth order for both models the Newtonian result is recovered such that $U_0 = U_N$. In order to expand the velocity-dependent drag correction factors we must insert $U_{NN}^{(E)}$ and $U_{NN}^{(C)}$ into their respective correction factors R_E and R_C, such that $R_E \approx 1 + \chi_E R_{E(1)}$ and $R_C \approx 1 + \chi_C R_{C(1)}$ where

$$R_{E(1)} = -0.317 \left(\frac{|\mathbf{u}_0|}{d_s} \right)^{0.692}, \tag{2.38}$$

and

$$R_{C(1)} = -\frac{1}{2} \left(\frac{c_\perp u_{\dot{\gamma}_0}}{2\sqrt{2}\pi b} \right)^2, \tag{2.39}$$

are the first order correction factors, in which

$$|\mathbf{u}_0| = \sqrt{(1+q^2) + U_0^2 + 2q(U_0-1)\cos\theta - 2U_0}, \tag{2.40}$$

and

$$u_{\dot{\gamma}_0} = \sqrt{(1-U_0)^2(\hat{\mathbf{x}}\cdot\hat{\mathbf{n}})^2 + 2\frac{c_\parallel^2}{c_\perp^2}\left((1-U_0)\hat{\mathbf{x}}\cdot\hat{\mathbf{t}} - q\right)^2}, \tag{2.41}$$

are the leading order rod section velocity and shear rate velocity respectively. After expansion, the first-order experimental and Carreau swimming speeds are obtained to be

$$U_1^{(E)} = -0.317\left(\frac{1}{d_s}\right)^{0.692}\frac{\int_0^\Lambda |\mathbf{u}_0|^{0.692}P(\theta)ds}{c_\perp\Lambda - \beta(c_\perp - c_\parallel)\Lambda}, \tag{2.42}$$

and

$$U_1^{(C)} = -\frac{1}{2}\left(\frac{c_\perp}{2\sqrt{2}\pi b}\right)^2\frac{\int_0^\Lambda u_{\dot{\gamma}_0}^2 P(\theta)ds}{c_\perp\Lambda - \beta(c_\perp - c_\parallel)\Lambda}, \tag{2.43}$$

respectively, where

$$P(\theta) = (1-U_0)c_\perp - c_\parallel\cos\theta - (1-U_0)(c_\perp - c_\parallel)\cos^2\theta, \tag{2.44}$$

where θ is implicitly a function of the arc-length s. The right-hand side of both Eqs. (2.42) and (2.43) only depend on the Newtonian results and can thus be easily evaluated numerically. The results for both $U_1^{(E)}$ and $U_1^{(C)}$ are shown in Fig. 2.9. Both the experimental and Carreau first-order swimming speeds are negative for all values of the wave amplitude indicating a decrease in the swimming speed with non-Newtonian effects in agreement with our full numerics.

2.3.5 Physical interpretation

In order to gain some fundamental understanding on the origin of the observed systematic reduction in swimming speed, we take a closer look at the distribution of shear-rates along the waving flagellum. As the non-Newtonian equations are too nonlinear to glean physical insight, we consider the Newtonian shear-rates to inform our understanding of the system. We use the shear-rates calculated for our Carreau correction factor with the knowledge that larger shear-rates will lead to reduced drag force for both our correction factors.

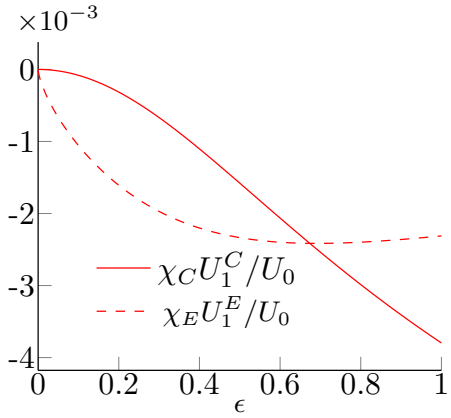

Fig. 2.9 First-order corrections to the Newtonian velocity scaled by the Newtonian speed, U_1/U_0, for the Carreau model (solid line) and the experimental model (dashed line) as a function of the wave amplitude ϵ. The correction is always negative indicating a decrease in the swimming speed.

We consider separately the "thrust" problem, where $U = 0$ and a net force is a applied on the fluid, and the "drag" problem, where $V = 0$ and the flagellum is dragged passively through the fluid. In the thrust problem, denoted '*th*', the magnitude of non-dimensionalised shear-rate velocity is given by

$$u_{\dot{\gamma}_{th}} = \sqrt{\sin^2\theta + 2\frac{c_{\parallel}}{c_{\perp}}(\cos\theta - q)^2}, \tag{2.45}$$

leading to a shear-rate along the flagellum of

$$|\dot{\boldsymbol{\gamma}}_{th}| = \frac{c_{\perp} u_{\dot{\gamma}_{th}}}{2\sqrt{2}\pi b}, \tag{2.46}$$

where shear-rates are non-dimensionalised by ω. In the drag problem, denoted by '*dr*', since the non-dimensionalised relevant shear-rate velocity is given by

$$u_{\dot{\gamma}_{dr}} = U\sqrt{\sin^2\theta + 2\frac{c_{\parallel}}{c_{\perp}}\cos^2\theta}, \tag{2.47}$$

the shear-rate is then given by

$$|\dot{\boldsymbol{\gamma}}_{dr}| = \frac{c_{\perp} u_{\dot{\gamma}_{dr}}}{2\sqrt{2}\pi b}. \tag{2.48}$$

The distribution of shear-rates for both thrust and drag problems is shown in Fig. 2.10 for two wave amplitudes (small in thin line and large in thick line). Note that

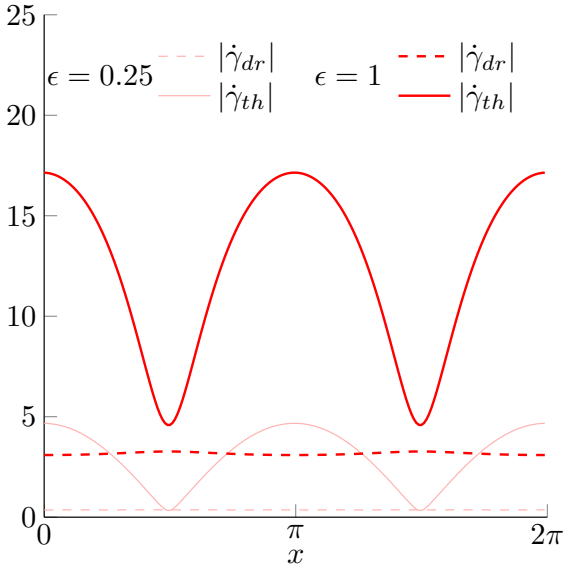

Fig. 2.10 Dimensionless shear-rates along a waving flagellum as a function of the dimensionless position x along the flagellum for the drag problem (dashed lines) and the thrust problem (solid lines), shown for a small amplitude ($\epsilon = 0.25$) and large amplitude ($\epsilon = 1$) swimmer.

the drag problem is computed for $U = U_N$ i.e. we are comparing the shear-rates for the flow around the flagellum for the two problems which, on average, induce equal and opposite forces during the swimming motion. What is apparent from these results is that the shear-rates in the thrust problem are systematically larger than in the drag problem essentially everywhere along the waving flagellum. In a shear-thinning fluid, the higher the shear-rate the lower the viscosity. Since for swimming thrust and drag have to balance, we see that if the swimming speed was kept constant, forces would not balance and there would be more drag than thrust. The value of the swimming speed has thus to decrease in order to compensate for it.

An alternative way to interpret this result is to consider the case of waving at small amplitude ϵ. In that limit, the shear-rates for the thrust and drag problems are given by

$$|\dot{\gamma}_{th}| \approx \frac{c_\perp \epsilon |\cos(x-t)|}{2\sqrt{2}\pi} + O(\epsilon^2), \tag{2.49}$$

and,

$$|\dot{\gamma}_{dr}| \approx \frac{c_\parallel \epsilon^2}{2\sqrt{2}\pi} \frac{\left(1 - c_\parallel/c_\perp\right)}{c_\parallel/c_\perp} + O(\epsilon^4), \tag{2.50}$$

respectively. As the shear-rate in the drag problem is a factor ϵ smaller than the one due to thrust generation, we obtain a relatively larger reduction in thrust, and

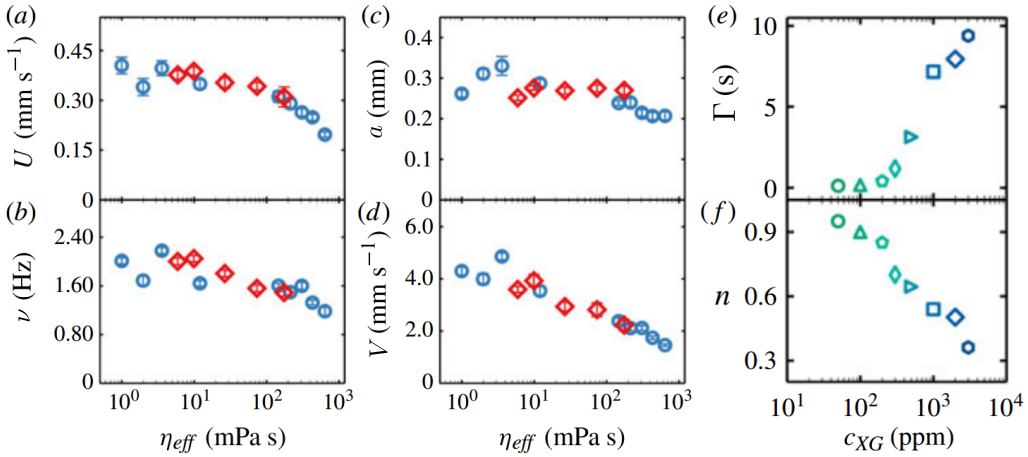

Fig. 2.11 Summary of nematode kinematics for Newtonian (blue) and shear-thinning (red) fluids with each data point representing the mean and standard error of approximately 15 recordings, and a summary of the shear-thinning fluid fitting parameters. (a) Swimming speed U, (b) beat frequency ν, (c) head amplitude a, (d) wave speed V, all as a function of the effective viscosity η_{eff}. Carreau fluid parameters are fitted to cone-plate rheometry data for each fluid. (e) Carreau time scale Γ and (f) the shear-thinning index n. Adapted and Reprinted from Ref. [143].

thus a reduction in the swimming speed. Fundamentally, the difference in shear-rate scaling between thrust ($\sim \epsilon$) and drag ($\sim \epsilon^2$) arises from the fact that in the thrust-producing waving motion, only a small subset of the periodic up-and-down motion in the direction perpendicular to the swimming direction is rectified to produce useful work for swimming.

2.4 Comparison with *C. elegans* experiments

In order to demonstrate the relevance of our empirical model we now compare our simulations results to the experimental results of Gagnon et al. [143], where the swimming motion of the small nematode *Caenorhabditis elegans* (*C. elegans*) was studied in both Newtonian and shear-thinning fluids. The shear-thinning fluids in their study are composed of Xanthan gum solutions, shown by rheological measurements to be inelastic and well described by the Carreau model, with greater shear-thinning obtained for larger Xanthan gum concentrations. *C. elegans* are then immersed in the different fluids within an acrylic chamber of diameter 2 cm and thickness 1 mm. The organisms are approximately 1 mm in length and 80 μm in diameter. Through body tracking, the swimming speed, frequency, wavespeed and amplitude of the waving

nematode is measured in each of the different fluids as shown in Fig. 2.11 together with the Carreau fluid parameters for each of the shear-thinning fluids. These are then plotted against an effective viscosity η_{eff}, defined as the average viscosity over the shear-rates experienced by the swimmer, $U/L \leq \dot{\boldsymbol{\gamma}} \leq 2\omega B/d$, and ranging in this series of experiments from 6 mPa s to 200 mPa s. The results for shear-thinning fluids are then compared to Newtonian fluids with similar viscosities to the effective viscosities of the shear-thinning fluids.

Using the experimental data from Ref. [143], the waveform and wavespeed of each swimmer in the different fluids is known as well as the fluid properties, and thus a direct comparison with our model results can be made with no fitting parameters. The only parameter which can be altered in our simulations is the length of the unphysical rod 'sections' which affects both the Newtonian and non-Newtonian results through the Newtonian drag coefficients. Here we choose two examples one identical to the the previous planar wave analysis where $\ell = 0.09\lambda$ and a second with more realistic ellipsoidal rods with $\ell = \ell_{nema}$ as $\ell_{nema} < \lambda$. This comparison is presented in Fig. 2.12 where we plot the dimensional swimming speed, U, against the effective viscosity, η_{eff}. Each simulation data point shares fluid and swimmer properties with the experimental shear-thinning swimming speed at that particular effective viscosity. Experimental results are shown with open symbols (each data point represents the mean and standard error of approximately 15 experiments [143]) while the results of our models are shown with line symbols (rod-like filaments) and filled symbols (ellipsoidal filaments). Specifically we use line symbols (crosses and stars) to plot results of our modelling approach using $\ell = 0.09\lambda$, as described in Section 2.2.2 (both the experimental and the Carreau model), here the Newtonian drag ratio is given by $c_\perp/c_\parallel \approx 1.1$. As the wavelength is larger than the length of the nematode, ℓ is too short. Instead we choose the body length ℓ_{nema} and note that its shape is more accurately described by that of a prolate ellipsoid of aspect ratio $\alpha = d_{nema}/l_{nema} \approx 0.08$, where d_{nema} is the nematode diameter. Using the drag coefficients described in Ref. [149] for prolate spheroids, we find that the dimensions of *C. elegans* correspond to a drag ratio $c_\perp/c_\parallel \approx 1.5$, which is within the range of drag ratios calculated by Ref. [31] for biologically relevant swimming. The corresponding results are show with filled circles in Fig. 2.12 for the experimental empirical model and the Carreau empirical model.

While some discrepancies exist, we see that both sets of numerical simulations share the qualitative features of the experimental results, which are greater than all modelling in both Newtonian and non-Newtonian fluids. Our empirical non-Newtonian resistive-force theory is thus able to capture the main physical features of swimming

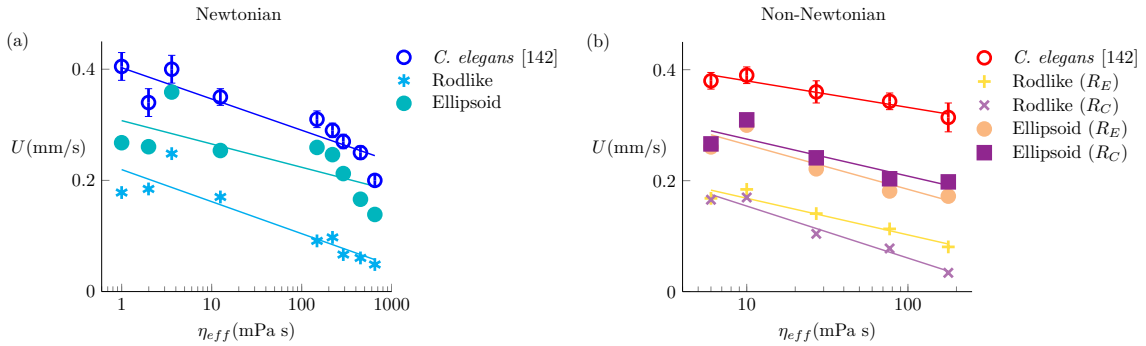

Fig. 2.12 Experimental results from Ref. [143] (open symbols with error bars) plotted together with our simulation results (line or filled symbols). Newtonian swimming speeds are shown in (a), and non-Newtonian swimming speeds in (b). The simulation results are represented by line symbols for thin rod results and filled symbols for fat rod results. The lines in each of the different colours are straight lines of best fit to their matching colour symbol. Each shear-thinning simulation data point shares fluid and swimmer properties with the red experimental shear-thinning swimming speed at that particular effective viscosity.

in a shear-thinning fluid. Quantitative differences are expected to arise from multiple sources. First, our model is confined to local effects of the thinning fluid whereas we estimate the fluid to be thinned over 100 nematode radii in the experiments. This would lead to soft confinement effects, and an increase of the swimming above that shown by the thick filament model in Fig. 2.12b [106, 147]. Furthermore our simulations do not include end effects, which are predicted to increase swimming speeds in non-Newtonian fluids [150, 125]. Wall effects in the confined experimental setup are also expected to play a role whereas our model considers swimming in an infinite fluid. Despite these possible sources of discrepancies, our simple empirical model is able to capture the main physical features of waving locomotion in a shear-thinning fluid.

2.5 Discussion

Flagella waving in fluids are expected to be subject to two types of physical changes when the fluid is no longer Newtonian but is shear-thinning [146]. The first one, local, is due to the decrease of the fluid forces resulting from a decrease of the fluid viscosity. The second, nonlocal, results from overall changes to the flow field in the fluid, and is similar to enhanced in swimming under soft confinement [106, 147]. In this Chapter we proposed an empirical model to quantify the first of these effects by replacing the classical Newtonian drag coefficients with velocity-dependent shear-thinning drag

coefficients based on experimental results or empirical modelling. We illustrated our new models by calculating the swimming speed of an infinite planar wave swimmer with a slender flagellum, for a range of shear-thinning fluid parameters, and apply our results to a set of experimental results on *C. elegans* taking into account the ellipsoidal shape of the nematode [143].

The main limitation to our model, beyond the fact that it is clearly not derived from first principles and is thus empirical, is the small range of relaxation times (or actuation frequencies) where our model is viable. Indeed, as with Newtonian resistive-force theory, we must ensure that the flow induced by the moving portion of a filament is local otherwise interactions between different sections of the filament are required. In a shear-thinning fluid this means that the flow outside the "region of influence" of size ℓ needs to be Newtonian to allow fluid stresses to be determined solely by the local kinematics. This imposes thus a limit on the range of shear-rates between the critical shear-rate and the largest shear-rate experienced by the flagella. Typical shear-rates generated by spermatozoa, cilia and *C. elegans* are in the range $10^1 - 10^3\,\mathrm{s}^{-1}$, and typical critical shear-rates of mucus are on the order $|\dot{\boldsymbol{\gamma}}_C| \sim 10^{-3}\,\mathrm{s}^{-1}$ [84], and soil $|\dot{\boldsymbol{\gamma}}_C| \sim 10^{-1}\,\mathrm{s}^{-1}$ [85]. Hence the typical distance r away from a particular location along the flagellum where the fluid is Newtonian is on the order $r/a \sim 10^2$ for *C. elegans* in soil and $r/a \sim 10^4 - 10^5$ for cilia and spermatozoa in mucus. Meaning the fluid around biological organisms is already heavily sheared by the motion at a length ℓ before the swimmer, and therefore the requirement $\Gamma\nu \leq 0.09$ is likely to not be reached in vivo.

Further improvements to these models would ideally capture the shear-thinning fluid effects of the rod sections around each rod section of the flagellum, *i.e.* the creation of a non-Newtonian slender body theory, however this would require an accurate calculation of the shear-rates experienced by the rod section. Something we cannot capture with our locally Newtonian assumption and would require the use of non-Newtonain stokeslets and doublets. Additional improvements could be made by combining the shear-thinning effect discussed in this Chapter with the effect of a polymer-depleted region around the rod [106].

While the work presented here focused on planar waving motion it can be adapted to helical propulsion of bacteria. In that case, and unlike for planar swimming, the presence of a head is crucial to balance hydrodynamic moments [151]. The force integral over the rigid helical flagella must match the force generated by the head, and similarly for the torque, then the rotation rate and the swimming speed can be obtained. In order to describe the force and torque on the head both the rotational and translational the drag coefficient of the head would be required. If the head is rod-shaped then

the translational drag coefficients are as described in this paper, however for spherical (e.g. *coccus*) or more complex head shapes knowledge of new drag coefficients would be required, obtained experimentally or numerically.

Beyond simple flagellar-based locomotion, resistive-force theory has also been used to tackle large variety of problems in the biophysics of swimming cells. With our modelling approach, these results could then be extended to more complex fluids. Problems which could be tackled include the polymorphic transitions of bacteria flagella [152], bundling of flagella [153], swimming non-flagellated bacteria [154], the generation of waving modes in passive [155, 29] and active filaments [46], and the motion of filaments in external flows [156, 157].

3

Small-amplitude rigid swimmers in viscoelastic fluids

3.1 Introduction

We consider mathematically the most general problem for planar locomotion using small-amplitude waves periodic both in space and in time. Specifically, we prescribe the shape deformation as a sum of waves travelling with different wavenumbers and frequencies and in different directions and consider the resulting locomotion in a viscoelastic, Oldroyd-B fluid. This swimmer is rigid such that the waveform is unaffected by the surrounding fluid. We show that swimming in a non-Newtonian fluid at small amplitudes need not always lead to slower swimming compared to the Newtonian case, provided the right combination of waves are considered. For swimming enhancement to be observed, different waves need to travel in opposite directions, and the enhancement in that case results from the asymmetric viscoelastic damping of waves with different frequencies. A change of the swimming direction is also possible. After presenting the general derivations, and introducing a sufficient condition for enhanced locomotion, we analyse in detail the cases of two or three travelling waves. The enhancement in a viscoelastic fluid can be obtained for all Deborah numbers below a critical value or, in the case of three waves or more, only if a finite amount of elasticity is present in the fluid.

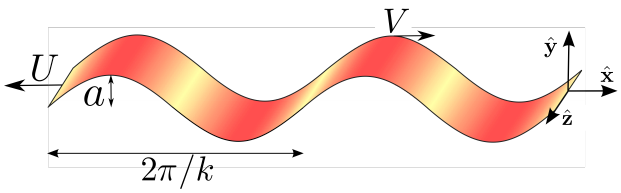

Fig. 3.1 A two-dimensional flexible sheet deforming as a traveling wave with amplitude a, wave number k, wave speed V, and frequency $\omega = kV$ resulting in its swimming at speed U.

3.2 General small-amplitude wave in a viscoelastic fluid

3.2.1 Setup

Analogous to Taylor's classic swimming calculation [9, 44], an infinite inextensible two-dimensional sheet of negligible thickness is placed in a fluid and undergoes waving motion, as illustrated in Fig. 3.1.

The waveform of the sheet is prescribed, and results in swimming. In the frame of the swimmer the oscillation of the vertical position, $y(x,t)$, of the sheet is described by,

$$y(x,t) = a \sum_{n=-\infty}^{+\infty} \sum_{m=-\infty}^{+\infty} \alpha_{n,m} e^{i(mkx - n\omega t)}, \tag{3.1}$$

where x denotes the coordinate along the average sheet axis and t time. In Eq. (3.1), a is the sheet amplitude, k the fundamental wavenumber and ω the fundamental frequency. Furthermore the modes $n = 0$ and $m = 0$ are omitted as there is no mean deformation in x or in time. The fluid is assumed to be located above the sheet along the $y > 0$ direction, we only need to consider fluid above (or below) the sheet as we only consider the flow at infinity which is the same above or below the sheet. We allow both positive and negative values of the mode number (m, n) in order to include waves travelling in both directions along the sheet. The order-one complex coefficients $\alpha_{n,m}$ represent dimensionless Fourier amplitude of each (m, n) mode and since y is real they satisfy $\alpha_{-n,-m} = \alpha^*_{n,m}$. To simplify notation all sums over n and m from $-\infty$ to $+\infty$ will be denoted with a single summation symbol, $\sum_{n,m}$.

Upon non-dimensionalising x by k^{-1} and t by ω^{-1}, Eq. (3.1) becomes

$$y(x,t) = \epsilon \sum_{n,m} \alpha_{n,m} e^{i(mx-nt)}, \tag{3.2}$$

with a prefactor $\epsilon = ak$ defined as the ratio of the sheet amplitude to its wavelength. We assume that this ratio is small in this Chapter, $\epsilon \ll 1$, allowing the swimming speed to be computed as an asymptotic expansion in ϵ.

As the sheet is infinite along the z direction we can reduce the three-dimensional swimming problem to two dimensions. The velocity field is written as $\mathbf{u} = u_x\hat{\mathbf{x}} + u_y\hat{\mathbf{y}}$. This allows a streamfunction, $\psi(x,y,t)$, to be defined such that $u_x = \partial\psi/\partial y$ and $u_y = -\partial\psi/\partial x$, ensuring that the flow remains incompressible, $\nabla \cdot \mathbf{u} = 0$.

In order to find the streamfunction we must first consider the boundary conditions imposed on the flow. On the waving sheet the no slip boundary condition enforces the velocity of the fluid at the sheet location to be the same as the velocity of the sheet, so that

$$\nabla\psi|_{x,y(x,t)} = \epsilon \sum_{n,m} in\alpha_{n,m} e^{i(mx-nt)}\hat{\mathbf{x}}. \tag{3.3}$$

Far away from the sheet we expect that the flow will be unaffected by the wavemotion. Hence in the frame of the swimmer, the far field velocity will be the speed of the swimmer, but in the opposite direction. So if the steady swimming of the sheet is denoted $-U\hat{\mathbf{x}}$ then we have the boundary condition

$$\nabla\psi|_{x,\infty} = U\hat{\mathbf{x}}, \tag{3.4}$$

where the value of U is to be determined.

3.2.2 Constitutive relationship: Oldroyd-B fluid

At low Reynolds number, which is the relevant limit for microorganisms, the flow around the sheet is described by the Cauchy equation,

$$\nabla p = \nabla \cdot \boldsymbol{\tau}, \tag{3.5}$$

with p the pressure, and $\boldsymbol{\tau}$ the deviatoric stress. Viscoelastic effects in the fluid are modelled using the classical Oldroyd-B evolution equation for $\boldsymbol{\tau}$. The Oldroyd-B constitutive equation models a dilute solution of infinitely extensible polymers in a Newtonian solute as a homogeneous continuum [158, 87]. In this classical model, the shear viscosity is constant but the polymer elasticity affects the flow, giving rise

to normal stresses. The Oldroyd-B model is the simplest of the dumbbell models that can be rigorously derived from a dilute solution of infinitely-extensible elastic dumbbells in a Newtonian solvent [87]. The Oldroyd-B model captures many features of Boger (elastic, constant viscosity) fluids such as those used in experiments on propulsion [111, 110, 159, 112]. Furthermore, from Ref. [44], we expect that to second order in ϵ, our asymptotic results will remain valid for a large class of constitutive relationships. In an Oldroyd-B fluid, the total deviatoric stress, $\boldsymbol{\tau}$, a combination of stresses from the Newtonian solvent $\boldsymbol{\tau}_s$, and those from the polymers $\boldsymbol{\tau}_p$, is written as $\boldsymbol{\tau} = \boldsymbol{\tau}_s + \boldsymbol{\tau}_p$. If η_s denotes the solvent viscosity and assuming that $\boldsymbol{\tau}_p$ follows a first-order Maxwell constitutive equation with relaxation time λ, elastic modulus G, and polymer viscosity $\eta_p = G/\lambda$, the total stress obeys [87]

$$\boldsymbol{\tau} + \lambda \overset{\triangledown}{\boldsymbol{\tau}} = \eta\dot{\boldsymbol{\gamma}} + \eta_s\lambda \overset{\triangledown}{\dot{\boldsymbol{\gamma}}}, \tag{3.6}$$

where $\dot{\boldsymbol{\gamma}}$ is the shear rate tensor, defined as $\dot{\boldsymbol{\gamma}} = \nabla\mathbf{u} + \nabla\mathbf{u}^T$, and $\eta = \eta_s + \eta_p$ is the sum of the solvent and polymer viscosities. In Eq. (3.6),

$$\overset{\triangledown}{\mathbf{A}} = \frac{\partial \mathbf{A}}{\partial t} + \mathbf{u}\cdot\nabla\mathbf{A} - (\nabla\mathbf{u}^T\cdot\mathbf{A} + \mathbf{A}\cdot\nabla\mathbf{u}). \tag{3.7}$$

defines the upper-convected derivative that describes the rate of change of the tensor $\mathbf{A}$ while it translates and deforms with the fluid. Upon non-dimensionalising stresses by $\eta\omega$ and shear rates by ω, Eq. (3.6) becomes

$$\boldsymbol{\tau} + \mathrm{De}\overset{\triangledown}{\boldsymbol{\tau}} = \dot{\boldsymbol{\gamma}} + \beta\mathrm{De}\overset{\triangledown}{\dot{\boldsymbol{\gamma}}}, \tag{3.8}$$

where $\beta = \eta_s/\eta \leq 1$, and $\mathrm{De} = \lambda\omega$ is the Deborah number that describes the relative importance of viscoelasticity by comparing the relaxation time to the timescale on which the fluid is perturbed, given by ω^{-1}, where ω is the fundamental waving frequency.

3.2.3 Asymptotic solution

Since we have $\epsilon \ll 1$ we seek to find solutions to the streamfunction, stress and velocity in terms of perturbative expansion in ϵ, such that

$$\psi = \epsilon\psi_1 + \epsilon^2\psi_2 + \ldots, \tag{3.9}$$

$$\boldsymbol{\tau} = \epsilon\boldsymbol{\tau}_1 + \epsilon^2\boldsymbol{\tau}_2 + \ldots, \tag{3.10}$$

$$U = \epsilon^2 U_{2NN} + \ldots. \tag{3.11}$$

The swimming velocity is expected to be quadratic in ϵ, because of the symmetry $\epsilon \to -\epsilon$ due to the low Reynolds number regime in which the sheet propagates. A change from ϵ to $-\epsilon$ is identical to a shift in of half a period in time which cannot change the swimming speed as this is independent of time as the wave is infinite and the Stokes equations are time independent. The finite Deborah number introduces time dependence but from Ref. [44] we do not expect swimming at this order even at finite Deborah numbers. We thus focus on the first and second-order solutions (the subscript NN is used as a reminder that the final result for the swimming speed will quantify non-Newtonian swimming).

Solution at order ϵ

The leading-order constitutive equation is linear and given by

$$\boldsymbol{\tau}_1 + \mathrm{De}\frac{\partial \boldsymbol{\tau}_1}{\partial t} = \dot{\boldsymbol{\gamma}}_1 + \beta \mathrm{De}\frac{\partial \dot{\boldsymbol{\gamma}}_1}{\partial t}. \tag{3.12}$$

This can be reduced into a streamfunction equation by taking its divergence, combining with Eq. (3.5), and taking the curl to eliminate the pressure, leaving

$$\left(1 + \beta \mathrm{De}\frac{\partial}{\partial t}\right)\nabla^4 \psi_1 = 0. \tag{3.13}$$

The post-transient solution to Eq. (3.12) is found using Fourier notation and solving the biharmonic equation analytically, leading to

$$\psi_1 = \sum_{n,m} \alpha_{n,m}\frac{n}{m}(1 + |m|y)e^{-|m|y}e^{i(mx-nt)}, \tag{3.14}$$

where the first-order boundary conditions,

$$\nabla\psi_1|_{x,0} = \sum_{n,m} in\alpha_{n,m}e^{i(mx-nt)}\hat{\mathbf{x}}, \tag{3.15a}$$

and

$$\nabla\psi_1|_{x,\infty} = \mathbf{0}, \tag{3.15b}$$

are satisfied. Clearly, the first-order solution is the same as the Newtonian case, and as expected there is no swimming at this order.

Solution at order ϵ^2

At order ϵ^2, the constitutive equation, Eq. (3.8), is given by

$$\left(1+\mathrm{De}\frac{\partial}{\partial t}\right)\boldsymbol{\tau}_2-\left(1+\beta\mathrm{De}\frac{\partial}{\partial t}\right)\dot{\boldsymbol{\gamma}}_2= \\ \mathrm{De}(\nabla\mathbf{u}_1^T\cdot\boldsymbol{\tau}_1+\boldsymbol{\tau}_1\cdot\nabla\mathbf{u}_1-\mathbf{u}_1\cdot\nabla\boldsymbol{\tau}_1) \\ -\beta\mathrm{De}(\nabla\mathbf{u}_1^T\cdot\dot{\boldsymbol{\gamma}}_1+\dot{\boldsymbol{\gamma}}_1\cdot\nabla\mathbf{u}_1-\mathbf{u}\cdot\nabla\dot{\boldsymbol{\gamma}}_1). \tag{3.16}$$

Using Fourier notation of the form

$$\mathbf{A}=\sum_{n,m}\tilde{\mathbf{a}}^{(n,m)}e^{-int}, \tag{3.17}$$

for any tensor, vector, or scalar, the first-order constitutive equation, Eq. (3.12), gives access to the Fourier component of the first-order stress as

$$\tilde{\boldsymbol{\tau}}_1^{(n,m)}=\frac{1-in\beta\mathrm{De}}{1-in\mathrm{De}}\tilde{\dot{\boldsymbol{\gamma}}}_1^{(n,m)}. \tag{3.18}$$

As we are interested in the time-averaged swimming, it is sufficient to focus on the time-averaged version of Eq. (3.16). We then use Eq. (3.18) to express the mean of Eq. (3.16) using the Fourier modes of its right-hand-side, and obtain

$$\langle\boldsymbol{\tau}_2\rangle-\langle\dot{\boldsymbol{\gamma}}_2\rangle=\sum_{n,m}\frac{\mathrm{De}(1-\beta)}{1-in\mathrm{De}}\times \\ (\nabla\mathbf{u}_1^{T*}\cdot\dot{\boldsymbol{\gamma}}_1+\dot{\boldsymbol{\gamma}}_1\cdot\nabla\mathbf{u}_1^*-\mathbf{u}_1^*\cdot\nabla\dot{\boldsymbol{\gamma}}_1)^{(n,m)}. \tag{3.19}$$

With the first-order streamfunction whose Fourier component is

$$\tilde{\psi}_1^{(n,m)}=\alpha_{n,m}\frac{n}{m}(1+|m|y)e^{-|m|y}e^{imx}, \tag{3.20}$$

we obtain the Fourier modes of the flow velocity,

$$\tilde{\mathbf{u}}_1^{(n,m)}=\alpha_{n,m}\frac{n}{m}e^{-|m|y}e^{imx}\begin{pmatrix}-|m|^2y\\-(1+|m|y)im\end{pmatrix}, \tag{3.21}$$

the velocity gradient,

$$\nabla\tilde{\mathbf{u}}_1^{(n,m)} = \alpha_{n,m}\frac{n}{m}e^{-|m|y}e^{imx}\times \begin{pmatrix} -im|m|^2y & m^2(1+|m|y) \\ |m|^3y-|m|^2 & im|m|^2y \end{pmatrix}, \tag{3.22}$$

and the shear stress tensor,

$$\tilde{\dot{\boldsymbol{\gamma}}}_1^{(n,m)} = \alpha_{n,m}\frac{n}{m}e^{-|m|y}e^{imx}\begin{pmatrix} -2im|m|^2y & 2|m|^3y \\ 2|m|^3y & 2im|m|^2y \end{pmatrix}. \tag{3.23}$$

The divergence and curl are then taken, as before, to obtain an explicit equation for the second-order streamfunction as

$$\frac{d^4\langle\psi_2\rangle}{dy^4} = \sum_{n,m} -|\alpha_{n,m}|^2\frac{n^2}{m^2}\frac{(\beta-1)\mathrm{De}}{1-in\mathrm{De}}\times \frac{\mathrm{d}^2}{\mathrm{d}y^2}\Big[e^{-2|m|y}\left(-4im|m|^4y+4im|m|^5y^2-2|m|^3im\right)\Big]. \tag{3.24}$$

Integrating with respect to y three times, this gives

$$\frac{\mathrm{d}\langle\psi_2\rangle}{\mathrm{d}y} = Ay^2+By+C+ \sum_{n,m}|\alpha_{n,m}|^2\frac{n^2}{m^2}\frac{(\beta-1)\mathrm{De}}{1-in\mathrm{De}}e^{-2|m|y}(-2im|m|^4y^2+im|m|^2). \tag{3.25}$$

Given the form of the boundary conditions at infinity, Eq. (3.4), we obtain $A=B=0$ and C is equal to the second-order swimming speed, hence $C=U_{2NN}$. Its value can be found using the time-averaged second-order boundary condition,

$$\frac{\mathrm{d}\langle\psi_2\rangle}{\mathrm{d}y}\Big|_{x,0} = \sum_{n,m} nm|\alpha_{n,m}|^2, \tag{3.26}$$

leading to

$$U_{2NN} = \sum_{n,m} nm|\alpha_{n,m}|^2\left(\frac{1-in\mathrm{De}\beta}{1-in\mathrm{De}}\right). \tag{3.27}$$

Rewriting Eq. (3.27) with sums in n and m running from 1 to ∞ only, and using that $\alpha_{-n,-m} = \alpha^*_{n,m}$, leads to a simplified expression for the final result as

$$U_{2NN} = 2\sum_{n\geq 1}\sum_{m\geq 1} nm(|\alpha_{n,m}|^2 - |\alpha_{n,-m}|^2)\left(\frac{1+\beta n^2 \mathrm{De}^2}{1+n^2\mathrm{De}^2}\right), \tag{3.28}$$

where the opposite-sign contributions of waves travelling in the $+x$ and $-x$ direction are apparent.

3.3 A sufficient condition for enhanced swimming

The result in Eq. (3.28) gives the leading-order swimming speed of the swimming sheet with the most general shape deformation periodic in both x and t. When there are no viscoelastic effects $\mathrm{De} = 0$, and the Newtonian result is recovered. We denote the swimming speed U_{2N} in that case.

As can be seen in Eq. (3.28), it is the value of the (dimensionless) frequency n that affects the non-Newtonian change of each mode, not the value of the (dimensionless) wavenumber m. In order to gain insight into the conditions for swimming to be enhanced or slowed down by the presence of viscoelastic stresses, let us focus on the simple case where only the modes $|m| = |n|$ are present. The sheet deformation is written now as a linear superposition of travelling waves

$$y = \epsilon\sum_{n\geq 1} \alpha_{+n}e^{in(x-t)} + \alpha_{-n}e^{in(x+t)}, \tag{3.29}$$

where α_{+n} and α_{-n} describes the nth mode wave travelling to the right ($x > 0$) and left ($x < 0$) respectively. Using Eq. (3.28) this leads to non-Newtonian swimming with speed

$$U_{2NN} = \sum_{n\geq 1} u_n\left(\frac{1+n^2\beta\mathrm{De}^2}{1+n^2\mathrm{De}^2}\right), \tag{3.30}$$

and Newtonian swimming with speed,

$$U_{2N} = \sum_{n\geq 1} u_n, \tag{3.31}$$

where, we have further simplified notation such that

$$u_n = 2n^2(|\alpha_{+n}|^2 - |\alpha_{-n}|^2), \tag{3.32}$$

describes the superposition of mode n waves in both directions. Clearly, for both Newtonian and non-Newtonian cases, the addition of backwards waves always reduces the absolute value of the swimming speed. Let us now focus on the relative change in speed when comparing swimming between a Newtonian and a non-Newtonian fluid.

Using only inspection we cannot, a priori, define a range of Deborah number where we expect to see an increase in speed from the Newtonian to the non-Newtonian swimming (i.e. $U_{2NN}/U_{2N} > 1$). In order to look for further insight, we consider the infinite and zero Deborah number limits. At zero Deborah number, where there are no elastic effects, the ratio of swimming speeds is equal to 1. In the limit of large Deborah numbers $\mathrm{De} \gg 1$, where elastic effects dominate, it is straightforward to get from Eq. (3.30) that $U_{2NN}/U_{2N} = \beta < 1$, and thus swimming is always eventually decreased. As the value of De increases from zero to infinity, the speed ratio could monotonically decrease from 1 to β, in which case no enhancement would be seen, or non-monotonically, where enhancement could take place.

Our numerical simulations indicate that in the cases where the speed ratio does go above 1, then in most cases it is always increasing in the neighbourhood of $\mathrm{De} = 0$ before monotonically decreasing to β (see numerical results in Fig. 3.2 and discussion below). In order to characterise the behavior around $\mathrm{De} = 0$, we can compute derivatives and Taylor-expand the ratio of swimming speeds. The first derivative $\partial U_{2NN}/\partial \mathrm{De}$ evaluated at $\mathrm{De} = 0$ is zero because the swimming speed depends quadratically on the Deborah number. However, the second derivative (the curvature) is non-zero, and is given by

$$\left.\frac{\partial^2 U_{2NN}}{\partial \mathrm{De}^2}\right|_{\mathrm{De}=0} = \sum_{n\geq 1} 2n^2 u_n(\beta - 1). \tag{3.33}$$

When it is divided by the Newtonian swimming speed, Eq. (3.31), the above gives access to the curvature of U_{2NN}/U_{2N} at $\mathrm{De} = 0$ (this is equivalent to taking the first derivative of the speed ratio with respect to De^2). If that curvature is positive, then faster swimming occurs in the neighbourhood of $\mathrm{De} = 0$. As we always have $\beta < 1$, the curvature is positive if there is a sign difference between the sums in Eqs. (3.31)-(3.33) and therefore a sufficient condition for enhanced swimming is the kinematic condition

$$\left[\sum_{n\geq 1} u_n\right] \times \left[\sum_{n\geq 1} n^2 u_n\right] < 0. \tag{3.34}$$

In order to achieve the condition in Eq. (3.34), waves travelling in opposite directions are required. Indeed, for example if all u_n are positive, then it is easy to see from Eq. (3.30) that each u_n mode decreases in amplitude, resulting in an overall decrease

in magnitude of the speed. If there are waves travelling in both direction, i.e. at least one $\alpha_{-n} \neq 0$ and one $\alpha_{+n} \neq 0$, then they need different combinations of amplitudes and frequencies in order to satisfy the condition in Eq. (3.34). Hence a forwards and backwards swimming waves are required.

Physically, the increase in swimming speed between Newtonian and viscoelastic fluids seen here arises from the fact that the damping caused by a non-zero Deborah number affects modes with different frequencies differently. Specifically, the damping term of the form $(1 + n^2\beta\mathrm{De}^2)/(1 + n^2\mathrm{De}^2)$ decreases monotonically with n. Modes with higher frequencies are therefore damped more than those with lower values of n, which provides a mechanism for enhanced swimming.

For illustration, consider two waves travelling in opposite directions with the high-frequency (n) wave travelling along the $-x$ direction ($u_n < 0$) and the low-frequency (m) one along the $+x$ direction ($u_m > 0$). Then their respective amplitudes be such that the resulting Newtonian swimming speed is positive, $U_{2N} > 0$. In the viscoelastic fluid, the u_n wave will be damped more than the u_m wave, as $n > m$. On one hand, decreasing the magnitude of the u_n wave will increase the swimming speed while on the other hand, decreasing the u_m mode will hinder the swimming velocity – it is thus a matter of relative decrease. If the wave amplitudes are such that the gain found by the damping of the u_n wave more than compensates for the damping of the u_m wave, then the non-Newtonian swimming speed will be above the Newtonian one, $U_{2NN} > U_{2N}$. If the wave amplitudes are such that $U_{2N} < 0$, then a similar reasoning might be used to lead to $U_{2NN} > 0$ and in that case, viscoelasticity might lead to a reversal of the direction of locomotion.

3.4 Superposition of two travelling waves: continuous enhancement

We now consider in detail simple cases. We start by swimming using two travelling waves, and show that in this case the sufficient condition described above is in fact necessary: when enhancement takes place, it will lead to faster swimming for all Deborah numbers below a critical value. In order to analytically describe situations where faster swimming can occur, two simple waveforms each containing two waves travelling in opposite directions will be considered. Clearly these two travelling waves must have different frequencies, otherwise they are both damped in the same proportion by viscoelasticity and the swimming speed decreases with respect to the Newtonian case.

3.4.1 Superposition of two travelling waves with identical wave speeds

An example of two waves with different frequencies modes, amplitudes, and wave direction but identical magnitude of wave speed is given by

$$y(x,t) = \epsilon\left[\alpha\sin(x-t) + \sin n(x+t)\right], \tag{3.35}$$

where α is the dimensionless ratio of amplitudes between the two waves. Using Eqs. (3.30) and (3.31) for the sinusoidal waveform in Eq. (3.35) we get the second-order Newtonian swimming speed as

$$U_{2N} = \frac{1}{2}(\alpha^2 - n^2), \tag{3.36}$$

while the second-order non-Newtonian swimming speed is given by

$$U_{2NN} = \frac{\alpha^2}{2}\left(\frac{1+\beta\mathrm{De}^2}{1+\mathrm{De}^2}\right) - \frac{n^2}{2}\left(\frac{1+n^2\beta\mathrm{De}^2}{1+n^2\mathrm{De}^2}\right). \tag{3.37}$$

To find where faster swimming occurs, we compute as above the second derivative of the swimming ratio, U_{2NN}/U_{2N} with respect to De at $\mathrm{De} = 0$, giving

$$\frac{\partial^2}{\partial\mathrm{De}^2}\left(\frac{U_{2NN}}{U_{2N}}\right)\bigg|_{\mathrm{De}=0} = 2(\beta-1)\left(\frac{\alpha^2-n^4}{\alpha^2-n^2}\right). \tag{3.38}$$

This is positive (i.e. upwards curving from $U_{2NN}/U_{2N} = 1$) when $n < \alpha < n^2$. Hence faster swimming requires the relative amplitude between the two waves to lie in a precise interval. If α is too small the behavior is dominated by the $-x$ wave while if it is too large the dynamics is dominated by the $+x$ wave. At higher modes, the range of amplitudes available to the swimming sheet that can produce faster swimming in a non-Newtonian environment compared to a Newtonian one is increased.

We illustrate in Fig. 3.2 these results numerically. We plot the ratio of swimming velocities, U_{2NN}/U_{2N}, as a function of the Deborah number, De, for a range of values of both n and α. We choose a fixed value of $\beta = 0.1$. The computational results confirm that when enhanced swimming is obtained, the speed ratio first increases in the neighbourhood of $\mathrm{De} = 0$ before monotonically decreasing to β. This validates the curvature analysis as a method for predicting enhanced swimming, and indeed faster swimming in a non-Newtonian fluid is seen in the range $n < \alpha < n^2$. An illustration of travelling wave that swims faster in a non-Newtonian fluid is shown in Fig. 3.3,

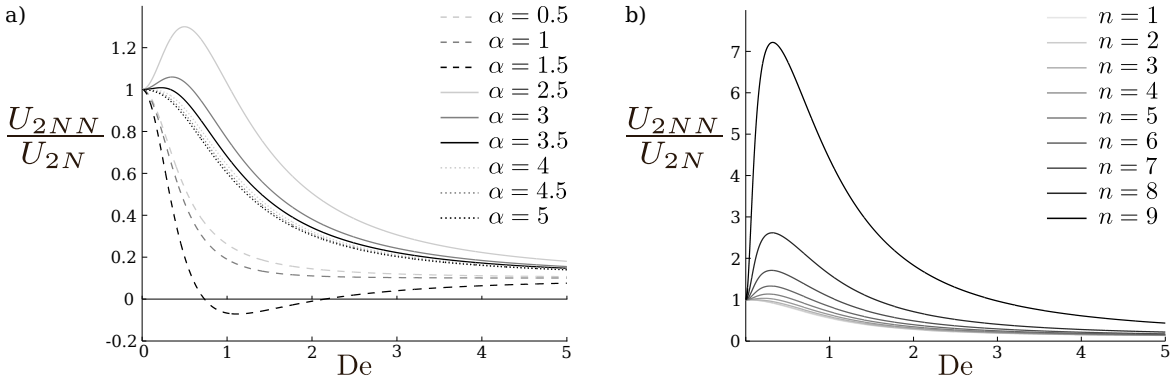

Fig. 3.2 Ratio between the non-Newtonian swimming speed U_{2NN}, and the Newtonian value U_{2N}, as a function of the Deborah number, De, for various values of the relative wave amplitude α, and frequency ratio n, in the waveform from Eq. (3.35). Here we have chosen $\beta = 0.1$. Left: fixed value of $n = 2$ and a range of α values (between 0.5 and 5) where $\alpha = n$ is excluded as Newtonian swimming is zero. Right: fixed value of $\alpha = 9.5$ and n ranging between $n = 1$ and 9.

with $n = 2$ and $\alpha = 5/2$. This waveform corresponds to the speed ratio shown as the uppermost solid grey line in Fig. 3.2 with a maximum of $U_{2NN} = 1.3$ at $\mathrm{De} = 0.5$.

Further analytical insight can be provided by noting from Fig. 3.2 that the peak swimming speed ratio occurs when De is order one. Dividing the result in Eq. (3.37) by that in Eq. (3.36) and taking a first derivative with respect to De we can compute the value of the Deborah number at which the velocity ratio is extremised. It occurs for two values of De given by

$$\mathrm{De}_{1*} = \sqrt{\frac{n^2 - \alpha}{n^2(\alpha - 1)}} \text{ and } \mathrm{De}_{2*} = 0. \tag{3.39}$$

For α above n^2 the only solution is the maximum value of 1 occurring at $\mathrm{De}_{2*} = 0$. When α crosses below n^2 a maximum is created near $\mathrm{De}_{1*} = 0$, and increases as α decreases. When $\alpha = n$ a transition occurs where De_{1*} changes from a maximum point ($n < \alpha$) to a minimum ($\alpha < n$); its value at that point is $\mathrm{De}_{1*} = 1/n$. It remains a minimum until α crosses the value 1, below which the only solution is the maximum of 1 at $\mathrm{De}_{2*} = 0$.

A final point of interest in Fig. 3.2 is the fact, as discussed above, that the ratio between the swimming speeds can become negative. In these cases, the swimmer would then swim in different directions in the Newtonian and non-Newtonian fluids, as was already noted in Ref. [129]. This occurs when $\alpha < n$ such that a swimmer immersed in a Newtonian fluid has negative swimming velocity but there is a range of Deborah

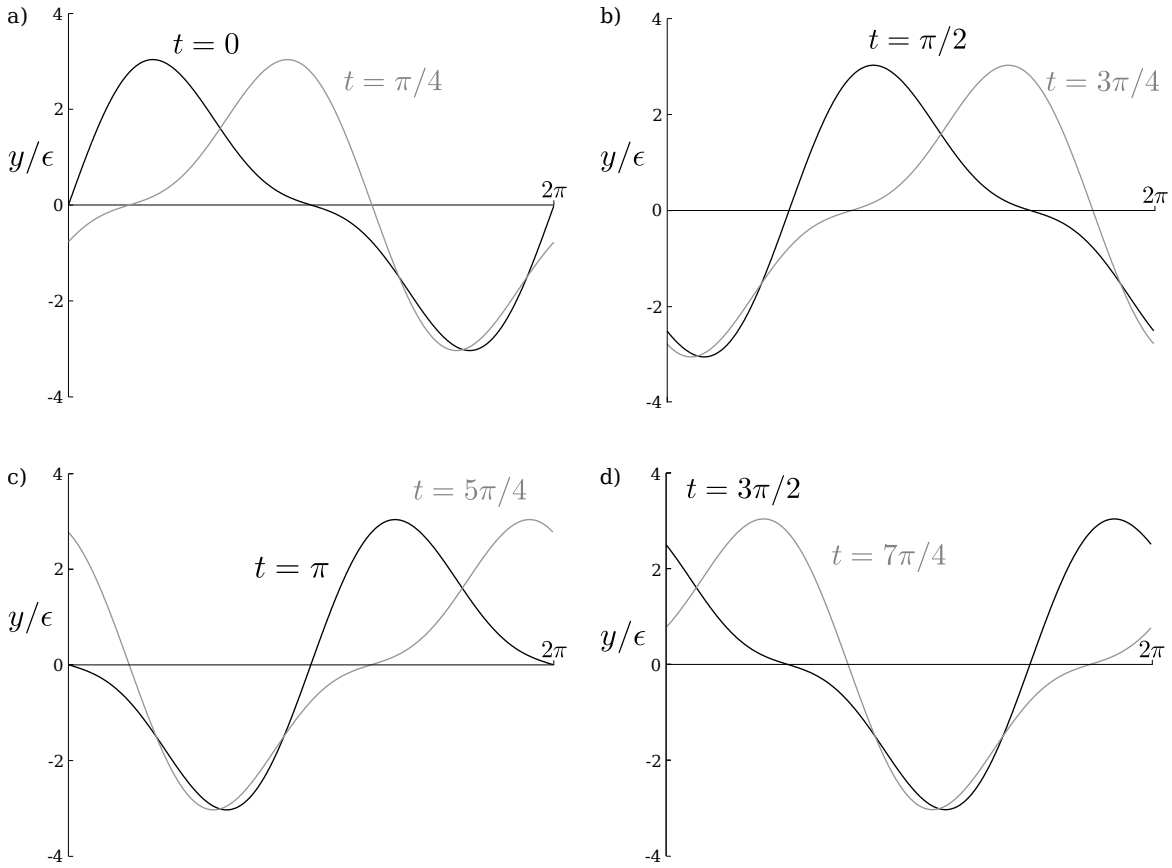

Fig. 3.3 Illustration of a waveform producing faster swimming in a non-Newtonian fluid. The waveform is described by Eq. (3.35) with $\alpha = 5/2$ and $n = 2$, and corresponds to a swimming speed ratio as shown by the uppermost solid grey line in Fig. 3.2a. The black lines in each of the four figures show the waveform at dimensionless times 0, $\pi/2$, π and $3\pi/2$, respectively, and the grey lines show the evolution of the wave an eighth of a period later, to show how the wave travels and changes shape during its period.

numbers for which a swimmer immersed in a non-Newtonian fluid continues to swim forwards. The speed ratio goes through a minimum before increasing back towards β at large Deborah numbers. The reversal of swimming occurs when there is a difference in sign between Eq. (3.36) and Eq. (3.37), which corresponds to the amplitude range

$$\sqrt{\frac{n^2(1+\beta n^2 \mathrm{De}^2)(1+\mathrm{De}^2)}{(1+n^2\mathrm{De}^2)(1+\beta\mathrm{De}^2)}} < \alpha < n. \tag{3.40}$$

This result is reminiscent of a recent study on reciprocal (time-reversible) motion in a worm-like micellular solution, which showed that the direction and the speed of the swimmer could be changed when distinct Deborah numbers are reached [160].

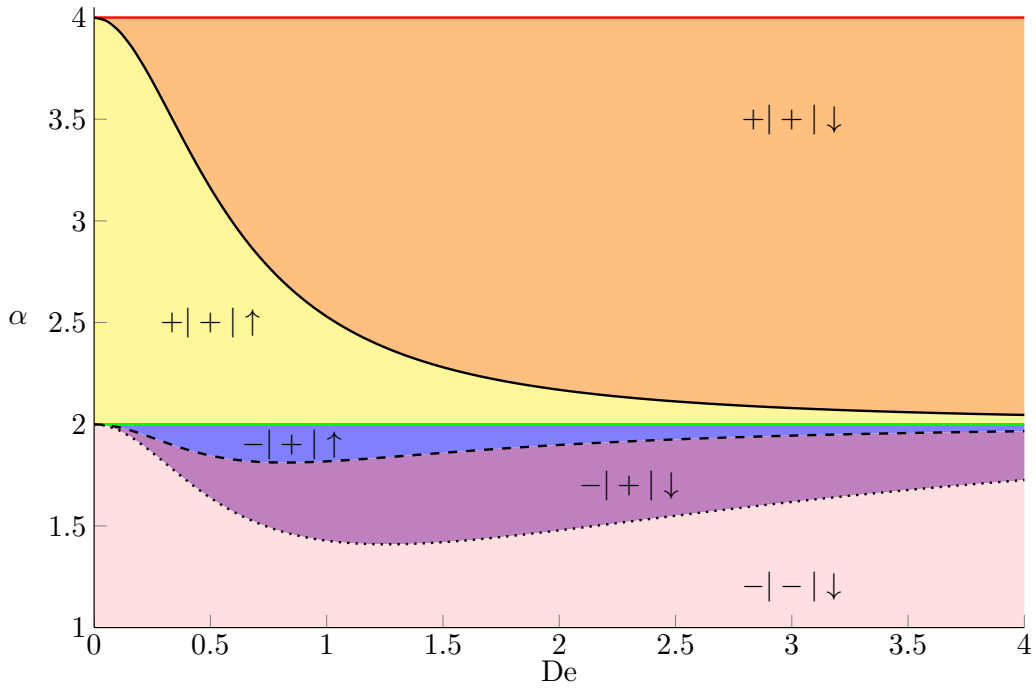

Fig. 3.4 A phase diagram for enhanced or hindered, backwards or forward swimming with the waveform Eq. (3.35) with fixed $n = 2$. The +/- symbols represent forwards and backwards swimming respectively, while up or down arrows represent enhanced or hindered motion respectively. In each section of the phase diagram we list Newtonian swimming direction | non-Newtonian swimming direction | enhanced or hindered, respectively. The red line shows the upper bound on α, above this value no enhanced swimming can occur. The dashed and dotted lines show the lower bounds of Eq. (3.41) and Eq. (3.40) respectively.

Finally, we can also find a range of a values for which the swimmer will not only change direction but will also swim with a larger magnitude, which occurs when

$$\sqrt{\frac{n^2(2+n^2\mathrm{De}^2+\beta n^2\mathrm{De}^2)(1+\mathrm{De}^2)}{(1+n^2\mathrm{De}^2)(2+\mathrm{De}^2\beta\mathrm{De}^2)}} < \alpha < n. \tag{3.41}$$

Here the swimming speed ratio becomes negative and less than -1. Together with the condition for enhanced swimming we plot a phase diagram, showing where the non-Newtonian swimmer swims in a different direction or swims faster than its Newtonian counterpart, as shown in Fig. 3.4. As the main focus of this thesis is faster swimming, we limit ourselves to the cases where Newtonian swimming is positive and look for non-Newtonian enhancement in the same direction.

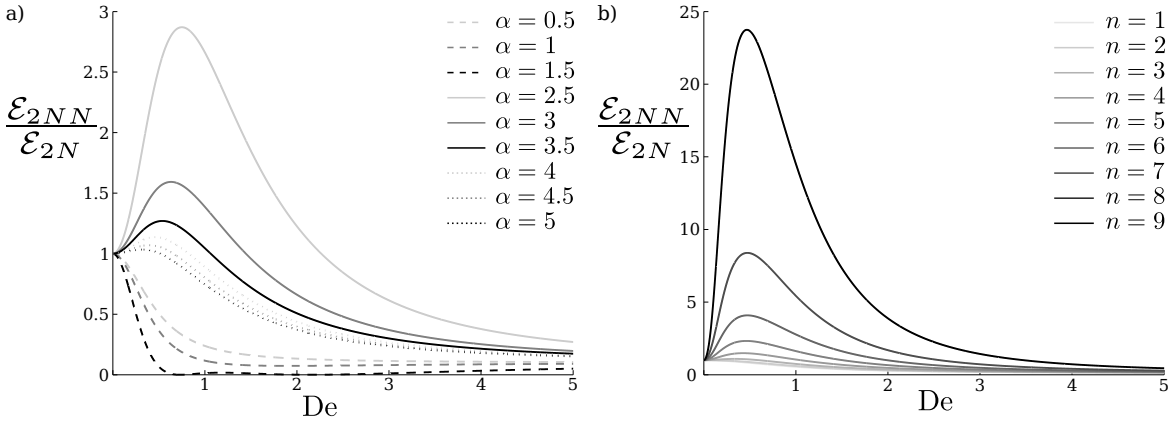

Fig. 3.5 Ratio of the swimming efficiency in a non-Newtonian fluid compared to its Newtonian counterpart as a function of De: (a) $n = 2$ for a range of values of α; (b) $\alpha = 9.5$ and $1 \leq n \leq 9$. The waveform is the one described in Eq. (3.35).

3.4.2 Necessary vs. sufficient condition for enhanced swimming

The sufficient condition for enhancement, shown in Eq. (3.34), detailed the conditions required for an upwards curving of the swimming speed ratio from zero Deborah number. In order to study if this sufficient condition is also necessary, we search analytically for the conditions leading to $U_{2NN} > U_{2N}$, in the case of a two wave swimmer, leading to

$$0 < \mathrm{De} < \sqrt{\frac{n^4 - \alpha^2}{n^2(\alpha^2 - n^2)}} \equiv \mathrm{De}_a. \tag{3.42}$$

This condition requires $n < \alpha < n^2$, and defines the range of Deborah number where forward swimming enhancement is achieved, namely $[0, \mathrm{De}_a]$. If we enforce the curvature to be negative then we cannot find a set of viable parameters for which $U_{2NN} > U_{2N} > 0$, thus showing that the sufficient condition is also necessary when two modes are considered: in the case of two waves, if forward swimming enhancement is ever to be obtained, it will take place for any Deborah number below a critical value De_a.

3.4.3 Swimming efficiency

We now turn to energetic considerations. The rate of viscous dissipation in the fluid as the sheet is swimming is equal to the volume integral of $\boldsymbol{\tau} : \dot{\boldsymbol{\gamma}}$ in the fluid. At leading order we therefore have to integrate $\boldsymbol{\tau}_1 : \dot{\boldsymbol{\gamma}}_1$. With the general waveform in

Eq. (3.1), the dimensional second-order dissipation rate in the non-Newtonian fluid per unit length in the $\hat{\mathbf{z}}$ direction is easily found and we obtain $W = \epsilon^2 W_{2NN} + \dots$ with

$$W_{2NN} = \sum_{n\geq 1}\sum_{m\geq 1} 8\pi\eta\omega^2 m n^2 \left(\frac{1+n^2\beta\mathrm{De}^2}{1+n^2\mathrm{De}^2}\right)\left(|\alpha_{n,m}|^2 - |\alpha_{n,-m}|^2\right). \tag{3.43}$$

The result in Eq. (3.43) should then be compared with its Newtonian counterpart.

Let us consider for illustration the waveform in Eq. (3.35). In that case, the ratio of the work done against the non-Newtonian fluid compared to the Newtonian one is given by

$$\frac{W_{2NN}}{W_{2N}} = \frac{\eta}{\eta_N(n^3+\alpha^2)}\left[\alpha^2\left(\frac{1+\mathrm{De}^2\eta_s/\eta}{1+\mathrm{De}^2}\right) + n^3\left(\frac{1+n^2\mathrm{De}^2\eta_s/\eta}{1+n^2\mathrm{De}^2}\right)\right], \tag{3.44}$$

where η_N is the Newtonian viscosity. In order to contrast the locomotion in the polymeric fluid with that in the solvent alone, we then take $\eta_N = \eta_s$. Furthermore, as is done traditionally [22], the swimming efficiency is defined as

$$\mathcal{E} = \frac{\eta U^2}{W}\cdot \tag{3.45}$$

In order to compare the efficiency of swimming in the different fluids, we compute the ratio

$$\frac{\mathcal{E}_{2NN}}{\mathcal{E}_{2N}} = \frac{\eta U_{2NN}^2}{W_{2NN}}\frac{W_{2N}}{\eta_N U_{2N}^2}\cdot \tag{3.46}$$

The ratio of the work and viscosity in the two different fluids, $\eta W_{2N}/\eta_N W_{2NN}$, is always greater than 1 for non-zero Deborah number, meaning that when the swimming speed ratio U_{2NN}/U_{2N} is greater than 1, the swimming efficiency is automatically always increased. Increased efficiency may allow a swimmer to propel itself faster in a non-Newtonian fluid compared to a Newtonian one. If we consider a swimmer with fixed energy output, then the non-Newtonian swimmer may be able to use the excess energy output. Due to the decrease in work needed to be done on the fluid, excess flagellum molecular motors could work to increase the swimmer amplitude or increase swimmer frequency both of which would increase the swimming speed compared to a smaller amplitude or slower beating swimmer in the same fluid. To directly compare swimming speeds taking into account energy considerations we need a model that includes the internal actuation of the molecular motors inside the flagellum, and their energetic considerations.

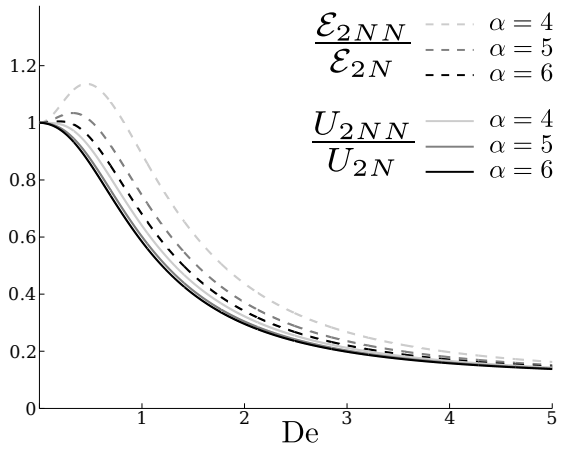

Fig. 3.6 Three example waveforms are shown for which the swimming speed is not enhanced but the efficiency is. The relative amplitude in Eq. (3.35) lies outside the range $n < \alpha < n^2$ $(n = 2)$.

We plot the ratio of efficiencies against De for a range of relative wave amplitude α, and wavenumber ratio n, in Fig. 3.5, where $\eta_s/\eta = \beta = 0.1$. Clearly, an increase in swimming speed is correlated with an increase in efficiency, but increased efficiencies can in fact be obtained without enhanced swimming. Indeed, from Eq. (3.46), increased efficiency is obtained as soon as

$$\left(\frac{U_{2NN}}{U_{2N}}\right)^2 > \frac{\eta_N W_{2NN}}{\eta W_{2N}}. \tag{3.47}$$

Given that the right-hand side of Eq. (3.47) is less than one, the condition for enhanced efficiency does not require enhanced swimming. Specifically, using the illustrative sinusoidal waveform of Eq. (3.35), we obtain an improved efficiency when

$$\frac{(n^3+\alpha^2)}{(\alpha^2-n^2)^2} > \frac{\left[\alpha^2\left(\frac{1+\beta\mathrm{De}^2}{1+\mathrm{De}^2}\right)+n^3\left(\frac{1+\beta n^2\mathrm{De}^2}{1+n^2\mathrm{De}^2}\right)\right]}{\left[\alpha^2\left(\frac{1+\beta\mathrm{De}^2}{1+\mathrm{De}^2}\right)-n^2\left(\frac{1+\beta n^2\mathrm{De}^2}{1+n^2\mathrm{De}^2}\right)\right]^2}, \tag{3.48}$$

for which $n < \alpha < n^2$ is not a necessary condition. This result is illustrated in Fig. 3.6 in the case $n = 2$. When $\alpha > n^2$, the waveform travels in the same direction in both fluids and the swimmer is always faster in a Newtonian fluid although it is more efficient in the non-Newtonian one for a range of Deborah numbers.

3.4.4 Two waves with identical wavelengths

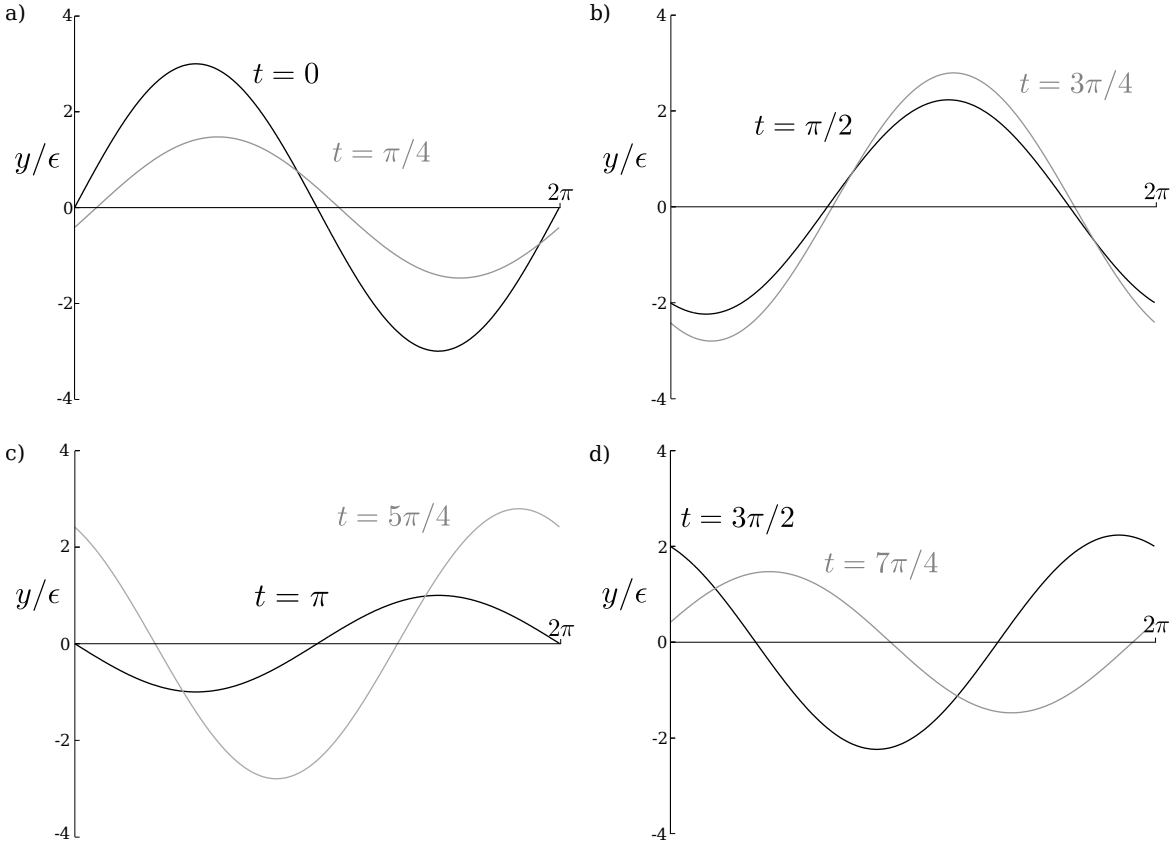

Fig. 3.7 Illustration of a waveform from Eq. (3.49) with $\alpha = 2$ and $n = 2$ that produces faster swimming in a non-Newtonian fluid. The black lines in each of the four figures show the waveform at dimensionless times 0, $\pi/2$, π and $3\pi/2$, respectively, and the grey lines show the evolution of the wave an eighth of a period later.

Instead of two waves with identical wave speeds, enhanced swimming can also be obtained in a combination of waves with identical wavelengths. Since the waves need to have different frequencies, then they necessarily have different wave speeds. As an example we consider here the waveform

$$y = \epsilon[\alpha \sin(x - t) + \sin(x + nt)]. \tag{3.49}$$

This gives

$$U_{2NN} = \frac{\alpha^2}{2}\left(\frac{1 + \beta \mathrm{De}^2}{1 + \mathrm{De}^2}\right) - \frac{n}{2}\left(\frac{1 + n^2\mathrm{De}^2}{1 + n^2\mathrm{De}^2}\right), \tag{3.50}$$

and

$$U_{2N} = \frac{1}{2}(\alpha^2 - n). \tag{3.51}$$

Similarly as above, the second derivate of U_{2NN}/U_{2N} at $\mathrm{De} = 0$ is given by

$$\frac{\partial^2}{\partial \mathrm{De}^2}\left(\frac{U_{2NN}}{U_{2N}}\right)\bigg|_{\mathrm{De}=0} = \left(\frac{\alpha^2 - n^3}{\alpha^2 - n}\right)(\beta - 1), \tag{3.52}$$

and faster swimming occurs when

$$n^{1/2} < \alpha < n^{3/2}, \tag{3.53}$$

which is confirmed by numerical computations (not shown). A waveform leading to enhanced swimming in this case is illustrated in Fig. 3.7, in the case $\alpha = 2$ and $n = 2$. This corresponds to a maximum speed enhancement of $U_{2NN}/U_{2N} \approx 1.1$ at Deborah number $\mathrm{De} \approx 0.4$. To obtain the optimal Deborah number, we extremise the ratio of swimming speeds to find the peaks occurring at

$$\mathrm{De}_{1*} = \sqrt{\frac{n^2 - \alpha\sqrt{n}}{n^2(\alpha\sqrt{n} - 1)}} \text{ and } \mathrm{De}_{2*} = 0, \tag{3.54}$$

with a behavior qualitatively similar to that of the last section.

3.5 Superposition of three travelling waves: continuous vs. discrete enhancement

In the previous sections, where the superposition of two waves was considered, we saw that when enhancement is present, it is continuous from $\mathrm{De} = 0$ to an order one Deborah number De_a, where the value $\mathrm{De}_a \neq 0$ is the only non-zero solution of $U_{2NN}/U_{2N} = 1$. We now demonstrate that if the swimmer is able to use a third travelling wave, it is possible for swimming enhancement to occur only when a finite amount of viscoelasticity is present, i.e. for values of the Deborah number in the range $[\mathrm{De}_b, \mathrm{De}_c]$, where De_b and De_c are both non-zero.

We consider, for illustration purposes, a waveform with three modes $1 < n_2 < n_3$. The corresponding speeds u_1, u_{n_2} and u_{n_3} are re-scaled by u_1 so that we take $u_1 = 1$. Using the same notation as above, the Newtonian swimming speed is then given by

$$U_{2N} = 1 + u_{n_2} + u_{n_3}. \tag{3.55}$$

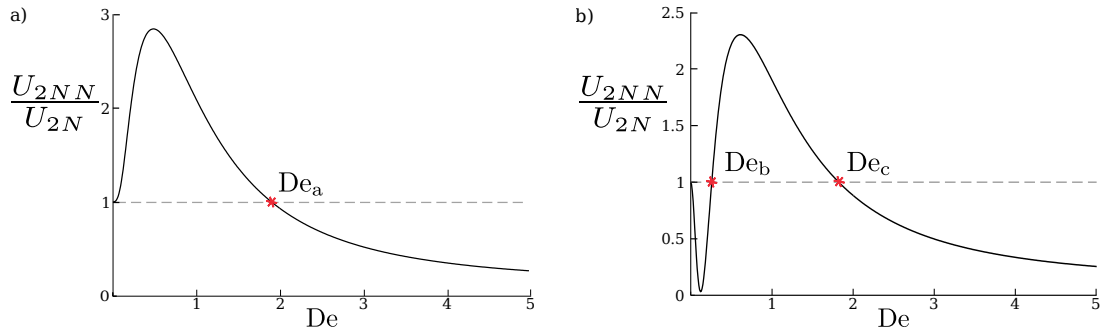

Fig. 3.8 Two different types of enhancement are shown for two different three-mode waves with $n_1 = 1$, $n_2 = 4$ and $n_3 = 8$: (a) continuous enhancement from zero Deborah number in the range $[0, \mathrm{De}_a]$ with $\mathrm{De}_a \approx 1.9$ ($u_{n_1} = 1$, $u_{n_2} = -1$, $u_{n_3} = 0.3$); (b) enhancement in a discrete, finite, range of Deborah numbers, $[\mathrm{De}_b, \mathrm{De}_c]$, where $\mathrm{De}_b \approx 0.3$ and $\mathrm{De}_c \approx 1.8$ ($u_{n_1} = 1$, $u_{n_2} = -2$, $u_{n_3} = 1.2$).

The difference between the non-Newtonian and Newtonian swimming speeds is then found to be

$$U_{2NN} - U_{2N} = \mathrm{De}^2(\beta - 1)\left[\left(\frac{1}{1+\mathrm{De}^2}\right) + \left(\frac{n_2^2 u_{n_2}}{1+n_2^2\mathrm{De}^2}\right) + \left(\frac{n_3^2 u_{n_3}}{1+n_3^2\mathrm{De}^2}\right)\right]. \quad (3.56)$$

Focusing on cases where $U_{2N} > 0$, enhanced forward swimming is found when Eq. (3.56) is positive. As shown in Fig. 3.8 numerically for $n_2 = 4$ and $n_3 = 8$, there are two types of enhancements possible: either on a range $[0, \mathrm{De}_a]$ where the velocity ratio curves upward at the origin (continuous enhancement, Fig. 3.8a, as in § 3.4) or on a range $[\mathrm{De}_b, \mathrm{De}_c]$ for which the curvature at $\mathrm{De} = 0$ is initially negative before curving upward as the viscoelasticity increases (discrete enhancement, Fig. 3.8b). As the swimming speed ratio is a continuous function there is a continuous transition between these two types of enhancement.

In order to distinguish between them analytically, we observe that when the curvature is negative, we can either have no enhancement or enhancement at a finite Deborah number. Hence, we need to search for cases where Eq. (3.56) is positive, given that the curvature at the origin is negative. The curvature of the general wave was obtained in Eq. (3.33), hence for negative curvature in our three-mode waveform we require

$$\kappa = 2(\beta - 1)(1 + n_2^2 u_{n_2} + n_3^2 u_{n_3}) < 0. \quad (3.57)$$

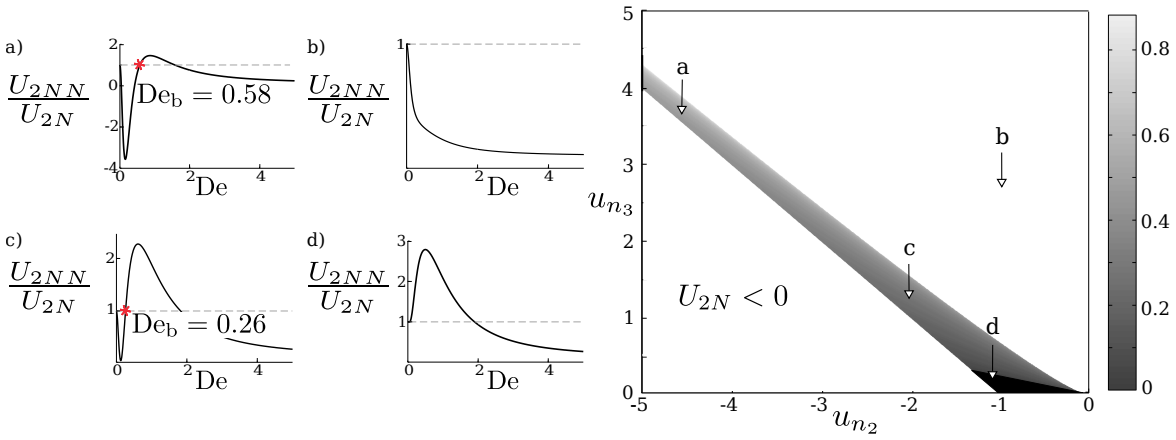

Fig. 3.9 Regions in the parameters space $\{u_{n_2}, u_{n_3}\}$ where enhanced swimming occurs. The black section represents where the curvature is positive (*i.e.* upwards curving) so that from infinitesimally small Deborah number we get an increase in the swimming speed. In contrast, the grey scale section shows regions where enhanced swimming is obtained despite negative curvature at the origin. The grey scale color scheme quantifies the value of non-zero Deborah numbers at which the increase in swimming speed first occurs, De_b, from low Deborah number in dark, to high Deborah number (≈ 0.8) in light grey. Results are shown for $n_2 = 4$ and $n_3 = 8$. The sub-figures a-d show the swimming speed ratio as a function of Deborah number for each of the corresponding labels indicating different u_{n_2} and u_{n_3} within the parameter space plot.

The result in Eq. (3.56) can then be written in terms of U_{2N} and κ as

$$n_2^2 n_3^2 \mathrm{De}^4(\beta - 1)\left(\frac{n_2^2 + n_3^2 - 1}{n_2^2 n_3^2} + u_{n_2} + u_{n_3}\right) > \left[\mathrm{De}^2\kappa(\tfrac{1}{2} + \mathrm{De}^2) + n_2^2 n_3^2 \mathrm{De}^4(\beta - 1)U_{2N}\right]. \tag{3.58}$$

As $\beta - 1 < 0$, and assuming that $U_{2N} > 0$ and $\kappa < 0$, the minimum requirement for non-continuous enhancement is

$$\frac{n_2^2 + n_3^2 - 1}{n_2^2 n_3^2} + u_{n_2} + u_{n_3} < 0. \tag{3.59}$$

The three conditions given by Eqs. (3.55) ($U_{2N} > 0$), (3.57), and (3.59) can be satisfied simultaneously only when $u_{n_2} < 0$ and $u_{n_3} > 0$, *i.e.* the first and third modes must have a different sign to the second mode. We then search numerically over the domain $\{u_{n_2} < 0,\, u_{n_3} > 0\}$ and De to obtain the regions where Eq. (3.56) is positive provided $U_{2N} > 0$ and $\kappa < 0$, in the example case $n_2 = 4$ and $n_3 = 8$. The values of u_{n_2} and u_{n_3} fitting these conditions are shown in Fig. 3.9 (grey scale domain) while the region showing continuous enhancement is shown in black. The grey scale colouring

scheme used in Fig 3.9 displays the value of the lower bound in the interval, De_b, from low (dark grey) to high (light grey) values. For three waves, in contrast to the case of two waves, situations exist therefore where a finite amount of viscoelasticity is required to get enhanced propulsion, $\mathrm{De} > \mathrm{De}_b > 0$ (analysis for four and five mode waves show similar results and are not shown here).

3.6 Discussion

Motivated by the non-Newtonian environment in which many swimmers propel themselves *in vivo*, in this Chapter, we have calculated the speed of Taylor's swimming sheet in a Newtonian and an Oldroyd-B (non-Newtonian) fluid, in the small-amplitude limit. In contrast to previous analytical studies, we found that small-amplitude travelling waves can produce faster swimming in a non-Newtonian fluid compared to a Newtonian fluid when there are waves travelling in opposite directions in different frequency modes and with different amplitudes. Physically, in a non-Newtonian fluid the waves in higher frequency modes are damped more than those in lower frequency modes, increasing the overall speed of the wave under conditions placed upon the difference in frequency and amplitude of the summed waveforms. The efficiency of the wave can also be increased, and the direction of swimming can sometimes be reversed. By studying in detail the superposition of two or three travelling waves, we also showed that the range of Deborah number in which the enhancement of the swimming speed takes place can either include the origin, in which case any small amount of viscoelasticity will lead to faster swimming, or it may be a finite interval which does not include the origin, meaning that faster locomotion requires a finite amount of viscoelasticity.

The results in this Chapter are reminiscent of recent experimental and theoretical work on the role of inertia in locomotion, where two important questions have been addressed: (1) for a non-swimmer at zero Reynolds numbers, how much inertia is needed to make it swim? and (2) how does the locomotion speed of a Stokesian swimmer vary with inertia? The answer to question (1) depends crucially on the geometry and actuation of the swimmer and both discrete [161, 162] and continuous [163] transition to swimming were obtained. In response to question (2), model organisms called squirmers were shown to vary their speed monotonically from zero Reynolds number [164, 165]. Similarly, in our results where the inertia effects are replaced by non-Newtonian effects, we showed that a careful design of the swimming kinematics could lead to either a decrease or an increase, which could be continuous or discrete, of the locomotion speed. We expect that these results will remain valid for more realistic models of swimming

organisms, in particular those including features such as large-amplitude, finite-size, and three-dimensional effects.

In three-dimensions, the same frequency-dependent damping term as the one in Eq. (3.28) is present for infinite cylindrical swimmers [52], hence similar results are expected to hold. With regards to finite sized swimmers, backward propagating waves are expected to occur due to the finite nature of real flagella. Previous computational studies have shown that the addition of viscoelasticity decreases the backwards motion of a finite swimmer [126] due to the presence of a viscoelastic network behind the swimmer. The opposite has been observed experimentally for nematodes where hyperbolic stresses created along the swimmer hinder propulsion [112]. It is yet unclear how our theoretical results would extend to a finite swimmer, though we may expect that the mechanism provided in this Chapter would provide an additional contribution to the swimming speed. In the case of multiple swimmers, it would be interesting to investigate how waves with both high and low frequency modes affect one another and potentially synchronise. From Ref [133] we expect the synchronisation rate to increase with the frequency of the waves however the generalisation to multiple modes in viscoelastic fluids has yet to be done. A recent study addresses a related issue in the Newtonian case [166].

The waveforms produced here offer insight into how swimming speeds can be increased in fluids with viscoelastic properties often found in nature [86]. Can these shape kinematics occur in biology? For eukaryotic flagellar swimming this requires understanding of how the stochastic actuation of molecular motors create waveforms. Dynein, the motor protein causing flagella bending, has been proposed to have two distinct modes to create oscillatory bending - these can be described as active and passive, or forward and reverse active modes [49], leading to travelling waves that can propagate up or down the flagellum. Due to the finite nature of flagella the wave is reflected back off the tail end or basal body, thus creating passive backwards waves [47]. Experiments on *Drosophila* spermatozoa show that the cells use actively created forwards and backwards flagellar waves to avoid obstacles [167]. Furthermore by solving elastohydrodynamic force balance equations on infinite flagella analytic studies have shown two different modes of waves travel along the flagella with the same frequency, but different amplitudes and directions [168]. Hence a flagellum naturally creates forward and backward travelling waves with different amplitudes. The enhancement described in this Chapter requires however waves with different frequencies travelling in the backwards direction for enhancement to occur. The addition of higher frequency modes ($n = 2$ and $n = 3$), found in small amounts

in beating spermatozoa [169], would not however lead to an increase in swimming speed as $u_n > 0$ for all values of n found experimentally. Changes in flagella beating frequency can occur by altering the environment in which the swimmer propagates, for example hyperactivation when mammalian spermatozoa reach the ovum, leading to a reduction in the beat frequency and increase in the beat amplitude [170]; a variation in ATP or salt concentrations also change frequencies [49]. Recent work on the unsteady modes of flagellar motion show that most modes have a frequency smaller than the fundamental frequency, and hence would correspond to a reduced swimming speed [171]. The addition of noise to the molecular motor oscillations, either through variations in concentrations in the bulk or variations between motors, could lead to increased swimming provided the coherent noise is large enough for the flagellum to access a higher frequency mode, however this is larger than the noise measured [172]. Backwards travelling wave results have been described for muscle-actuated planar motion occurring for example in the nematode *Caenorhabditis elegans* [53] as well as other flagellar systems such as the green alga *Chlamydomonas reinhardtii* [173].

While our study offers only an idealised view, and although as of yet there are no experimental studies from biology for which the model here would predict faster swimming, our work address the most general periodic waving deformation and points to the use of multiple waves travelling in different directions as a mechanism allowing control of swimming speed and direction in complex environments.

4

Active swimming in viscoelastic fluids

4.1 Introduction

From these rigid swimmer studies we move to flexible swimmers. Instead of prescribing the shape of the flagellar deformation we solve for the waveform of the swimmer as a balance between the fluid stresses and the internal driving and resisting forces. Through this force balance, we propose a dynamic mechanism for swimming enhancement in a viscoelastic fluid. We then show that this dynamic balance leads to a generic transition from hindered rigid swimming to enhanced flexible locomotion.

4.2 Waving motion in viscoelastic fluids

In this section we briefly recap Taylor's swimming sheet [9] (Fig. 3.1) and Oldroyd-B fluids [87].

We consider active deformations of Taylor's two-dimensional waving model as introduced in Chapter 3. The extension to the case of three dimensional filaments is presented later in this Chapter, with similar results. Again, the sheet is embedded in a viscous fluid, and due to internal actuation is made to deform its shape as a traveling wave of frequency ω, amplitude a, wave number k, and wave speed $V = \omega/k$, and self-propels as a result with speed U in the opposite direction. The flat sheet is in the $\hat{\mathbf{x}} - \hat{\mathbf{z}}$ plane, such that deformations away from this flat state occur in the $\hat{\mathbf{y}}$ direction.

We similarly apply the incompressible Cauchy equations, $\nabla \cdot \boldsymbol{\tau} = \nabla p$, $\nabla \cdot \mathbf{u} = 0$, with p the pressure, $\mathbf{u}$ the velocity field, and $\boldsymbol{\tau}$ the deviatoric stress. We define a stream function ψ such that $u_x = \partial\psi/\partial y$ and $u_y = -\partial\psi/\partial x$, to enforce incompressibility.

The total deviatoric stress, $\boldsymbol{\tau}$, satisfies the Oldroyd-B constitutive equation described in Chapter 3,

$$\boldsymbol{\tau} + \lambda \overset{\triangledown}{\boldsymbol{\tau}} = \eta\dot{\boldsymbol{\gamma}} + \eta_s\lambda \overset{\triangledown}{\dot{\boldsymbol{\gamma}}}, \tag{4.1}$$

where the total viscosity is $\eta = \eta_s + \eta_p$ and where $\dot{\boldsymbol{\gamma}} = \nabla\mathbf{u} + \nabla\mathbf{u}^T$ is the shear rate tensor. In Eq. (4.1), we used $\overset{\triangledown}{\mathbf{A}}$, to denote the upper convected derivative for any tensor $\mathbf{A}$, defined in Eq. 3.7. An important factor in the derivations below will be $\beta = \eta_s/\eta < 1$, ratio of solvent to total viscosity. The relative importance of viscoelasticity is quantified by the Deborah number, $\mathrm{De} = \lambda\omega$, the ratio of the relaxation time of the polymers immersed in the fluid λ, to the relevant time-scale of the waving motion of the sheet ω^{-1}.

4.3 Swimming speed

Assuming that the waveform of the sheet is known, we first solve for the external fluid dynamics. The height of the sheet is written as $y(x,t) = \epsilon y_1(x,t) + \epsilon^2 y_2(x,t) + \ldots$, where $\epsilon \ll 1$ denotes the dimensionless waving amplitude. The leading-order shape, y_1, is decomposed as

$$y_1(x,t) = \mathrm{Re}\left[\sum_{n\geq 1} a^{(n)} e^{in(kx-\omega t)}\right], \tag{4.2}$$

where Re denotes the real part, and $a^{(n)}$ is the amplitude of the nth Fourier mode. Using the Fourier notation $A = \mathrm{Re}\left[\sum_{n\geq 1} \tilde{A}^{(n)} e^{-in\omega t}\right]$ to describe the nth mode $\tilde{A}^{(n)}$ of a time-periodic function A, we thus have $\tilde{y}_1^{(n)} = a^{(n)} e^{inkx}$.

Denoting by $a_{NN}^{(n)}$ the sheet amplitude in a non-Newtonian (Oldroyd-B) fluid and by $a_N^{(n)}$ the Newtonian one, we can solve for the external fluid dynamics asymptotically in powers of ϵ following the work in Refs. [44, 174]. Swimming is obtained at order ϵ^2, at dimensional speeds in the non-Newtonian (NN) case given by

$$U_{NN} = \tfrac{1}{2}\sum_{n=1}^{\infty} n^2\omega k \left|a_{NN}^{(n)}\right|^2 \left(\frac{1+\beta n^2\mathrm{De}^2}{1+n^2\mathrm{De}^2}\right), \tag{4.3}$$

while in the Newtonian (N) limit we obtain

$$U_N = \tfrac{1}{2}\sum_{n=1}^{\infty} n^2 \omega k \left|a_N^{(n)}\right|^2. \tag{4.4}$$

If the swimmer has identical shape in both fluids, *i.e.* $a_{NN}^{(n)} = a_N^{(n)}$, comparing Eqs. (4.3) and (4.4) shows that we always have $U_{NN} < U_N$ since $\beta < 1$. Thus for a stiff infinite swimmer swimming speed enhancement cannot be achieved. In order to obtain an enhancement of the swimming speed in a viscoelastic fluid, a physical mechanism must thus exist to increase $\left|a_{NN}^{(n)}\right|$ beyond $\left|a_N^{(n)}\right|$. As we show below, solving for the swimmer amplitude by enforcing the correct dynamic balance allows us to obtain a nontrivial dependence of $a_{NN}^{(n)}$ on the Deborah number, and enhancement. As both Eqs. (4.3) and (4.4) are quadratic in the amplitudes $a^{(n)}$, we note that we only need derive the first order shape dynamics.

4.4 Dynamic balance of an active swimmer

For a beating eukaryotic flagellum there are three forces to consider. Firstly, the internal driving due to the spatio-temporal actuation from molecular motors [175]. We model this internal forcing, classically, as due to a time-varying distribution of active bending moments per unit length, $F(x,t)$ [39]. Balancing this actuation are two resisting forces, the external hydrodynamic stresses (pressure and viscous stresses) and the internal solid mechanic resistance (elastic cost to be bent away from a preferred, flat state) [55]. Note that any possible internal dissipation is neglected compared to dissipation in the outside fluid. Denoting the bending stiffness of the sheet κ, the normal force balance at leading order in the amplitude of the sheet deformation is written as

$$-\kappa\nabla^4 y + \hat{\mathbf{n}}\cdot\boldsymbol{\sigma}\cdot\hat{\mathbf{n}}|_S = \nabla^2 F, \tag{4.5}$$

on the surface of the sheet, where $\hat{\mathbf{n}}$ is the unit normal to the sheet at leading order and $\boldsymbol{\sigma}$ the hydrodynamic stress tensor.

In order to determine the hydrodynamic stress, we consider the constitutive equation, Eq. (4.1), at leading order

$$\left(1+\lambda\frac{\partial}{\partial t}\right)\boldsymbol{\tau}_1 = \eta\left(1+\beta\lambda\frac{\partial}{\partial t}\right)\dot{\boldsymbol{\gamma}}_1, \tag{4.6}$$

where we have expanded each quantity in powers of $\epsilon \ll 1$, $\boldsymbol{\tau} = \epsilon\boldsymbol{\tau}_1 + \ldots$; $\dot{\boldsymbol{\gamma}} = \epsilon\dot{\boldsymbol{\gamma}}_1 + \ldots$, etc. Writing Eq. (4.6) using Fourier notation we have

$$\tilde{\boldsymbol{\tau}}_1^{(n)} = \frac{\eta - in\lambda\omega\eta_s}{1 - in\lambda\omega}\tilde{\dot{\boldsymbol{\gamma}}}_1^{(n)} = \frac{1 - in\mathrm{De}\beta}{1 - in\mathrm{De}}\eta\tilde{\dot{\boldsymbol{\gamma}}}_1^{(n)}. \tag{4.7}$$

The first order Stokes equation similarly reduces to

$$\eta\nabla\cdot\tilde{\dot{\boldsymbol{\gamma}}}_1^{(n)} = \frac{1 - in\mathrm{De}}{1 - in\mathrm{De}\beta}\nabla\tilde{p}_1^{(n)}, \tag{4.8}$$

at leading order in ϵ. The pressure is eliminated from the above by taking its curl, leaving the biharmonic equation for the stream function, $\nabla^4\tilde{\psi}_1^{(n)} = 0$. This is solved in Fourier space to obtain the first order stream function as

$$\psi_1 = \mathrm{Re}\left[\sum_{n=1}^{\infty}\frac{\omega}{k}a_{NN}^{(n)}(1 + nky)e^{-nky}e^{in(kx-\omega t)}\right]. \tag{4.9}$$

Notably, the flow described by Eq. (4.9) is the same as the Newtonian solution, hence viscoelasticity does not modify the flow induced by the swimmer at leading order. However, as we see below, it does impact the stress distribution. In order to determine the pressure, we have to integrate Eq. (4.8) using Eq. (4.9) leading to

$$\tilde{p}_1^{(n)} = -2\eta\omega k\left(\frac{1 - in\mathrm{De}\beta}{1 - in\mathrm{De}}\right)in^2a_{NN}^{(n)}e^{-nky}e^{inkx}. \tag{4.10}$$

The hydrodynamic stress tensor, $\boldsymbol{\sigma}$, is given by $\boldsymbol{\sigma} = -p\mathbf{I} + \boldsymbol{\tau}$, which, at leading order, reduces in Fourier space to

$$\tilde{\boldsymbol{\sigma}}_1^{(n)} = -\tilde{p}_1^{(n)}\mathbf{I} + \frac{1 - in\mathrm{De}\beta}{1 - in\mathrm{De}}\eta\tilde{\dot{\boldsymbol{\gamma}}}_1^{(n)}, \tag{4.11}$$

for each Fourier mode n.

With the determination of the fluid stress, Eq. (4.5) can be written in Fourier components as

$$-\kappa\frac{\partial^4\tilde{y}_1^{(n)}}{\partial x^4} - \frac{\partial^2\tilde{F}_1^{(n)}}{\partial x^2} = \tilde{p}_1^{(n)} + 2\eta\left(\frac{1 - in\mathrm{De}\beta}{1 - in\mathrm{De}}\right)\frac{\partial^2\tilde{\psi}_1^{(n)}}{\partial y\partial x}\bigg|_S \tag{4.12}$$

Writing $F_1 = \mathrm{Re}\left[\sum_{n\geq 1} f^{(n)}e^{in(kx-\omega t)}\right]$ to describe the first order contribution to the active bending moment, from Eqs (4.9), (4.10) and (4.12) we can determine the

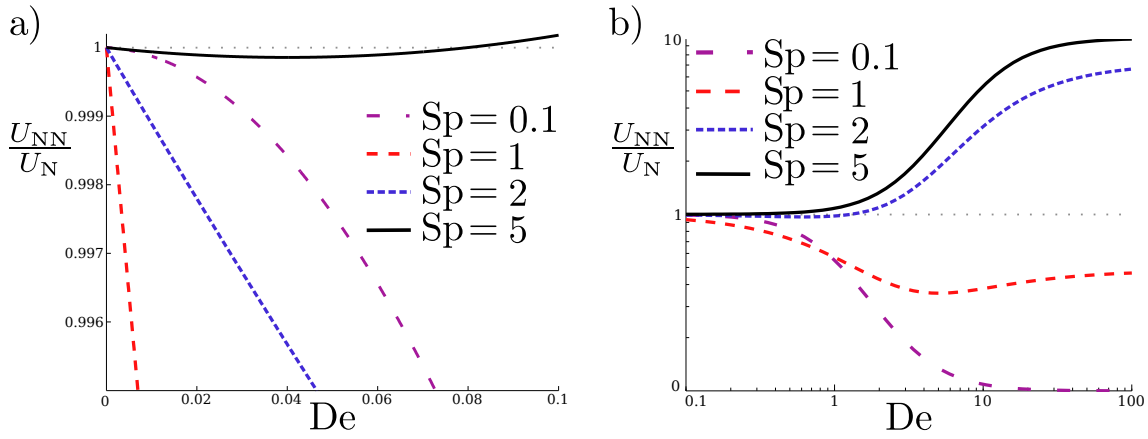

Fig. 4.1 Ratio of non-Newtonian to Newtonian swimming speed, U_{NN}/U_N, as a function of the Deborah number, De, for four different values of the Sperm numbers ($\beta = 0.1$ corresponding to a critical value of Sp $\gtrsim 1.16$ for enhanced swimming, Eq. (4.26)).

leading-order dynamic response of the sheet amplitude and obtain

$$a_{NN}^{(n)} = \frac{-k^2 f^{(n)}}{-\kappa n^2 k^4 + 2\eta\omega i k \left(\dfrac{1 - in\mathrm{De}\beta}{1 - in\mathrm{De}}\right)}. \tag{4.13}$$

As can be seen in Eq. (4.13), the value of the Deborah number impacts the sheet amplitude, and thus the swimmer waveform is modified by a change in the surrounding fluid.

Inputting the linear waveform amplitude, Eq. (4.13), into the quadratic swimming speed, Eq. (4.3), we finally obtain the non-Newtonian swimming speed as

$$U_{NN} = \frac{\omega}{2k} \sum_{n=1}^{\infty} \left[\frac{n^2 |f^{(n)}|^2}{\kappa^2 k^2} \left(\frac{1 + n^2 \beta \mathrm{De}^2}{1 + n^2 \mathrm{De}^2} \right) \frac{1}{n^4 + 4\mathrm{Sp}^6 \left(\frac{1 + n^2\beta^2\mathrm{De}^2}{1 + n^2\mathrm{De}^2} \right) + 4n^3 \mathrm{Sp}^3 \left(\frac{\mathrm{De}(1-\beta)}{1+n^2\mathrm{De}^2} \right)} \right], \tag{4.14}$$

where we have defined the (two-dimensional) Sperm number, $\mathrm{Sp} = (\eta\omega/\kappa k^3)^{1/3}$, which quantifies the dimensionless ratio of fluid to bending stresses [168]. If $\mathrm{Sp} \ll 1$, the dominant balance is between activity and elasticity, and the flagellum waveform is not affected by fluid stresses – this is the stiff (s) limit. In contrast, when $\mathrm{Sp} \gg 1$, fluid effects balance the active bending and the waveform changes with the properties of the fluid – this is the floppy (f) limit.

Simplifying the analysis to focus on the single $n = 1$ mode (reducing notation to $f^{(n)} \equiv f$), we have non-Newtonian swimming at speed

$$U_{NN} = \frac{\omega}{k}\left(\frac{|f|^2}{2\kappa^2 k^2}\right)\frac{\left(1+\beta\mathrm{De}^2\right)}{1+\mathrm{De}^2+4\mathrm{Sp}^3\mathrm{De}(1-\beta)+4\mathrm{Sp}^6\left(1+\beta^2\mathrm{De}^2\right)}, \tag{4.15}$$

while the Newtonian limit is found by setting $\mathrm{De} = 0$ in Eq. (4.15). The non-Newtonian to Newtonian swimming speed ratio, U_{NN}/U_N, is thus given by

$$\frac{U_{NN}}{U_N} = \frac{(1+4\mathrm{Sp}^6)(1+\beta\mathrm{De}^2)}{1+\mathrm{De}^2+4\mathrm{Sp}^3\mathrm{De}(1-\beta)+4\mathrm{Sp}^6(1+\beta^2\mathrm{De}^2)}, \tag{4.16}$$

which is the main result of this Chapter, shown in Fig. 4.1. We note that Eq. (4.16) is monotonically increasing in Sp for fixed De, but is non-monotonic in De for fixed Sp.

4.5 Extension to an infinite filament

Having studied a two-dimensional waving sheet, we outline how to carry out the calculation a three-dimensional infinite filament, following Ref. [176]. Consider an infinite periodic filament in an Oldroyd-B fluid waving with small amplitude. The filament is modelled geometrically as a cylinder, which when straight is parametrised by s along its axis, ϕ around this axis, and radius b. When small-amplitude waves propagate along $\hat{\mathbf{x}}$, the surface of the cylinder is described by $\vec{r}_c = s\hat{\mathbf{x}} + [h(s,t) + b\cos\phi]\hat{\mathbf{y}} + b\sin\phi\hat{\mathbf{z}}$ and the height of the filament away from its centreline position is

$$h(s,t) = \epsilon\mathrm{Re}\left[a_{NN}e^{i(ks-\omega t)}\right], \tag{4.17}$$

where a is the amplitude, and $h(s,t)$ is analogous to $y(x,t)$ in Eq. (4.2) when $n = 1$. Using the first-order Oldroyd-B equation, in Fourier notation, we recover Eq. (4.7). We can then consider the Stokes equation at first order,

$$\nabla^2\tilde{\mathbf{u}}_1 = \eta\left(\frac{1-i\beta\mathrm{De}}{1-i\mathrm{De}}\right)\nabla\tilde{p}_1, \tag{4.18}$$

where the first order boundary conditions for each mode are given by $\tilde{\mathbf{u}}_1 = i\omega\tilde{h}\hat{\mathbf{y}}$. The solutions are best derived using cylindrical polar co-ordinates, where the basis vectors are $\hat{\mathbf{x}}$, $\hat{\mathbf{r}} = \sin\phi\hat{\mathbf{z}} + \cos\phi\hat{\mathbf{y}}$ and $\hat{\theta} = -\sin\phi\hat{\mathbf{y}} + \cos\phi\hat{\mathbf{z}}$. The first-order solutions are shown in Table 4.1 [52]. These can then be used to compute the second-order

$\tilde{p}$	$-\eta\omega k\tilde{h}i\cos\theta AK_1(kr)$
$\tilde{u}_r$	$-\tilde{h}\omega i\cos\theta[\alpha Ark K_1(kr)+BK_2(kr)+CK_0(kr)]$
$\tilde{u}_\theta$	$-\tilde{h}\omega i\sin\theta[BK_2(kr)-CK_0(kr)]$
$\tilde{u}_x$	$-\tilde{h}\omega\cos\theta[\alpha Ark K_0(kr)+(B+C-\alpha A)K_1(kr)]$
αA	$\left\{K_0(kb)+bkK_1(kb)\left[\frac{1}{2}+\frac{K_0(kb)}{2K_2(kb)}-\frac{K_0(kb)^2}{K_1(kb)^2}\right]\right\}^{-1}$
B	$-\alpha Abk K_1(kb)/[2K_2(kb)]$
C	$[1-bkK_1(kb)\alpha A/2]/K_0(kb)$

Table 4.1 Pressure and velocity field for a travelling wave in the $\hat{\mathbf{x}}$ direction on a cylinder to first-order in $\ln(kb)$, with $\alpha=(1-i\mathrm{De})/(1-i\beta\mathrm{De})$ [52].

swimming speed, leading to the same result as Eq. (4.3). The force per unit length acting of the fluid is found by integrating the stress around the circumference and keeping only lowest-order terms in $\ln(kb)$ the force per unit length perpendicular to the filament is

$$\mathcal{F}_{vis}=\mathrm{Re}\left[-i\omega a_{NN}\frac{4\pi}{\ln(kb)}\frac{1-i\beta\mathrm{De}}{1-i\mathrm{De}}\eta e^{i(ks-\omega t)}\right]. \tag{4.19}$$

This viscoelastic force is then balanced by the passive elastic forces of the filament and the internal forcing,

$$\tilde{\mathcal{F}}_{vis}=-2b\frac{\partial^2\tilde{F}_1}{\partial s^2}-\kappa\frac{\partial^4\tilde{h}}{\partial s^4}\,, \tag{4.20}$$

where F_1 is the first-order bending moment per unit length, as above. The non-Newtonian swimming velocity is then finally given by

$$U_{NN}=\frac{\omega}{k}\left(\frac{2b^2\left|f\right|^2}{\kappa^2k^2}\right)\frac{\left(1+\beta\mathrm{De}^2\right)}{1+\mathrm{De}^2+2\mathrm{Sp}^4\mathrm{De}(1-\beta)+\mathrm{Sp}^8\left(1+\beta^2\mathrm{De}^2\right)}, \tag{4.21}$$

where we have defined the perpendicular drag coefficient $c_\perp=4\pi\eta/\ln(kb)$, and the three-dimensional Sperm number, $\mathrm{Sp}=(c_\perp\omega/\kappa k^4)^{1/4}$. Comparing Eq. (4.21) and Eq. (4.15) we see that they have a similar dependence on the Deborah number and β, with slight differences in coefficients for each of the terms. The main differences arise from the difference between the two-dimensional and three-dimensional Sperm number, however studying the limits of the two functions we recover the same results, as shown in Table 4.2. The three dimensional result, Eq. (4.21), is thus very similar to the two-dimensional case Eq. (4.15), and the physical mechanism identified in this Chapter extends naturally to three dimensions.

	two-dimensional U_{NN}/U_N	three-dimensional U_{NN}/U_N
$\mathrm{Sp} \to 0$	$\frac{1+\beta \mathrm{De}^2}{1+\mathrm{De}^2}$	$\frac{1+\beta \mathrm{De}^2}{1+\mathrm{De}^2}$
$\mathrm{De} \to 0$	1	1
$\mathrm{Sp} \to \infty$	$\frac{1+\beta \mathrm{De}^2}{1+\beta^2 \mathrm{De}^2}$	$\frac{1+\beta \mathrm{De}^2}{1+\beta^2 \mathrm{De}^2}$
$\mathrm{De} \to \infty$	$\frac{\beta+4\beta \mathrm{Sp}^6}{1+4\beta^2 \mathrm{Sp}^6}$	$\frac{\beta+\beta \mathrm{Sp}^8}{1+\beta^2 \mathrm{Sp}^8}$
$\mathrm{Sp} \to \infty$ and $\mathrm{De} \to \infty$	$1/\beta$	$1/\beta$
$\mathrm{Sp} \to 0$ and $\mathrm{De} \to 0$	1	1

Table 4.2 The limits of the two-dimensional swimming speed ratio are compared to the limits of the three dimensional swimming speed ratio.

4.6 Enhanced locomotion

In order to derive the conditions under which swimming enhancement is possible, we need to understand when the swimming speed ratio U_{NN}/U_N as a function of $(\beta, \mathrm{De}, \mathrm{Sp})$ can be above one. Let us first consider some relevant physical limits. In the stiff limit, $\mathrm{Sp} \ll 1$, Eq. (4.16) simplifies to the fixed-amplitude result [44]

$$\frac{U_{NN}}{U_N} = \frac{1 + \beta \mathrm{De}^2}{1 + \mathrm{De}^2}. \tag{4.22}$$

In that limit, the swimming speed ratio decreases monotonically with increasing Deborah number to the asymptotic value $U_{NN} = (\eta_s/\eta)U_N$ for $\mathrm{De} \gg 1$.

In the opposite floppy limit, $\mathrm{Sp} \gg 1$, the flagellum shape is highly sensitive to changes in the hydrodynamic stress and the speed ratio, Eq. (4.16), reduces to

$$\frac{U_{NN}}{U_N} = \frac{1 + \beta \mathrm{De}^2}{1 + \beta^2 \mathrm{De}^2}. \tag{4.23}$$

Here, we obtain a systematic monotonic increase of the swimming speed with Deborah numbers, up to an asymptotic value $U_{NN}/U_N = 1/\beta$ obtained when $\mathrm{De} \gg 1$. This is the maximum value of the swimming speed ratio that can be achieved.

Our model points therefore to a transition from hindered to enhanced swimming when the flagellum is sufficiently flexible. To get further insight, let us look at small deviations from the Newtonian limit ($\mathrm{De} = 0$). Computing the derivate of U_{NN}/U_N with respect to De we get

$$\frac{\partial}{\partial \mathrm{De}} \left(\frac{U_{NN}}{U_N} \right) \Big|_{\mathrm{De}=0} = \frac{4(\beta - 1)\mathrm{Sp}^3}{(1 + 4\mathrm{Sp}^6)}, \tag{4.24}$$

which is always negative. Consequently, a small amount of viscoelasticity (De $\ll 1$) will always start by decreasing the swimming speed. In contrast, in the infinite Deborah number limit, the swimming speed ratio becomes

$$\frac{U_{NN}}{U_N}(\mathrm{De} \gg 1) = \frac{\beta + 4\beta \mathrm{Sp}^6}{1 + 4\beta^2 \mathrm{Sp}^6}. \tag{4.25}$$

A transition from hindered ($U_{NN} < U_N$) to enhanced propulsion ($U_{NN} > U_N$) in a non-Newtonian fluid occurs thus when

$$\mathrm{Sp}^3 > \frac{1}{2\sqrt{\beta}}. \tag{4.26}$$

The result in Eq. (4.26) indicates therefore a transition in swimmer flexibility allowing enhancement of the swimming speed. Indeed, the Sperm number scales inversely proportional to the flagellum bending modulus, and thus for a given fluid, the criterion in Eq. (4.26) is equivalent to a requirement for κ to be small enough.

Our results are illustrated numerically in Fig. 4.1 for $\beta = 0.1$. We plot the ratio of the non-Newtonian to Newtonian swimmer speed, U_{NN}/U_N, as a function of the Deborah number for four different values of the Sperm number. The data are shown in Fig. 4.1a for small values of De and ranging from 0 to 100 in Fig. 4.1b. In all cases, the swimming speed initially decreases with the Deborah number (Fig. 4.1a) but when the swimmer is sufficiently flexible, the swimming speed subsequently increases and crosses the threshold $U_{NN} = U_N$ (Fig. 4.1b). The criterion from Eq. (4.26) corresponds to enhancement predicted to occur as soon as $\mathrm{Sp} \gtrsim 1.16$, consistent with the numerical results. Note that our model also allows us to compute the value of the transition Deborah number beyond which enhancement occurs. In Eq. (4.16), one can solve the quadratic equation for De and $U_{NN} > U_N$ is equivalent to $\mathrm{De} > 4\mathrm{Sp}^3/(4\beta\mathrm{Sp}^6 - 1)$, which, as expected, is defined only if the criterion in Eq. (4.26) is satisfied.

Beyond swimming kinematics, our model also allows us to compute swimming energetics and efficiency. Following Ref. [44] and the derivations above, we can calculate the power expanded by the swimmer against the fluid, W_{NN}. Defining the swimming efficiency, classically, as $\mathcal{E} = \eta U^2/W$, the ratio between the non-Newtonian efficiency and that in a Newtonian fluid with the same viscosity (η) is exactly given by the swimming speed ratio U_{NN}/U_N from Eq. (4.16), *i.e.*

$$\frac{\mathcal{E}_{NN}}{\mathcal{E}_N} = \frac{U_{NN}}{U_N}. \tag{4.27}$$

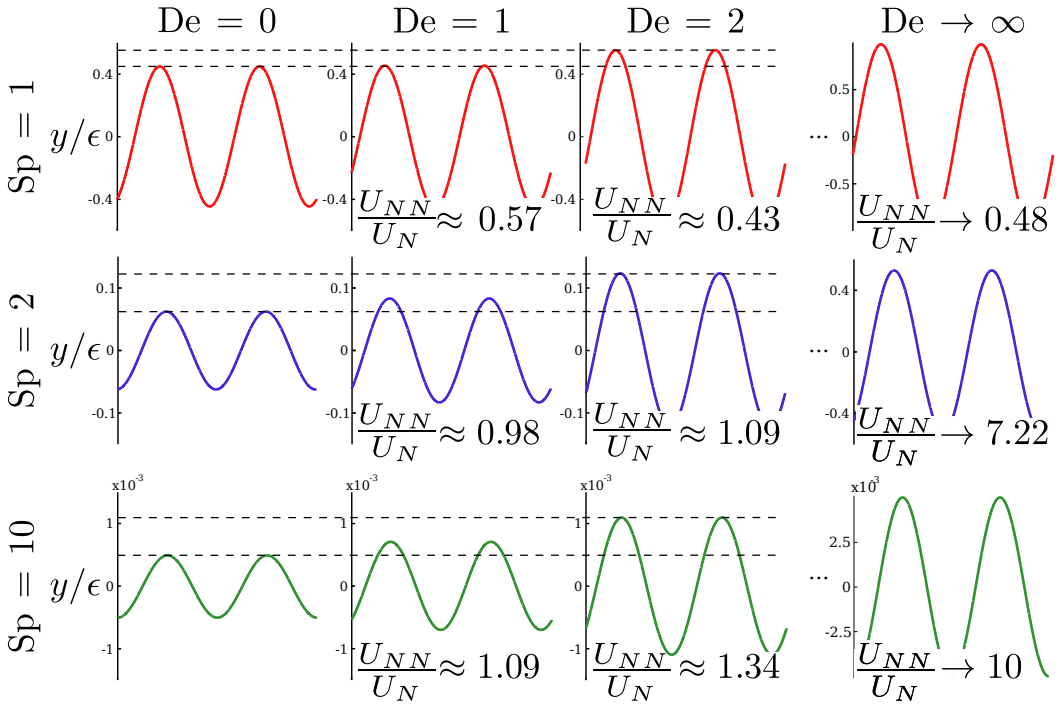

Fig. 4.2 Swimming waveforms under a linear response for Sp = 1, 2, and 10, as a function of the Deborah number, De. In each plot, the value of the swimming ratio, U_{NN}/U_N, is indicated. As in Fig. 4.1 $\beta = 0.1$ and Sp $\gtrsim 1.16$ is required for enhancement. An increase in De leads to an increase in waving amplitude which, when sufficiently large, leads to enhanced swimming.

Thus conditions for enhanced swimming correspond thus to those required for enhanced efficiency and we cannot have increased speed without increased efficiency or increased efficiency without increased speed.

4.7 Illustration of the waveform

We further illustrate the impact of non-Newtonian stresses by displaying the swimming waveform in the case of an internal sinusoidal forcing. We thus prescribe $f^{(1)} = f$ and $f^{(n)} = 0$ for $n > 1$, and compute the leading-order waveform. Under the assumption of linear response, the shape remains sinusoidal with a different phase and amplitude. The waveforms of one wavelength are illustrated in Fig. 4.2 for three Sperm numbers (1, 2 and 10) and four Deborah numbers (0, 1, 2, and ∞). Superimposed on the shapes are the values of U_{NN}/U_N.

The results in Fig. 4.2 show the expected decrease in waving amplitude that accompanies an increase in Sperm number but, more importantly, the systematic

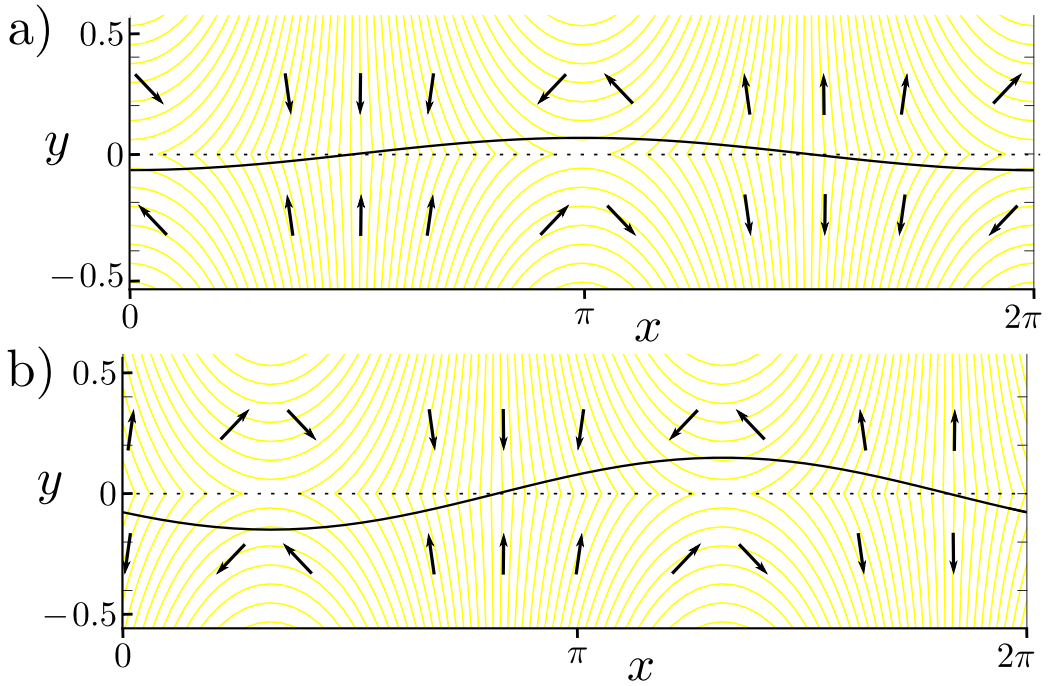

Fig. 4.3 The first order stream function is shown in yellow for an planar wave swimmer immersed in (a) a Newtonian fluid, and (b) a non-Newtonian fluid (De = 2). Both swimmers have Sp = 2 and show their respective waveforms with the first order velocity field in black arrows.

increase in amplitude with an increase of viscoelasticity De. The waving amplitudes can be computed analytically and we obtain the Newtonian result as $a_N^2 = 1/(1 + 4\mathrm{Sp}^6)$, which explains the decrease of waving amplitude with Sperm number. In the non-Newtonian case we have a waving amplitude given by

$$a_{NN}^2 = \frac{1 + \mathrm{De}^2}{1 + \mathrm{De}^2 + 4\mathrm{Sp}^3\mathrm{De}(1-\beta) + 4\mathrm{Sp}^6(1 + \beta^2\mathrm{De}^2)}. \tag{4.28}$$

The critical Deborah number for which $a_{NN} > a_N$ is then found to be $\mathrm{De} > 1/\mathrm{Sp}^3(1+\beta)$, which is always satisfied. Hence the presence of viscoelastic stresses leads to a systematic increase of the waving amplitude of the swimmer. This provides a physical interpretation for the swimming enhancement seen in Fig. 4.1: if the viscoelastic amplitude increase is large enough, it is able to compensate for the non-Newtonian damping term from Eq. (4.3), leading to faster swimming, $U_{NN} > U_N$.

Furthermore we plot the first order stream function at a fixed time $t = 0$ in Fig. 4.3. Here we again see the increase in amplitude moving from a Newtonian to a non-Newtonian fluid, and the phase shift between them. Additionally we see that

at first order both swimmers have the same streamlines (shifted). We note that the regions of extension and compression in the Newtonian fluid are dissipative, but in the viscoelastic fluid some of the work done on the fluid is stored in the polymer springs. Thus the work done on a viscoelastic fluid is always reduced compared to a Newtonian fluid allowing for an increased amplitude to be achieved.

4.8 Discussion

In this Chapter, we have proposed a physical mechanism for enhanced locomotion in a viscoelastic fluid. It does not require transient or end effects but instead arises naturally due to the equations of active elasto-hydrodynamics applied to locomotion.

Our results can be rationalised by focusing on the two different stiff (s) and floppy (f) limits, and comparing the non-Newtonian swimming speed for $\mathrm{De} \gg 1$ to the Newtonian one ($\mathrm{De} = 0$). In the stiff regime fluid forces are negligible, and the dynamic balance in Eq. (4.12) reduces to one between bending resistance and active stresses. Considering only the typical magnitudes of a and f, we then get $a^{(s)} \sim f/\kappa k^2$ for both Newtonian and non-Newtonian. The swimming speeds scale then as $U_N^{(s)} \sim \omega f^2/\kappa^2 k^3$ and, for large De, $U_{NN}^{(s)} \sim \beta\omega f^2/\kappa^2 k^3$, leading to $\left(\frac{U_{NN}}{U_N}\right)^{(s)} = \beta < 1$. In contrast, in the floppy regime, elastic forces are negligible compared to fluid stresses, and the dynamic balance in Eq. (4.12) reduces to one between the fluid resistance of the filament and the active stresses, with $a_N^{(f)} \sim kf/\eta\omega$ and $a_{NN}^{(f)} \sim kf/\eta\omega\beta$. The swimming speeds in this case are given by $U_N^{(f)} \sim k^3 f^2/\eta^2\omega$ and $U_{NN}^{(f)} \sim k^3 f^2/\beta\eta^2\omega$, leading to $\left(\frac{U_{NN}}{U_N}\right)^{(f)} = 1/\beta > 1$, and enhanced swimming.

Physically, we have shown that the transition from hindered to enhanced swimming takes its origin in the systematic increase of the waving amplitude for active swimming in a viscoelastic fluid, which can overcome viscoelastic fluid damping [44]. How can this increase in amplitude be intuitively rationalised? We would like to argue that it is a consequence of the change in fluid pressure, and results from a 'viscoelastic suction'. Indeed, we consider the leading-order pressure in Eq. (4.10), and compute its typical value on the sheet for a fixed amplitude a, allowing us to isolate the change in pressure due to the fluid dynamics and not due to the amplitude increase. The ratio between the typical non-Newtonian and Newtonian pressure is then

$$\left[\frac{p_{NN}(a)}{p_N(a)}\right]^2 = \frac{1+\beta^2\mathrm{De}^2}{1+\mathrm{De}^2}, \tag{4.29}$$

which shows a large pressure reduction (since $\beta < 1$) in a viscoelastic fluid. For sufficiently large Sperm numbers, where fluid stresses have a relatively larger impact on the waveform, the wave amplitude increase due to this suction effect is able to overcome the non-Newtonian fluid damping in locomotion and increase the swimming speed.

To conclude, we note that although the mechanism outlined in this Chapter was derived in the context of flagellar locomotion, the same physical principle would be at play for higher swimmers exploiting muscular contractions, and thus could also be relevant to the dynamics of small multicellular organisms in complex environments.

5

Tumbling-to-swimming transition in bacteria motion

This chapter contains a mixture of my own work and work that has been done in collaboration with Debasish Das, a post-doc with Eric Lauga. The rod model and the analytic work for modelling helical flagellar filaments is my own work, and the numerics of the helical model were done in collaboration with Debasish Das.

5.1 Introduction

Peritrichously flagellated bacteria have many flagella, typically 4-7 for *E. coli*. Each flagellum consists of a helical flagellar filament, a short elastic hook, and a rotary motor. Here we study the swimming of peritrichously flagellated bacteria while varying the hook stiffness and show that swimming occurs due to an elasto-hydrodynamic instability. If the flagellar filaments are somewhat randomly distributed on the cell body and they are all roughly similar, why don't the flagella all push against each other leading to negligible swimming? The flexibility of the hook is crucial for the gathering of flagella at one end of the cell leading to successful swimming. If the hook was rigid the filaments would all be normal to the cell body surface at all times and hence never bundle, however *in vivo* the hook is flexible leading to successful swimming.

We first build a simple model of a cell propelled by two active rods, capturing the instability and finding analytically a critical hook stiffness below which swimming occurs. We then build a numerical model of swimming bacteria using slender-body theory, but ignore interactions between flagella explored by previous studies. We observe a transition from negligible swimming to successful swimming with decreasing

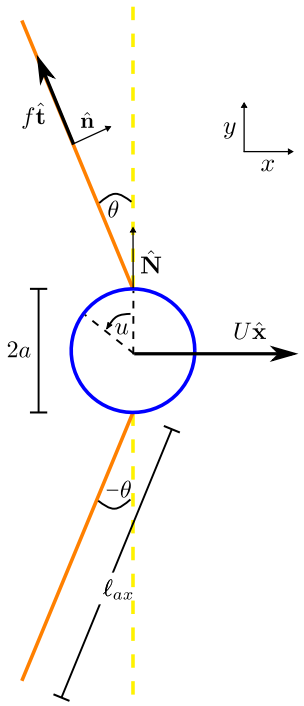

Fig. 5.1 Simple model: Two rods are attached at $u_1 = 0$ (top) and $u_2 = \pi$ (bottom), to a spherical head of radius a. Rods are length ℓ_{ax}, have a tilt angle $\pm\theta$ away from the cell body surface normal, $\hat{\mathbf{N}}$. Each rod pushes with a force of size f along its tangent vector $\hat{\mathbf{t}}$, and as a result swims with velocity $U\hat{\mathbf{x}}$.

hook stiffness. Finally, we examine past measurements of hook flexibility and show bacteria are safely on the swimming side of the instability.

5.2 Rod model of peritrichous bacterium

To propose a first model for a symmetric bacterium, we attach two flagella, one on each side of a spherical body shown in Fig. 5.1. The helical flagellar filaments are approximated as straight rods of length ℓ_{ax}. Instead of force generation coming from rotating a helix, we impose a force per unit length tangent to the rod. The rods are of equal length, with their bases positioned at $u_1 = 0$ (top) and $u_2 = \pi$ (bottom) around the cell body. The rod filaments are attached to the cell body via a short elastic filament, the bacteria hook. The hook is less than 100× shorter than the flagellar filament, thus we can ignore the hydrodynamics of the hook as in Ref. [81]. To capture the elastic torque it imposes on the flagellar filament (and hence the cell body) we treat the elastic filament as a springed hinge with spring constant $K = EI/\ell_h$, where EI is the bending rigidity of the hook, and ℓ_h is the length of the hook, as in Ref. [82].

Table 5.1 Typical wild type *E. coli* parameters

Parameter	Symbol	Value	Dimensionless	
Cell Body (Major Axis Radius)	c	1.3 μm	1	[177]
Cell Body (Minor Axis Radius)	a	0.4 μm	0.3	[177]
Number of Flagella	N_f	4-7	-	[178]
Helix Rotation Frequency	ν	110 Hz	1	[72]
Helix Radius	R_h	0.2 μm	0.15	[72]
Helix Wavelength	λ	2.2 μm	1.7	[72]
Helix Pitch Angle	β	$-30°$	-	$\tan^{-1}\beta = 2\pi R_h/\lambda$
Helix Axis Length	ℓ_{ax}	6.1 μm	4.7	[72]
Helix Filament Radius	r_f	12 nm	0.01	[72]
Bacteria Hook Length	ℓ_h	55 nm	0.04	[72]
Number of Turns	n	2.8	-	ℓ_{ax}/λ

The force exerted by the rods is $f\hat{\mathbf{t}}_{1,2}$, where

$$\hat{\mathbf{t}}_{1,2} = -\sin(u_{1,2}+\theta_{1,2})\hat{\mathbf{x}} + \cos(u_{1,2}+\theta_{1,2})\hat{\mathbf{y}}, \tag{5.1}$$

and f the force per unit length (along the flagellar filament axis) for a helical swimmer is given by resistive force theory as [27]

$$f = c_\perp \omega R_h \sin\beta \left(1 - \frac{c_\parallel}{c_\perp}\right). \tag{5.2}$$

Here $c_\parallel$ and $c_\perp$ the drag coefficients of a cylindrical rod moving parallel and perpendicular respectively, R_h the helix radius, $\omega = 2\pi\nu$ the angular velocity and β the helix pitch angle, with typical *E. coli* flagellar filament given in Table 5.1. The sign of f determines whether the swimmer is a pusher or a puller. If f is negative then the swimmer then the forces point towards the cell body and the swimmer is a pusher conversely if f is positive then the forces point away from the cell body and the swimmer is a puller. There are three different ways to change the sign of f. Firstly change the rotation direction of the flagella where $\omega > 0$ for counter-clockwise motion looking from the end of the flagellum to the cell body, and $\omega < 0$ for clockwise motion. Secondly the handedness of the helical filament can be changed from left ("normal") to right handed such that $\sin\beta$ changes from negative to positive. Finally lateral hairs can be placed on the flagellum such that $c_\parallel > c_\perp$, but there are no known examples of flagellated bacteria that have this feature. As bacteria flagella have a well conserved rod-like shape $c_\perp > c_\parallel$. For a given swimmer type (pusher or puller) when $\theta_{1,2} = 0$

there is no motion as the top and bottom forces are equal and opposite (dashed lines in Fig. 5.1).

For swimming a perturbation is required, we tilt both rods by an angle θ away from their original position, but in opposite directions. By symmetry there is only motion in the $\hat{\mathbf{x}}$ direction and there is no angular velocity. Under low Reynolds conditions the force on the entire cell must sum to zero such that there is zero net force. If we consider the forces exerted on the cell by the fluid

$$\hat{\mathbf{x}} \cdot \Bigg[- U\ell_{ax}\hat{\mathbf{x}} \cdot \Big(c_{\parallel} \left(\hat{\mathbf{t}}_1\hat{\mathbf{t}}_1 + \hat{\mathbf{t}}_2\hat{\mathbf{t}}_2 \right) + c_{\perp} \left(\hat{\mathbf{n}}_1\hat{\mathbf{n}}_1 + \hat{\mathbf{n}}_2\hat{\mathbf{n}}_2 \right) \Big) + 6\pi\mu a\hat{\mathbf{x}} + f\ell_{ax} \left(\hat{\mathbf{t}}_1 + \hat{\mathbf{t}}_2 \right) + \frac{\ell_{ax}^2}{2} \left(\dot{\theta}_1\hat{\mathbf{n}}_1 + \dot{\theta}_2\hat{\mathbf{n}}_2 \right) \Bigg] = 0, \tag{5.3}$$

where

$$\hat{\mathbf{n}}_{1,2} = \cos(u_{1,2} + \theta_{1,2})\hat{\mathbf{x}} - \sin(u_{1,2} + \theta_{1,2})\hat{\mathbf{y}}, \tag{5.4}$$

is the unit normal to the rod, U is the swimming speed, and $\dot{\theta}_{1,2}$ is the rate of change of $\theta_{1,2}$, where $\dot{\theta}_1 = -\dot{\theta}_2$.

Using Eqs. 5.1, 5.4, and $\theta_1 = -\theta_2$, we can simplify the force balance to

$$- 2\ell_{ax}U \left(c_{\parallel} \cos^2\theta + c_{\perp} \sin^2\theta \right) - 6\pi\mu aU + 2f\ell_{ax} \sin\theta + \dot{\theta}\ell_{ax}^2 c_{\perp} \cos\theta = 0, \tag{5.5}$$

where $\theta = |\theta_1| = |\theta_2|$. Rearranging for the swimming speed,

$$U = \frac{2f\ell_{ax} \sin\theta + \dot{\theta}\ell_{ax}^2 c_{\perp} \cos\theta}{6\pi\mu a + 2\ell_{ax}(c_{\parallel} \sin^2\theta + c_{\perp} \cos^2\theta)}. \tag{5.6}$$

Secondly, we consider the motion of the rod flagella relative to the cell body. The rod flagella is attached to the cell body but is free to rotate about its attachment point at the cell surface. We can consider each rod individually as the rods only interact through the background flow field $-U\hat{\mathbf{x}}$.

Firstly we have the torque on the rod due to the fluid, of which there are two components: one due to the background flow,

$$\vec{\boldsymbol{L}}_{back} = \frac{\ell_{ax}^2}{2} U c_{\perp} \left(\hat{\mathbf{x}} \cdot \hat{\mathbf{n}}_{1,2} \right) \hat{\mathbf{t}}_{1,2} \times \hat{\mathbf{n}}_{1,2}; \tag{5.7}$$

and a second torque due to the rotation of the filament,

$$\vec{\boldsymbol{L}}_{\dot{\theta}} = -\frac{\ell_{ax}}{3}\dot{\theta}_{1,2}\hat{\mathbf{n}}_{1,2} \cdot \left(\hat{\mathbf{t}}_{1,2} \times \hat{\dot{\theta}}_{1,2}\right)\left(\hat{\mathbf{t}}_{1,2} \times \hat{\mathbf{n}}_{1,2}\right). \tag{5.8}$$

The motion of the rod is constrained to the $\hat{\mathbf{x}} - \hat{\mathbf{y}}$ plane, thus $\hat{\dot{\theta}}_{1,2} = \hat{\mathbf{b}}$, where $\hat{\mathbf{b}} = \hat{\mathbf{t}}_{1,2} \times \hat{\mathbf{n}}_{1,2}$. The sign of $\dot{\theta}_{1,2}$ determines if the rod rotation is clockwise or anti-clockwise. The final torque on the rod is the elastic torque on the rod due to the springed hinge connecting the rod to the cell body, given by

$$\vec{\boldsymbol{L}}_{elas} = K\theta_{1,2}\frac{(\hat{\mathbf{t}}_{1,2} \times \hat{\mathbf{N}}_{1,2})}{|\hat{\mathbf{t}}_{1,2} \times \hat{\mathbf{N}}_{1,2}|}, \tag{5.9}$$

where

$$\hat{\mathbf{N}}_{1,2} = \sin u_{1,2}\hat{\mathbf{x}} + \cos u_{1,2}\hat{\mathbf{y}}, \tag{5.10}$$

is the unit normal to the cell body surface at the point of attachment. The final low Reynolds moment balance for each rod is given by

$$\vec{\boldsymbol{L}}_{back} + \vec{\boldsymbol{L}}_{\dot{\theta}} + \vec{\boldsymbol{L}}_{elas} = 0. \tag{5.11}$$

Since each flagellum is identical (up to a sign change), and $\hat{\mathbf{t}}_{1,2} \times \hat{\mathbf{N}}_{1,2} = -\hat{\mathbf{b}}$ the moment balance for each flagellum simplifies to

$$-\frac{\ell_{ax}^3}{3}c_\perp\dot{\theta} + \frac{\ell_{ax}^2}{2}Uc_\perp\cos\theta - K\theta = 0, \tag{5.12}$$

in the $\hat{\mathbf{b}}$ direction. Together with Eq. (5.6), we now have an equation for the evolution of θ

$$\left(\frac{\ell_{ax}^3}{3}c_\perp + \frac{c_\perp^2\cos^2\theta\ell_{ax}^2}{12\pi\mu a + 4\ell_{ax}(c_\parallel\sin^2\theta + c_\perp\cos^2\theta)}\right)\dot{\theta} = \frac{-f\ell_{ax}^3\sin\theta\cos\theta c_\perp}{6\pi\mu a + 2\ell_{ax}(c_\parallel\sin^2\theta + c_\perp\cos^2\theta)} - K\theta. \tag{5.13}$$

As

$$\frac{\ell_{ax}^3}{3}c_\perp + \frac{c_\perp^2\cos^2\theta\ell_{ax}^2}{12\pi\mu a + 4\ell_{ax}(c_\parallel\sin^2\theta + c_\perp\cos^2\theta)} \neq 0 \tag{5.14}$$

for all values of θ given that the rest of the parameters $(c_\perp, c_\parallel, \ell_{ax}, a, \mu)$ are positive, we need only look to the right hand side of Eq. (5.13) for steady state values. When the elastic torque dominates ($K \to \infty$), $\theta = 0$ is the only steady state, conversely

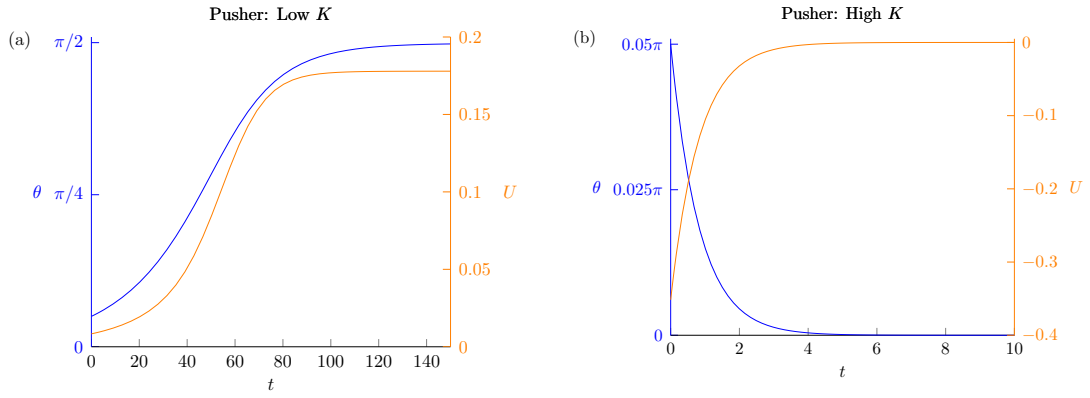

Fig. 5.2 Both graphs show the tilt angle θ and speed U for a pusher swimmer with an initial perturbation of $\theta|_{t=0} = 0.05\pi$. We show a low and a high spring constant: (a) with $K = 0.01$; and (b) with $K = 100$. The pusher swimmer with a low spring constant is able to swim.

if the elastic torque is negligible ($K = 0$), there are multiple steady states either $\theta = [0, \pi/2, \pi]$.

Firstly we solve Eq. (5.13) numerically, (using inbuilt MATLAB function, ode45), with the appropriate flagellar filament values for a wild type *E. coli* (shown in Table 5.1). We non-dimensionalise lengths by the maximum body size c, time t by the frequency of flagella rotation $\nu = \omega/2\pi$, and viscosity by the viscosity of water $\eta_{water} = 8.9\times10^{-4}$ Pa·s which our swimmers are immersed in. For each setup we start with a small perturbation, which is positive for the top rod and negative for the bottom rod. Both flagella have the same absolute values of θ, but have the opposite sign so they rods rotate in opposite senses at their base, as a mirror image. The evolution of θ in time is found for pusher (Fig. 5.2) and pullers (Fig. 5.3) with low and high K values. We see that for a pusher with a low spring constant, the cell swims, whereas for a puller with the same low spring constant no swimming occurs. At high spring constant, neither a pusher or a puller swim. A steady state is reached for all the different swimmers, so to explore the transition from no swimming to swimming we find steady state values for a range of K values. As shown in Fig. 5.4, at low K the rods are tilted, whereas at high K there is no tilt, hence no swimming. As K increases from this low K limit there is a smooth transition from $\theta = \pi/2$ to $\theta = 0$. There is a critical K above which the cell does not swim. The swimmer reaches its maximum velocity when the rod flagella are parallel to one another such that their forces point in the same direction.

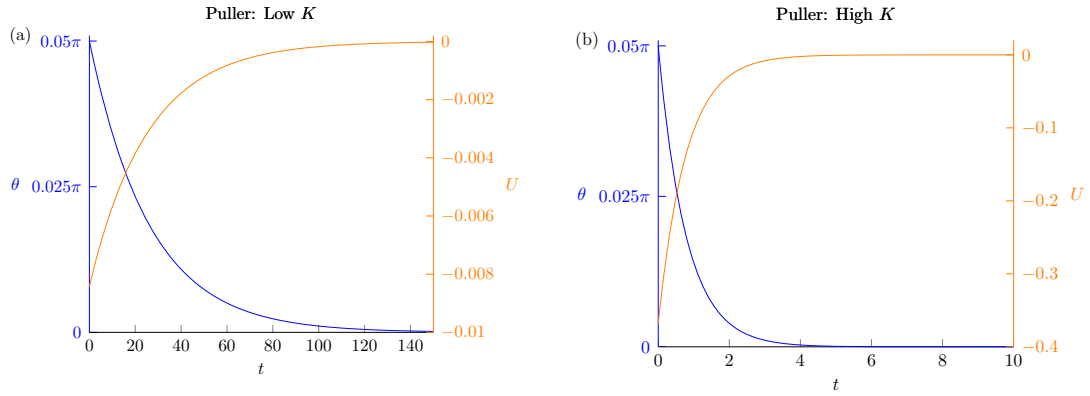

Fig. 5.3 Both graphs show the tilt angle θ and speed U for a puller swimmer with an initial perturbation of $\theta|_{t=0} = 0.05\pi$. We show a low and a high spring constant: (a) with $K = 0.01$; and (b) with $K = 100$, neither of which swim.

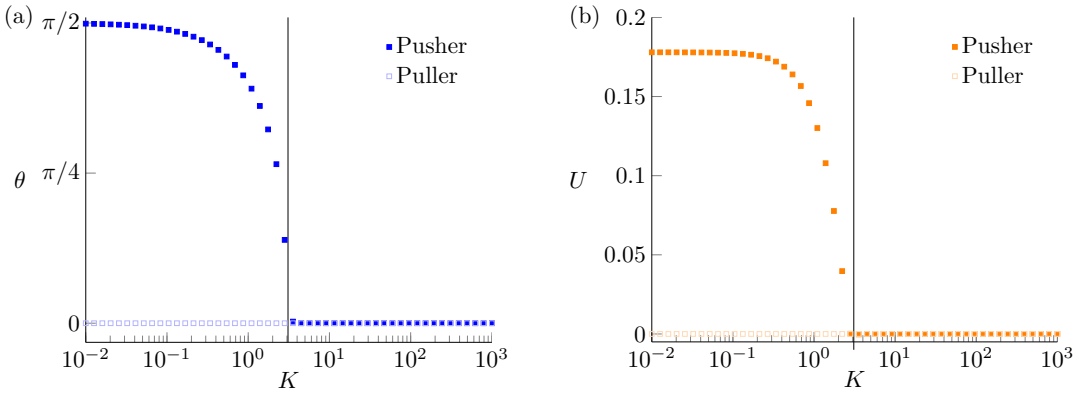

Fig. 5.4 The steady state tilt angles θ and swimming speeds U are found for a range of K values. With a pusher (filled symbols) we see a smooth transition from $\theta = \pi/2$ to $\theta = 0$, for a puller (open symbols) there is no transition. The black line is $K_c = 3.1$ found from linear stability analysis.

In order to analytically determine the stability of the $\theta = 0$ steady state, which exists for all K, we expand Eq. (5.13) about $\theta = 0$, such that

$$\dot{\theta} \approx \frac{3\theta}{c_\perp \ell_{ax}^3} \left(-K - \frac{f c_\perp \ell_{ax}^3}{2c_\perp \ell_{ax} + 6\pi\mu a} \right). \tag{5.15}$$

If f is positive (*i.e.* the swimmer is a puller) then the system is alway stable to small θ perturbations for any K value. Conversely if we study a pusher swimmer where f is negative, we can define a critical hook spring constant

$$K_c = -\frac{f c_\perp \ell_{ax}^3}{2c_\perp \ell_{ax} + 6\pi\mu a}, \tag{5.16}$$

below which the system is unstable and swimming occurs. If the hook is flexible enough then a small perturbation leads to swimming, and increasing U. Through flow induced bending at the hook the perturbation grows, generating more thrust and hence the perturbation is amplified. In Fig. 5.4 we see the analytically found critical hook stiffness matches the full solution.

To explore this instability with more realistic modelling we create a numerical model using helical flagella, where the force generation is due to the rotation of the flagellar filament.

5.3 Bacterium and reference frames

To build our bacterium model, shown in Fig. 5.5, with N_f flagella attached to an ellipsoidal cell body, we start by describing the different components and their frames. There are 4 frames required, the lab frame ($\hat{\mathbf{X}} - \hat{\mathbf{Y}} - \hat{\mathbf{Z}}$), the cell body frame ($\hat{\mathbf{x}} - \hat{\mathbf{y}} - \hat{\mathbf{z}}$), the cell body surface frame ($\hat{\mathbf{T}}^{(1)} - \hat{\mathbf{T}}^{(2)} - \hat{\mathbf{N}}$) and the flagellar filament frame ($\hat{\mathbf{i}} - \hat{\mathbf{j}} - \hat{\mathbf{k}}$).

The cell body is a prolate ellipse, with its long axis orientated in the $\hat{\mathbf{z}}$ direction, the radius in this direction is c, and the radii in the $\hat{\mathbf{x}}$ and $\hat{\mathbf{y}}$ direction is a, where $a < c$ is an ellipsoid as shown in Fig. 5.6. The eccentricity of the ellipsoid is then described by

$$e = \frac{\sqrt{c^2 - a^2}}{c}. \tag{5.17}$$

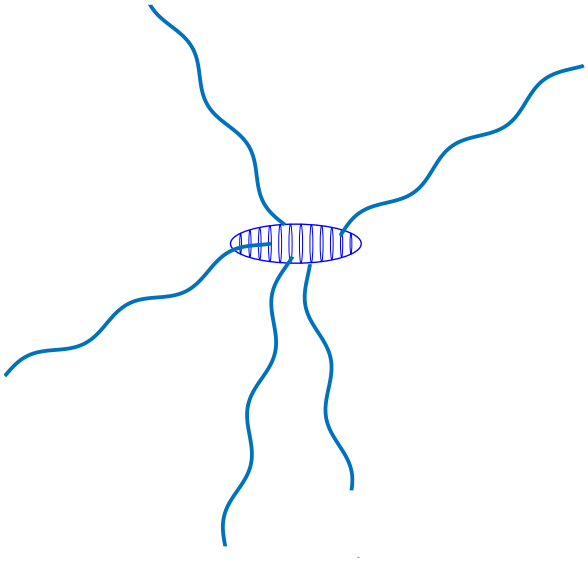

Fig. 5.5 A bacterium with five flagella.

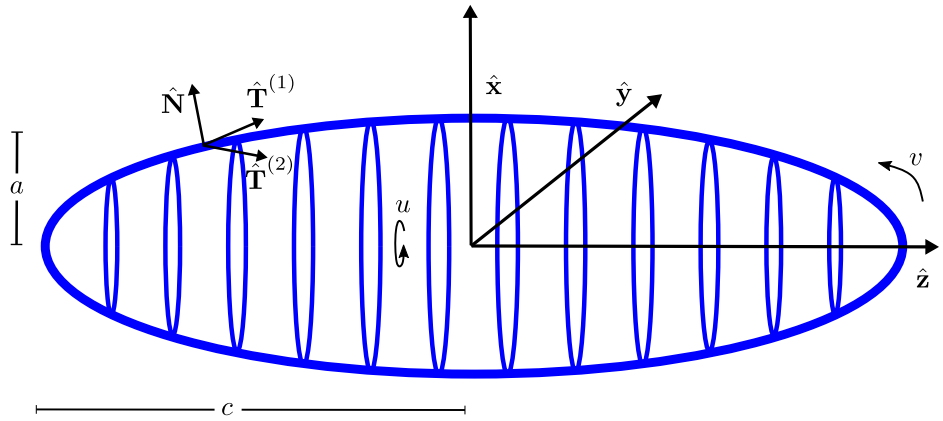

Fig. 5.6 The bacterium body is shown together with the cell body frame and cell body surface frame.

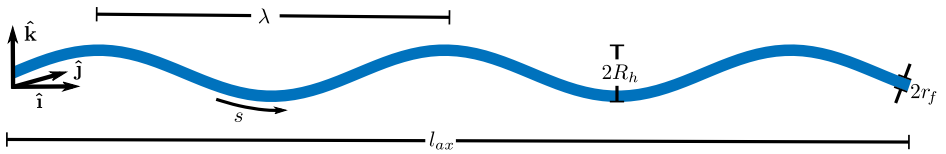

Fig. 5.7 The flagellar filament is shown together with the helix frame and helix parameters.

and in the orthonormal cell-body frame $\hat{\mathbf{x}} - \hat{\mathbf{y}} - \hat{\mathbf{z}}$, the surface is described by

$$x = a \sin v_i \cos u_i, \tag{5.18}$$

$$y = a \sin v_i \sin u_i, \tag{5.19}$$

$$z = c \cos v_i, \tag{5.20}$$

where $u = [0..2\pi)$, $v = [0..\pi]$. The cell body can be any known shape, *i.e.* one which we can describe the surface and the hydrodynamic resistance matrix.

If the bacterium does not rotate then the lab frame $(\hat{\mathbf{X}} - \hat{\mathbf{Y}} - \hat{\mathbf{Z}})$ is the same orientation as the body frame. Otherwise we must rotate vectors in the cell-body frame to the lab frame via the cell body angular velocity, $\vec{\mathbf{\Omega}}_b$. We can describe the rotation of the cell body vector basis as

$$\frac{d\vec{\boldsymbol{x}}}{dt} = \vec{\mathbf{\Omega}}_b \times \vec{\boldsymbol{x}}, \tag{5.21}$$

$$\frac{d\vec{\boldsymbol{y}}}{dt} = \vec{\mathbf{\Omega}}_b \times \vec{\boldsymbol{y}}, \tag{5.22}$$

which must be normalised, such that

$$\hat{\mathbf{x}}' = \frac{\vec{\boldsymbol{x}}}{|\vec{\boldsymbol{x}}|}, \tag{5.23}$$

$$\hat{\mathbf{y}}' = \frac{\vec{\boldsymbol{y}} - \vec{\boldsymbol{y}} \cdot \vec{\boldsymbol{x}}}{|\vec{\boldsymbol{y}}|}; \tag{5.24}$$

hence we can define the final axis as

$$\hat{\mathbf{z}}' = \hat{\mathbf{x}}' \times \hat{\mathbf{y}}', \tag{5.25}$$

where the dashes represent the rotated cell body vectors in the lab frame. We can also define a rotation matrix, $\mathbf{B_b} = \mathbf{C_b}\mathbf{D_b}\mathbf{E_b}$ that can rotate any vector or matrix from the cell body frame to the lab frame, where $\mathbf{C_b}$, $\mathbf{D_b}$ and $\mathbf{E_b}$ are the rotations $\vec{\mathbf{\Omega}}_b t$ about the $\hat{\mathbf{x}}$, $\hat{\mathbf{y}}$ and $\hat{\mathbf{z}}$ directions respectively.

The flagellar filament is a left-handed helix described by,

$$\vec{\boldsymbol{h}} = R_h \sin(ks)\hat{\mathbf{i}} + R_h \cos(ks)\hat{\mathbf{j}} + s\cos\beta\hat{\mathbf{k}}, \tag{5.26}$$

where $s = [0..\ell_{ax}/\cos\beta]$ is the position on the helix, $k = \pm 2\pi/\lambda$ and $\hat{\mathbf{i}} - \hat{\mathbf{j}} - \hat{\mathbf{k}}$ form the orthonormal helix frame, shown in Fig. 5.7 together with the helix parameters. The sign of k determines if the helix is left ($k > 0$) or right ($k < 0$) handed. For each flagellum, the attachment point on the cell body is defined as $[u_i, v_i]$ where $i = 1..N_f$. The attachment point of the flagellar filament on the cell body is fixed, but the flagellar filament can rotate with respect to the cell body. To describe these rotations we first define the cell body surface frame. The orthonormal cell body surface frame is described by two tangents to the surface and one surface normal, given by

$$\hat{\mathbf{T}}_i^{(1)} = \frac{1}{\sqrt{a^2\cos^2 v_i + c^2\sin^2 v_i}}(a\cos u_i\cos v_i, a\sin u_i\cos v_i, -c\sin v_i), \tag{5.27}$$

$$\hat{\mathbf{T}}_i^{(2)} = (-\sin u_i, \cos u_i, 0), \tag{5.28}$$

and

$$\hat{\mathbf{N}}_i = \frac{1}{\sqrt{c^2\sin^2 v_i + a^2\cos^2 v_i}}(c\sin v_i\cos u_i, c\sin v_i\sin u_i, a\cos v_i), \tag{5.29}$$

respectively. Hence, to transform between the cell body surface frame and the cell body frame we use the matrix

$$\mathbf{A}_i = \begin{pmatrix} \frac{a\cos u_i\cos v_i}{\sqrt{a^2\cos^2 v_i + c^2\sin^2 v_i}} & \frac{a\sin u_i\cos v_i}{\sqrt{a^2\cos^2 v_i + c^2\sin^2 v_i}} & \frac{-c\sin v_i}{\sqrt{a^2\cos^2 v_i + c^2\sin^2 v_i}} \\ -\sin u_i & \cos u_i & 0 \\ \frac{c\sin v_i\cos u_i}{\sqrt{c^2\sin^2 v_i + a^2\cos^2 v_i}} & \frac{c\sin v_i\sin u_i}{\sqrt{c^2\sin^2 v_i + a^2\cos^2 v_i}} & \frac{a\cos v_i}{\sqrt{c^2\sin^2 v_i + a^2\cos^2 v_i}} \end{pmatrix}, \tag{5.30}$$

which takes vectors from the $\hat{\mathbf{x}} - \hat{\mathbf{y}} - \hat{\mathbf{z}}$ cell body frame to the $\hat{\mathbf{T}}_i^{(1)} - \hat{\mathbf{T}}_i^{(2)} - \hat{\mathbf{N}}_i$ cell body surface frame. To transform from the cell body surface frame to the $\hat{\mathbf{x}} - \hat{\mathbf{y}} - \hat{\mathbf{z}}$ cell body frame, we use $\mathbf{A}_i^{-1}$.

Connecting the cell body to the flagellar filament is the hook. As in the rod model we ignore the hook hydrodynamics, and again consider the hook as a hinged spring. As in the rod model the 'neutral" position of the hook is when the helix axis is aligned with the cell body surface normal, meaning there is no elastic torque at this point. Thus we consider rotations away from the cell body surface frame. To do this we define 3 successive rotations, using the 3-1-3 Euler angle formulation, shown in Fig. 5.8. The

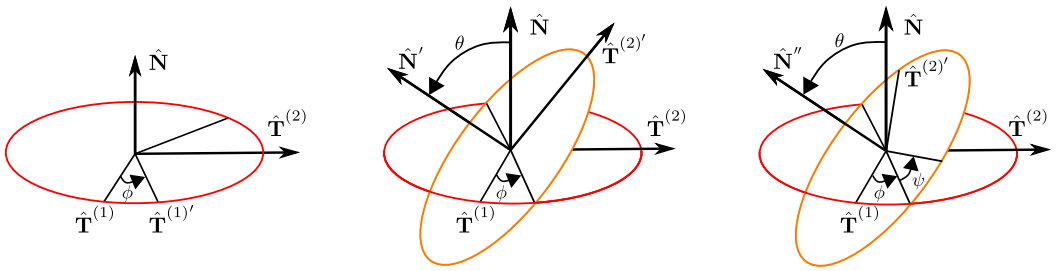

Fig. 5.8 The Euler angles are defined as three successive rotations.

first rotation is about the $\hat{\mathbf{N}}$ axis, by ϕ, the precession angle, secondly a rotation about the rotated $\hat{\mathbf{T}}^{(1)'}$ axis by θ, the tilt angle, and finally a rotation about the helix axis $\hat{\mathbf{k}}$ (or the rotated $\hat{\mathbf{N}}''$ axis) by ψ the roll angle. The first rotation matrix is given by

$$\mathbf{E} = \begin{pmatrix} \cos\phi & \sin\phi & 0 \\ -\sin\phi & \cos\phi & 0 \\ 0 & 0 & 1 \end{pmatrix}, \tag{5.31}$$

the second by,

$$\mathbf{D} = \begin{pmatrix} 1 & 0 & 0 \\ 0 & \cos\theta & \sin\theta \\ 0 & -\sin\theta & \cos\theta \end{pmatrix}, \tag{5.32}$$

and the third by

$$\mathbf{C} = \begin{pmatrix} \cos\psi & \sin\psi & 0 \\ -\sin\psi & \cos\psi & 0 \\ 0 & 0 & 1 \end{pmatrix}, \tag{5.33}$$

such that the full Euler transformation matrix is given by $\mathbf{B} = \mathbf{CDE}$, this matrix transforms vectors from the $\hat{\mathbf{T}}_i^{(1)} - \hat{\mathbf{T}}_i^{(2)} - \hat{\mathbf{N}}_i$ cell body surface frame to the flagella frame, $\hat{\mathbf{i}} - \hat{\mathbf{j}} - \hat{\mathbf{k}}$. The rotation rate of each of the Euler angles form a non-orthogonal basis $(\dot{\phi}, \dot{\theta}, \dot{\psi})$, that we write in the orthogonal $\hat{\mathbf{i}} - \hat{\mathbf{j}} - \hat{\mathbf{k}}$ helix frame using

$$\vec{\boldsymbol{\omega}}'' = \dot{\phi}\hat{\mathbf{N}} + \dot{\theta}\hat{\mathbf{T}}'_1 + \dot{\psi}\hat{\mathbf{k}}. \tag{5.34}$$

Inserting the relevant vectors and rotation matrices,

$$\vec{\boldsymbol{\omega}}'' = \dot{\phi}\mathbf{B}\begin{pmatrix} 0 \\ 0 \\ 1 \end{pmatrix} + \dot{\theta}\mathbf{C}\begin{pmatrix} 1 \\ 0 \\ 0 \end{pmatrix} + \dot{\psi}\begin{pmatrix} 0 \\ 0 \\ 1 \end{pmatrix}, \tag{5.35}$$

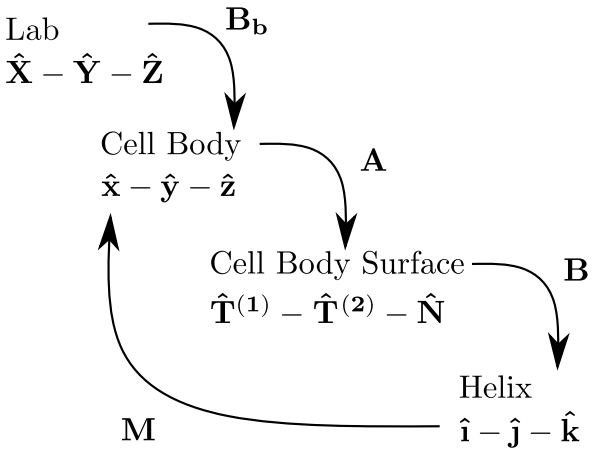

Fig. 5.9 The four reference frames described in this section, and the rotations between them.

such that

$$\vec{\boldsymbol{\omega}}'' = \begin{pmatrix} \dot{\phi}\sin\theta\sin\psi + \dot{\theta}\cos\psi \\ \dot{\phi}\sin\theta\cos\psi - \dot{\theta}\sin\psi \\ \dot{\psi} + \dot{\phi}\cos\theta \end{pmatrix}. \tag{5.36}$$

This allows us to convert flagellar filament angular velocities to Euler angles and *vice versa*. We now have the angular velocity of the flagella in the flagella frame. However, when using Euler angles we must take care when describing the angle dynamics. If $\theta = 0$ is fixed then ϕ and ψ are indistinguishable from one another as they are rotations about the same axis. The system is thus over defined by ϕ and ψ, as we only have one equation for the dynamics of both angles

$$\begin{pmatrix} 0 \\ 0 \\ \dot{\phi} + \dot{\psi} \end{pmatrix} = \vec{\boldsymbol{\omega}}''. \tag{5.37}$$

This is known as the gimbal lock and is present in all Euler angle formulations, either at $\theta = 0$ or $\theta = \pi/2$. A summary of the rotation matrices described in the section are given in Fig. 5.9.

Modelling the full swimming bacterium, with any rotation of the filament relative to the motor, can be split into two simpler problems. Firstly the rigid case where the flagellar filament does not feel any effects of the flow field created by the swimming bacterium, *i.e.* the hook is infinitely stiff. Hence we solve for the velocity and angular velocity for a given flagellar filament angular velocity. Secondly the case of a bacterium

stuck to a surface, where the cell body is fixed and the flagellar filament rotates due to an external imposed flow field.

5.4 Cell body motion with fixed flagellar filament motion

Assuming that there is no feedback between the flow field generated and the position of the helix, we calculate the velocity and the angular velocity of the bacterium given the angular dynamics of the flagellar filament(s). We first consider a single flagellum attached to a cell body, similar to Ref. [179], then extend this to N_f flagella.

The force $\vec{\boldsymbol{F}}_b$, and torque $\vec{\boldsymbol{L}}_b$, exerted by the fluid on the cell body is given by

$$\begin{pmatrix} \vec{\boldsymbol{F}}_b \\ \vec{\boldsymbol{L}}_b \end{pmatrix} = \mathbf{R_b} \begin{pmatrix} \vec{\boldsymbol{U}}_b \\ \vec{\boldsymbol{\Omega}}_b \end{pmatrix}, \tag{5.38}$$

where $\vec{\boldsymbol{U}}_b$ and $\vec{\boldsymbol{\Omega}}_b$ are the unknown body velocity and angular velocity respectively. For an ellipsoidal body the 6×6 cell body resistance matrix,

$$\mathbf{R_b} = - \begin{pmatrix} R_b(1,1) & 0 & 0 & 0 & 0 & 0 \\ 0 & R_b(2,2) & 0 & 0 & 0 & 0 \\ 0 & 0 & R_b(3,3) & 0 & 0 & 0 \\ 0 & 0 & 0 & R_b(4,4) & 0 & 0 \\ 0 & 0 & 0 & 0 & R_b(5,5) & 0 \\ 0 & 0 & 0 & 0 & 0 & R_b(6,6) \end{pmatrix}, \tag{5.39}$$

where

$$R_b(1,1) = R_b(2,2) = \frac{6\pi\mu c(16e^3)}{3(2e + (3e^2 - 1) * L)}, \tag{5.40}$$

$$R_b(3,3) = \frac{6\pi\mu c(8e^3)}{3(-2e + (1 + e^2)L)}, \tag{5.41}$$

$$R_b(4,4) = R_b(5,5) = \frac{8\pi\mu c^3(4e^3(2 - e^2)}{3(-2e + (1 + e^2)L)}, \tag{5.42}$$

$$R_b(6,6) = \frac{8\pi\mu c^3(4e^3(1 - e^2))}{3(2e - (1 - e^2)L)}, \tag{5.43}$$

with

$$L = \ln\left(\frac{1 + e}{1 - e}\right) \tag{5.44}$$

and e described in Eq. (5.17). The body resistance matrix $\mathbf{R_b}$ is centred at the cell body centre, and all rotations are about this point.

The flagellar filament base is fixed to the cell body, but it can rotate about this point, giving the kinematic boundary condition in the flagella frame

$$\begin{pmatrix} \vec{\boldsymbol{U}}_f'' \\ \vec{\boldsymbol{\Omega}}_f'' \end{pmatrix} = \begin{pmatrix} \vec{\boldsymbol{U}}_b'' \\ \vec{\boldsymbol{\Omega}}_b'' \end{pmatrix} + \begin{pmatrix} 0 \\ \vec{\boldsymbol{\omega}}'' \end{pmatrix}, \tag{5.45}$$

where where $\vec{\boldsymbol{U}}_f''$ and $\vec{\boldsymbol{\Omega}}_f''$ are the flagellar filament velocity and angular velocity respectively, and $\vec{\boldsymbol{\omega}}''$ is the relative rotation of the flagellar filament with respect to the cell body, which is imposed in this section.

The force $\vec{\boldsymbol{F}}_f$, and torque $\vec{\boldsymbol{L}}_f$, exerted by the fluid on the flagellar filament is given by

$$\begin{pmatrix} \vec{\boldsymbol{F}}_f'' \\ \vec{\boldsymbol{L}}_f'' \end{pmatrix} = \mathbf{R_f}'' \begin{pmatrix} \vec{\boldsymbol{U}}_f'' \\ \vec{\boldsymbol{\Omega}}_f'' \end{pmatrix}, \tag{5.46}$$

where

$$\mathbf{R_f}'' = \begin{pmatrix} \mathbf{D_a}'' & \mathbf{D_b}'' \\ \mathbf{D_b}''^T & \mathbf{D_c}'' \end{pmatrix}. \tag{5.47}$$

is the symmetric 6×6 flagellar filament resistance matrix, centred at the base of the flagellar filament about which it can rotate. The resistance matrix was calculated using slender-body theory, by Debasish Das. For a flagellum of the shape of the normal form *E. coli* flagellum we have

$$\mathbf{R_f}'' = \begin{pmatrix} -9.4051 & -0.0189 & -0.1068 & 0.1008 & -19.2894 & -0.0430 \\ -0.0189 & -9.3928 & -0.0775 & 19.2462 & 0.0289 & -0.0313 \\ -0.1068 & -0.0775 & -6.4348 & 0.0245 & -0.3167 & -0.1635 \\ 0.1008 & 19.2462 & 0.0245 & -135.0982 & 0.3410 & -0.1184 \\ -19.2894 & 0.0289 & -0.3167 & 0.3415 & -135.5565 & -0.4756 \\ -0.0430 & -0.0313 & -0.1635 & -0.1184 & -0.4756 & -0.3311 \end{pmatrix}. \tag{5.48}$$

Eq. (5.46) is written in the helix frame hence we need to rotate to the cell body frame, and move the resistance matrix centre from the surface of the cell to the centre of the cell.

To write the flagellum resistance matrix $\mathbf{R_f}''$ in the cell body frame we must first rotate $\mathbf{R_f}''$ from the helix frame $(\hat{\mathbf{i}} - \hat{\mathbf{j}} - \hat{\mathbf{k}})$ to the cell body frame, we rotate each of the 3×3 matrices in the full resistance matrix by the (3×3) transformation matrix

$\mathbf{M}$, such that

$$\mathbf{R_f}' = \begin{pmatrix} \mathbf{M} & \mathbf{0} \\ \mathbf{0} & \mathbf{M} \end{pmatrix} \begin{pmatrix} \mathbf{D_a}'' & \mathbf{D_b}'' \\ \mathbf{D_b}''^T & \mathbf{D_c}'' \end{pmatrix} \begin{pmatrix} \mathbf{M}^{-1} & \mathbf{0} \\ \mathbf{0} & \mathbf{M}^{-1} \end{pmatrix} \tag{5.49}$$

This gives the resistance matrix centred at the end of the flagella in the cell body frame. However in order to sum the body and flagella torque we need the resistance matrices centred at the same point. As the cell is rigid, the angular velocity at two different points on the cell body is constant, however the velocity at two different points on the body changes if the cell rotates. Representing forces, torques, velocities and angular velocities at the end of the helix with a dash, and at the cell body centre without, we shift the flagellar force and torque from the cell body surface to the cell body centre, separated by distance

$$\vec{\boldsymbol{r}} = (a\cos u \sin v, a \sin u \sin v, c \cos v)\,. \tag{5.50}$$

The angular velocity is fixed at both points $\vec{\boldsymbol{\Omega}}_f = \vec{\boldsymbol{\Omega}}_f'$, however the velocity at the cell body centre is given by $\vec{\boldsymbol{U}} = \vec{\boldsymbol{U}}' + \vec{\boldsymbol{\Omega}}_f \times \vec{\boldsymbol{r}}$, hence

$$\begin{pmatrix} \vec{\boldsymbol{U}}_f \\ \vec{\boldsymbol{\Omega}}_f \end{pmatrix} = \begin{pmatrix} \mathbf{I} & \mathbf{R}_\epsilon \\ \mathbf{0} & \mathbf{I} \end{pmatrix} \begin{pmatrix} \vec{\boldsymbol{U}}_f' \\ \vec{\boldsymbol{\Omega}}_f' \end{pmatrix}, \tag{5.51}$$

where $\mathbf{R}_\epsilon = -\mathbf{r} \cdot \epsilon$ shifts matrices and vectors from the surface of the body to the centre of the cell body, with ϵ representing the Levi-Civita 3rd order tensor. Similarly to the angular and body velocity, the force and torque centred at the two different points are related by $\vec{\boldsymbol{F}}_f = \vec{\boldsymbol{F}}_f'$ and $\vec{\boldsymbol{L}}_f = \vec{\boldsymbol{L}}_f' - \vec{\boldsymbol{F}}_f \times \vec{\boldsymbol{r}}$, such that

$$\begin{pmatrix} \vec{\boldsymbol{F}}_f \\ \vec{\boldsymbol{L}}_f \end{pmatrix} = \begin{pmatrix} \mathbf{I} & \mathbf{0} \\ \mathbf{R}_\epsilon & \mathbf{I} \end{pmatrix} \begin{pmatrix} \vec{\boldsymbol{F}}_f' \\ \vec{\boldsymbol{L}}_f' \end{pmatrix}. \tag{5.52}$$

Hence we can rewrite Eq. (5.46) centred at the cell body centre as,

$$\begin{pmatrix} \vec{\boldsymbol{F}}_f \\ \vec{\boldsymbol{L}}_f \end{pmatrix} = \mathbf{R_f} \begin{pmatrix} \vec{\boldsymbol{U}}_f \\ \vec{\boldsymbol{\Omega}}_f \end{pmatrix}, \tag{5.53}$$

where

$$\mathbf{R_f} = \begin{pmatrix} \mathbf{I} & \mathbf{0} \\ \mathbf{R}_\epsilon & \mathbf{I} \end{pmatrix} \begin{pmatrix} \mathbf{M} & \mathbf{0} \\ \mathbf{0} & \mathbf{M} \end{pmatrix} \mathbf{R_f}'' \begin{pmatrix} \mathbf{M}^{-1} & \mathbf{0} \\ \mathbf{0} & \mathbf{M}^{-1} \end{pmatrix} \begin{pmatrix} \mathbf{I} & \mathbf{R}_\epsilon \\ \mathbf{0} & \mathbf{I} \end{pmatrix}^{-1}. \tag{5.54}$$

For a single flagellum the low Reynolds force balance is then given in the cell body frame as

$$\begin{pmatrix} \vec{\boldsymbol{F}}_f \\ \vec{\boldsymbol{L}}_f \end{pmatrix} + \begin{pmatrix} \vec{\boldsymbol{F}}_b \\ \vec{\boldsymbol{L}}_b \end{pmatrix} = \mathbf{0}. \tag{5.55}$$

Together with the kinematic boundary condition (Eq. (5.45)) and the force-velocity and torque-angular velocity relationships (Eqs. (5.53) and (5.38)) we have

$$\begin{pmatrix} \vec{\boldsymbol{U}}_b \\ \vec{\boldsymbol{\Omega}}_b \end{pmatrix} = -\left(\mathbf{R_b} + \mathbf{R_f}\right)^{-1} \mathbf{R_f} \begin{pmatrix} \vec{\boldsymbol{u}}_f \\ \vec{\boldsymbol{\omega}} \end{pmatrix}. \tag{5.56}$$

Where we have written the relative flagella motion in the cell body frame, centered at the cell body centre using

$$\begin{pmatrix} \mathbf{R}_\epsilon \vec{\boldsymbol{\omega}} \\ \vec{\boldsymbol{\omega}} \end{pmatrix} = \begin{pmatrix} \mathbf{I} & \mathbf{R}_\epsilon \\ \mathbf{0} & \mathbf{I} \end{pmatrix} \begin{pmatrix} 0 \\ \mathbf{M}\vec{\boldsymbol{\omega}}'' \end{pmatrix}, \tag{5.57}$$

such that $\vec{\boldsymbol{u}}_f = \mathbf{R}_\epsilon \mathbf{M} \vec{\boldsymbol{\omega}}''$, and $\vec{\boldsymbol{\omega}} = \mathbf{M}\vec{\boldsymbol{\omega}}''$.

To extend this to multiple flagella, the low Reynolds force and torque balance becomes

$$\sum_0^{N_f} \begin{pmatrix} \vec{\boldsymbol{F}}_f^{(i)} \\ \vec{\boldsymbol{L}}_f^{(i)} \end{pmatrix} + \begin{pmatrix} \vec{\boldsymbol{F}}_b \\ \vec{\boldsymbol{L}}_b \end{pmatrix} = 0. \tag{5.58}$$

and we have N_f kinematic boundary conditions for each of the flagellum,

$$\begin{pmatrix} \vec{\boldsymbol{U}}_f^{(i)} \\ \vec{\boldsymbol{\Omega}}_f^{(i)} \end{pmatrix} = \begin{pmatrix} \vec{\boldsymbol{U}}_b \\ \vec{\boldsymbol{\Omega}}_b \end{pmatrix} + \begin{pmatrix} \mathbf{R}_\epsilon{}^{(i)} \mathbf{M}^{(i)} \vec{\boldsymbol{\omega}}_i \\ \vec{\boldsymbol{\omega}}_i \end{pmatrix}. \tag{5.59}$$

Hence

$$\begin{pmatrix} \vec{\boldsymbol{U}}_b \\ \vec{\boldsymbol{\Omega}}_b \end{pmatrix} = \sum_0^{N_f} -\frac{\mathbf{R_f}^{(i)}}{\left(\mathbf{R_b} + \sum_0^{N_f} \mathbf{R_f}^{(i)}\right)} \begin{pmatrix} \mathbf{R}_\epsilon{}^{(i)} \mathbf{M}^{(i)} \vec{\boldsymbol{\omega}}_i \\ \vec{\boldsymbol{\omega}}_i \end{pmatrix}, \tag{5.60}$$

If all N_f flagella are identical then the resistance matrix in the helix frame $\mathbf{R}_f^{(i)\prime\prime} = \mathbf{R_f}''$ for all i, but due to different attachment points and/or Euler rotations $\mathbf{R_f}^{(i)} \neq \mathbf{R_f}^{(j)}$ if $i \neq j$.

We can thus solve for the bacterium dynamics for a given flagellar filament angle dynamics. For a rigid hook, the only allowed motion is $\omega_x'' = \omega_y'' = 0$ and $\omega_z'' = 2\pi$, non-dimensionalised by the flagellar rotation frequency ν. The θ and ϕ angles are thus fixed and ψ increases linearly. To demonstrate our swimming model we study an example bacterium with a single flagellum attached at the end of the cell.

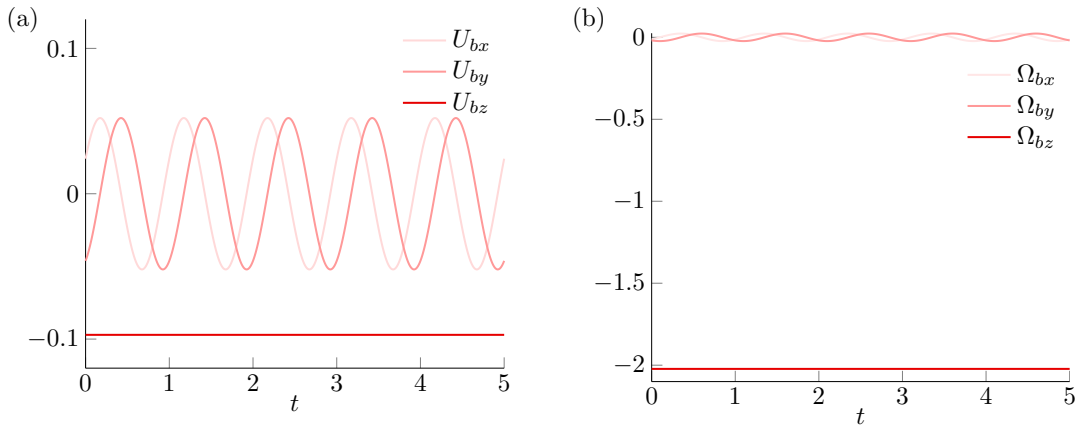

Fig. 5.10 The cell body frame velocity (a) and angular velocity (b) are shown.

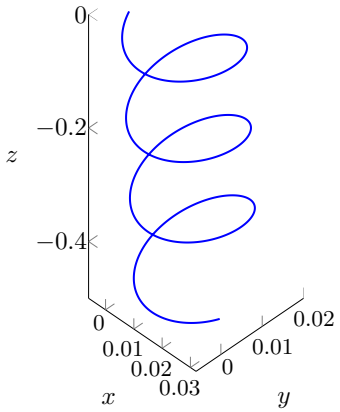

Fig. 5.11 The helical lab frame path of the bacterium is shown.

The flagellum is attached at the end of the cell body, $u = v = 0$, and although we can choose any orientation of the flagellum with respect to the cell body surface, we choose $\theta = 0$ (and $\phi = 0$) such that $\hat{\mathbf{N}} = \hat{\mathbf{k}}$. We solve the bacterium dynamics using an explicit Euler method.

Fig. 5.10 shows the cell body frame velocity and angular velocity for a pusher swimmer and Fig. 5.11 shows the the lab frame path of the cell, which is helical, as expected. We can calculate the swimming speed that would be measured experimentally as the distance away from the cell start point divided by the time it took to get there. We thus calculate $U = 14\,\mu\text{ms}^{-1}$, which is close to the measured *E. coli* swimming speed of $25\,\mu\text{ms}^{-1}$.

If the angular velocity of the flagellum is negative then the swimmer becomes a puller and the cell swims in the opposite direction.

5.5 Flagellar filament motion with fixed cell body motion

We next consider a bacterium stuck on a surface or fixed in place by an optical trap, and impose a flow field around the cell, such that the motion of the flagellum does not affect the motion of the cell body. The aim is to calculate the flagellar filament angular velocity $\vec{\boldsymbol{\omega}}$ for a given body frame velocity $\vec{\boldsymbol{U}}_b$ and angular velocity $\vec{\boldsymbol{\Omega}}_b$. To do this there are three torques to consider: fluid torque; elastic torque and motor torque. We calculate each of these in the flagellar filament frame and consider the torque of the flagellar filament acting on the fluid, so that they can be summed.

5.5.1 Fluid torque

We start from the force and torque balance in the helix frame, Eq. (5.46), that gives the force and torque on the flagellar filament given the flagellar filament velocity in the helix frame. From the bacterium boundary conditions, Eq. (5.45), and the helix frame force and torque balance, Eq. (5.46),

$$\begin{pmatrix} \vec{\boldsymbol{F}}''_f \\ \vec{\boldsymbol{L}}''_f \end{pmatrix} = \begin{pmatrix} \mathbf{D}''_a & \mathbf{D}''_b \\ \mathbf{D}''^T_b & \mathbf{D}''_c \end{pmatrix} \begin{pmatrix} \mathbf{M}^{-1} & \mathbf{0} \\ \mathbf{0} & \mathbf{M}^{-1} \end{pmatrix} \begin{pmatrix} \mathbf{I} & \mathbf{R}_\epsilon \\ \mathbf{0} & \mathbf{I} \end{pmatrix}^{-1} \begin{pmatrix} \vec{\boldsymbol{U}}_b + \vec{\boldsymbol{u}}_f \\ \vec{\boldsymbol{\Omega}}_b + \vec{\boldsymbol{\omega}} \end{pmatrix}, \tag{5.61}$$

where we have transformed $\vec{\boldsymbol{U}}_b$ and $\vec{\boldsymbol{\Omega}}_b$ from the cell body frame to the helix frame. This simplifies to

$$\begin{pmatrix} \vec{\boldsymbol{F}}_f'' \\ \vec{\boldsymbol{L}}_f'' \end{pmatrix} = \begin{pmatrix} \mathbf{D}_a'' & \mathbf{D}_b'' \\ \mathbf{D}_b''^T & \mathbf{D}_c'' \end{pmatrix} \begin{pmatrix} \mathbf{M}^{-1}\left(\vec{\boldsymbol{U}}_b - \mathbf{R}_\epsilon \vec{\boldsymbol{\Omega}}_b\right) \\ \mathbf{M}^{-1}\vec{\boldsymbol{\Omega}}_b + \vec{\boldsymbol{\omega}}'' \end{pmatrix} \tag{5.62}$$

The flagellar filament cannot translate relative to the cell body, thus the force balance returns rigid swimming as there are no additional forces. Thus the torque acting on the fluid due to the rod hydrodynamics,

$$\vec{\boldsymbol{L}}_{fluid}'' = \mathbf{D}_\mathbf{b}''^\mathbf{T}\mathbf{M}^{-1}\left(\vec{\boldsymbol{U}}_b - \mathbf{R}_\epsilon \vec{\boldsymbol{\Omega}}_b\right) + \mathbf{D}_\mathbf{c}''\mathbf{M}^{-1}(\vec{\boldsymbol{\Omega}}_b + \mathbf{M}\vec{\boldsymbol{\omega}}''). \tag{5.63}$$

As in the rod model we can split the fluid torque into two torques: one due to the background flow

$$\vec{\boldsymbol{L}}_{back}'' = -\mathbf{D}_\mathbf{b}''^\mathbf{T}\mathbf{M}^{-1}\left(\vec{\boldsymbol{U}}_b - \mathbf{R}_\epsilon \vec{\boldsymbol{\Omega}}_b\right) - \mathbf{D}_\mathbf{c}''\mathbf{M}^{-1}\vec{\boldsymbol{\Omega}}_b, \tag{5.64}$$

and one due to the motion of the flagellar filament relative to the back ground flow,

$$\vec{\boldsymbol{L}}_{\vec{\omega}}'' = \mathbf{D}_\mathbf{c}''\vec{\boldsymbol{\omega}}'', \tag{5.65}$$

where $\vec{\boldsymbol{L}}_{\vec{\omega}}''$ contains the unknown filament angular velocity relative to the body, and $\vec{\boldsymbol{L}}_{back}''$ contains the imposed background conditions.

5.5.2 Elastic torque

To describe the elastic torque we first revisit our Euler angles. In the rod model there was only one angle θ to consider, whereas the full bacterium model is described by three rotations away from the cell surface frame. As before θ describes the angle between the surface normal $\hat{\mathbf{N}}$, and the helix axis $\hat{\mathbf{k}}$, thus generates an elastic torque. The precession angle describes the helix axis position on a cone of fixed θ. We assume that is it only deviations away from the surface normal that generate torques, whereas deviations from the two surface tangents are have no elastic 'cost'. Thus for fixed θ, different ϕ values have the same elastic torque magnitude. Rotations about the filament axis have no elastic penalty as we assume the hook is stiff to torsion and acts as perfect torque transmitter from the motor embedded in the cell body and the flagellar filament, which is accurate for steady motor rotation [180]. The final Euler angle is ψ, the roll angle that describes rotations about the helix axis, which again

doesn't change the magnitude of the angle between the surface normal and the helix axis, hence has no elastic 'cost'. Thus the elastic torque has the form

$$\vec{\boldsymbol{L}}_{elas} = K\theta\hat{\mathbf{H}}, \tag{5.66}$$

where

$$\hat{\mathbf{H}} = \frac{\hat{\mathbf{k}} \times \hat{\mathbf{N}}_{\hat{\mathbf{i}}\hat{\mathbf{j}}\hat{\mathbf{k}}}}{|\hat{\mathbf{k}} \times \hat{\mathbf{N}}_{\hat{\mathbf{i}}\hat{\mathbf{j}}\hat{\mathbf{k}}}|}, \tag{5.67}$$

describes the torque direction. The normal to the cell surface written in the $\hat{\mathbf{i}} - \hat{\mathbf{j}} - \hat{\mathbf{k}}$ helix frame is given by

$$\hat{\mathbf{N}}_{\hat{\mathbf{i}}\hat{\mathbf{j}}\hat{\mathbf{k}}} = \mathbf{B}\begin{pmatrix}0\\0\\1\end{pmatrix} = \begin{pmatrix}\sin\theta\sin\psi\\ \sin\theta\cos\psi\\ \cos\theta\end{pmatrix}, \tag{5.68}$$

and the helix axis in the helix frame is simply $\hat{\mathbf{k}} = (0, 0, 1)$. The hinged spring will work to move the axis of the helix towards the cell body normal. Thus we take the cross product between the normal to the cell surface and the helix axis to find the rotation axis of the torque,

$$\hat{\mathbf{H}} = \begin{pmatrix}-\cos\psi\\ \sin\psi\\ 0\end{pmatrix}. \tag{5.69}$$

Thus

$$\vec{\boldsymbol{L}}_{elas} = K\theta\begin{pmatrix}-\cos\psi\\ \sin\psi\\ 0\end{pmatrix}. \tag{5.70}$$

5.5.3 Motor torque

We consider the motor-hook complex as a perfect torque transmitter, ignoring any hook torsion, hook hydrodynamics or any unsteady motor effects. Thus the torque generated by the motor at the flagellum base embedded in the cell body surface is perfectly transmitted along the hook to the flagellar filament. Thus the motor torque acts only along the helix axis,

$$\vec{\boldsymbol{L}}_m = \begin{pmatrix}0\\0\\L_m\end{pmatrix}, \tag{5.71}$$

where $L_m = 2\pi\nu D_c''(3,3)$. As $D_c''(3,3) < 0$ for a 'normal' form left-handed helix, $L_m < 0$ for a pusher swimmer. Conversely for a puller $L_m > 0$.

5.5.4 Final torque balance

The final torque balance is a sum of the previous torques,

$$\vec{\boldsymbol{L}}_{\vec{\omega}} + \vec{\boldsymbol{L}}_{elas} + \vec{\boldsymbol{L}}_{back} + \vec{\boldsymbol{L}}_{motor} = 0. \tag{5.72}$$

To find $\vec{\boldsymbol{\omega}}$, we rearrange, such that

$$\vec{\boldsymbol{\omega}}'' = -\mathbf{D_c''}^{-1}\left(-\mathbf{D_b''^T M^{-1}}\left(\vec{\boldsymbol{U}}_b - \mathbf{R}_\epsilon\vec{\boldsymbol{\Omega}}_b\right) - \mathbf{D_c''M^{-1}}\vec{\boldsymbol{\Omega}}_b - \begin{pmatrix} -K\theta\cos\psi \\ K\theta\sin\psi \\ L_m \end{pmatrix}\right). \tag{5.73}$$

We invert Eq. (5.36) to write $\vec{\boldsymbol{\omega}}''$ as Euler angles,

$$\dot{\phi} = \frac{\omega_1''\sin\psi + \omega_2''\cos\psi}{\sin\theta}, \tag{5.74}$$

$$\dot{\psi} = \omega_3'' - \frac{\omega_1''\sin\psi + \omega_2''\cos\psi}{\tan\theta}, \tag{5.75}$$

$$\dot{\theta} = \omega_1''\cos\psi - \omega_2''\sin\psi. \tag{5.76}$$

Thus we have three equations for the angle dynamics we can solve numerically for a given start position and given background conditions or cell body motion. We solve for the time evolution of the angles with an explicit Euler method.

To demonstrate the motion of a flagellar filament in flow, we consider two different bacteria stuck in place with a linear external flow field. We start by considering a dead bacterium *i.e.* zero motor torque, and impose $\vec{U}_b = (0,-1,0)$. As an example we first plot the filament dynamics for $K = 10$. In Fig. 5.12, we see that the θ, ϕ and $\dot{\psi}$ reach an oscillatory steady state (a) and the helix rotates mostly about its own axis (b).

To study how the oscillatory steady state angles change with K we define the average of this oscillatory value. The average is found by finding the oscillation frequency using the inbuilt MATLAB function findpeaks and filtering the data using a moving average filter for the mean value at $t = t_{end}$, first ensuring that a steady state is reached before averaging.

As seen in Fig. 5.13a, as the spring constant K is reduced the angle between the helix axis and the surface normal, θ, increases to $\theta = \pi/2$. At $\theta = \pi/2$, $\phi = 0$ such

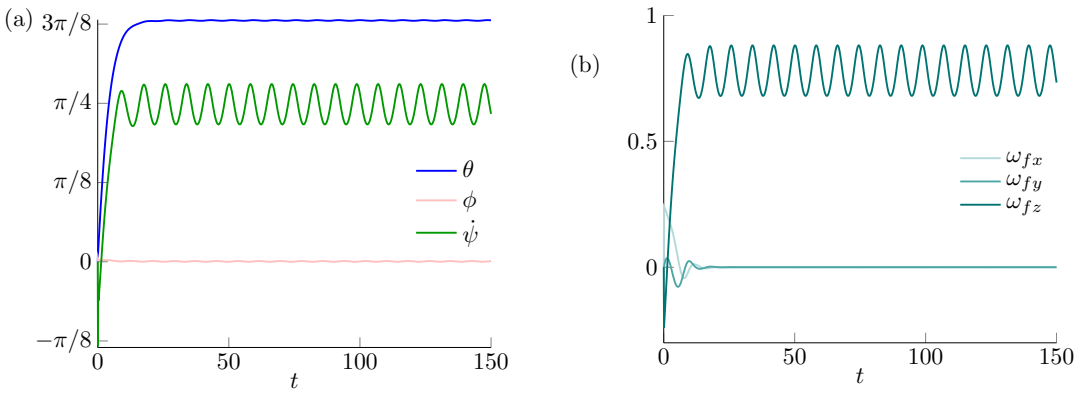

Fig. 5.12 A dead bacterium (*i.e.* no motor torque) is stuck in an external flow field, we plot how the Euler angles (a) and filament angular velocity (b) change with time t.

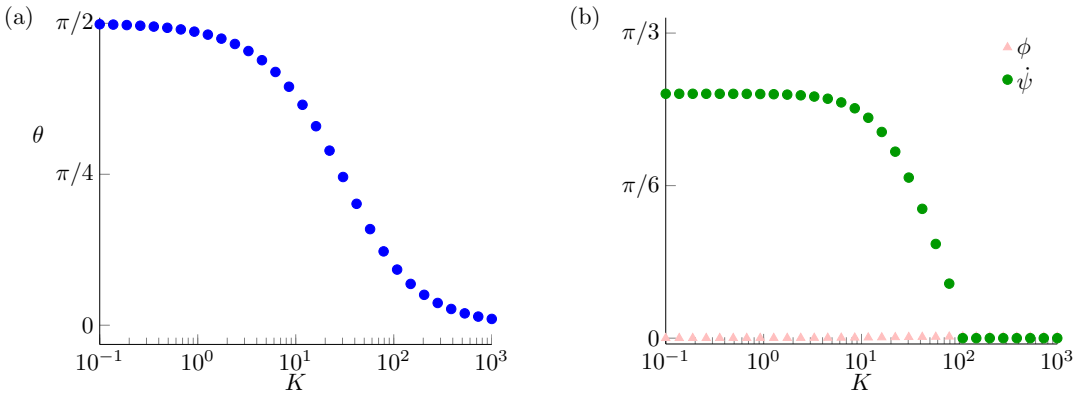

Fig. 5.13 A dead bacterium is stuck in an external flow field, we change the hook stiffness, K, and see that the tilt angle θ increases as K decreases (a). Additionally, the helix rotates faster as K decreases and the precession angle remains small (b).

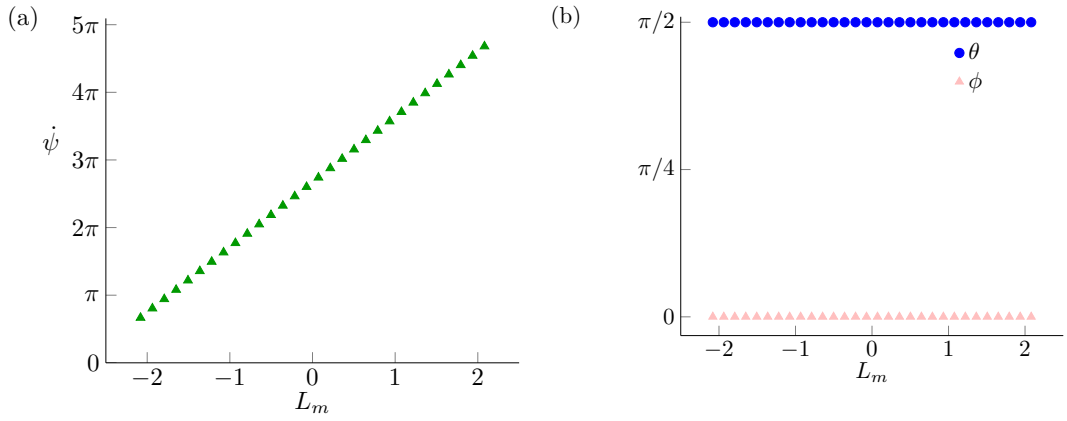

Fig. 5.14 An alive bacterium is stuck in an external flow field, we change the imposed motor torque, L_m from negative to positive. The helix rotation rate $\dot{\psi}$ (a) increases (b) with increasing torque, however the helix tilt angle θ and the precession angle ϕ are unchanged (b).

that the helix axis is aligned perfectly with the flow. Additionally, we see that the helix rotates along its axis with increasing rate as the helix aligns more with the flow, as shown in Fig. 5.13b.

Secondly we consider an alive bacterium that has no resistance to tilt rotations. We again impose no rotational flow but increase the body velocity to $U_b = (0, -10, 0)$ ensuring that the imposed flow dominates the flow generated by the rotation of the flagellar filament. As the motor torque changes from negative to positive we switch from being a pusher to a puller. From Fig. 5.14, the tilt and precession angles are unchanged, and rotation rate of the flagellar filament about its own axis either increases with increasing motor torque.

To fully describe a swimming bacterium we couple the swimming speed of the rigid swimmer to the filament angular frequency from the helix in flow (and *vice versa*).

5.6 Coupling swimming and flagellar motion

Before coupling the results from the previous two sections we must re-visit the force and torque on the bacterium. We split the bacterium into 3 constitutive parts, the body (subscript b), the motor-hook complex (subscript mh) and the flagellar filament (subscript f), and describe the total (superscript t) force and torque on each part. The

total force and torque on the flagellar filament is described by

$$\vec{\boldsymbol{F}}_f^{(t)} = \vec{\boldsymbol{F}}_f, \tag{5.77}$$

$$\vec{\boldsymbol{L}}_f^{(t)} = \vec{\boldsymbol{L}}_f + L_m\hat{\mathbf{k}} + \vec{\boldsymbol{L}}_{elas}. \tag{5.78}$$

Similarly the total force and and torque on the cell body is given by

$$\vec{\boldsymbol{F}}_f^{(t)} = \vec{\boldsymbol{F}}_f, \tag{5.79}$$

$$\vec{\boldsymbol{L}}_f^{(t)} = \vec{\boldsymbol{L}}_b - L_m\hat{\mathbf{N}} - \vec{\boldsymbol{L}}_{elas}. \tag{5.80}$$

The motor torque acts on the cell body normal to the surface as the motor-hook complex is embedded in the cell surface at its base. The elastic torque felt by the cell body is equal and opposite to the elastic torque felt by the flagellar filament. As we ignore the hydrodynamics of the motor-hook complex and treat it as a perfect torque transmitter, there is no force felt by the motor and the motor-hook torque is defined by its boundary conditions

$$\vec{\boldsymbol{L}}_{mh}^{(t)} = \vec{\boldsymbol{L}}_m\hat{\mathbf{N}} - \vec{\boldsymbol{L}}_m\hat{\mathbf{k}}, \tag{5.81}$$

such that the low Reynolds force and torque balance of these three components leaves,

$$\begin{pmatrix} \vec{\boldsymbol{F}}_f + \vec{\boldsymbol{F}}_b \\ \vec{\boldsymbol{L}}_f + \vec{\boldsymbol{L}}_b \end{pmatrix} = \begin{pmatrix} 0 \\ 0 \end{pmatrix} \tag{5.82}$$

as described for the rigid swimmer case. We can now couple the flagellar dynamics and swimming speed. We start with a single flagellated bacterium.

We insert the swimming speed from Eq. (5.56), into Eq. (5.73), such that

$$\vec{\boldsymbol{\omega}}'' = \mathbf{D_c''}^{-1}\left(-\mathbf{D_b''^T}\mathbf{M^{-1}}\left(\left(\mathbf{P_2} - \mathbf{P_4}\mathbf{R}_\epsilon\right)\vec{\boldsymbol{\omega}}''\right) - \mathbf{D_c''}\mathbf{M^{-1}}\mathbf{P_4}\vec{\boldsymbol{\omega}}'' - \begin{pmatrix} K\theta\cos\psi \\ K\theta\sin\psi \\ L_m \end{pmatrix}\right), \tag{5.83}$$

where we have defined the 6×6 matrix

$$\mathbf{P} = \begin{pmatrix} \mathbf{P_1} & \mathbf{P_2} \\ \mathbf{P_2^T} & \mathbf{P_4} \end{pmatrix} = (\mathbf{R_b} + \mathbf{R_f})^{-1}\mathbf{R_f}\begin{pmatrix} \mathbf{R}_\epsilon\mathbf{M} \\ \mathbf{M} \end{pmatrix}. \tag{5.84}$$

Re-arranging for $\vec{\boldsymbol{\omega}}''$ and simplifying, the problem reduces to

$$\mathbf{G}\vec{\boldsymbol{\omega}}'' = \begin{pmatrix} -K\theta\cos\psi \\ K\theta\sin\psi \\ L_m \end{pmatrix} \tag{5.85}$$

where

$$\mathbf{G} = \mathbf{D_c''} + \mathbf{D_b''^T}\mathbf{M^{-1}}\left(\mathbf{P_2} - \mathbf{P_4}\mathbf{R}_\epsilon\right) + \mathbf{D_c''}\mathbf{M^{-1}}\mathbf{P_4}. \tag{5.86}$$

We next extend this to N_f flagella, where $\mathbf{G}_{N_f}$ will be a tensor of size $(3N_f)\times(3N_f)$, such that

$$\begin{pmatrix} \mathbf{G}_1^1 & \mathbf{G}_2^1 & \dots & \mathbf{G}_{N_f}^1 \\ \mathbf{G}_1^2 & \mathbf{G}_2^2 & \dots & \mathbf{G}_{N_f}^2 \\ \vdots & \vdots & \ddots & \vdots \\ \mathbf{G}_1^{N_f} & \mathbf{G}_2^{N_f} & \dots & \mathbf{G}_{N_f}^{N_f} \end{pmatrix} \begin{pmatrix} \vec{\boldsymbol{\omega}}''_{1,f} \\ \vec{\boldsymbol{\omega}}''_{2,f} \\ \vdots \\ \vec{\boldsymbol{\omega}}''_{N_f,f} \end{pmatrix} = \begin{pmatrix} K\theta_1\hat{\mathbf{H}}_1 + \vec{\boldsymbol{L}}_m \\ K\theta_2\hat{\mathbf{H}}_2 + \vec{\boldsymbol{L}}_m \\ \vdots \\ K\theta_{N_f}\hat{\mathbf{H}}_{N_f} + \vec{\boldsymbol{L}}_m \end{pmatrix}. \tag{5.87}$$

We can then define

$$\mathbf{G}_{i,i} = -\mathbf{D_b''^T}\mathbf{M}^{(i)^{-1}}\mathbf{R}_\epsilon{}^{(i)} + \mathbf{D_c''} + \mathbf{D_b''^T}\mathbf{M}^{(i)^{-1}}\left(\mathbf{P_2}^{(i)} - \mathbf{P_4}^{(i)}\mathbf{R}_\epsilon{}^{(i)}\right) + \mathbf{D_c''}\mathbf{M}^{(i)^{-1}}\mathbf{P_4}^{(i)}, \tag{5.88}$$

and

$$\mathbf{G}_{i,j} = \mathbf{D_b''^T}\mathbf{M}^{(i)^{-1}}\left(\mathbf{P_2}^{(i)} + \mathbf{R}_\epsilon{}^{(j)}\mathbf{P_4}^{(i)}\right), \tag{5.89}$$

for $i \neq j$, where

$$\mathbf{P}^{(i)} = \left(\mathbf{R_b} + \sum_0^{N_f}\mathbf{R_f}^{(i)}\right)^{-1}\mathbf{R_f}^{(i)}\begin{pmatrix}\mathbf{I} & \mathbf{R}_\epsilon{}^{(i)} \\ \mathbf{0} & \mathbf{I}\end{pmatrix}\begin{pmatrix}0 \\ \mathbf{M}^{(i)}\end{pmatrix}. \tag{5.90}$$

5.6.1 Steric interaction between flagellum and body

Finally, to ensure that the flagella does not enter the cell body, we introduce a steric interaction between each flagellum and the cell body. As the helix has a non-zero radius at the base of the helix, the tilt angle at which the helix enters the body is any non-zero value of theta. Instead we consider when the helix axis enters the body, thus take $\theta_{s-h} = \pi/2$, with a tapered helix left as further work.

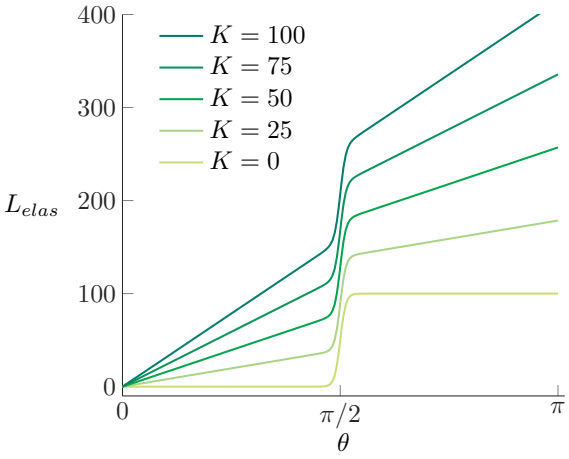

Fig. 5.15 We plot the magnitude of the new steric elastic torque $L_{elas} = \vec{\boldsymbol{L}}_{elas} \cdot \hat{\mathbf{H}}$.

There are two ways in which steric interactions can be included: 1) add a torque that cancels out the torque in the $\hat{\mathbf{i}}$ and $\hat{\mathbf{j}}$ directions when $\theta > \theta_{s-h}$; 2) a rapid increase the spring stiffness K when θ approaches θ_{s-h}. The former introduces the steric torque

$$\vec{\boldsymbol{L}}_{s-h} = -\left(\vec{\boldsymbol{L}}_{\vec{\omega}} + \vec{\boldsymbol{L}}_{elas} + \vec{\boldsymbol{L}}_{back} + \vec{\boldsymbol{L}}_{motor}\right) \cdot \hat{\mathbf{H}}\hat{\mathbf{H}}, \tag{5.91}$$

such that the final torque balance at $\theta = \theta_{s-h}$

$$\left(\vec{\boldsymbol{L}}_{\vec{\omega}} + \vec{\boldsymbol{L}}_{elas} + \vec{\boldsymbol{L}}_{back} + \vec{\boldsymbol{L}}_{motor}\right)\left(\mathbf{I} - \hat{\mathbf{H}}\hat{\mathbf{H}}\right) = 0. \tag{5.92}$$

However $\left(\mathbf{I} - \hat{\mathbf{H}}\hat{\mathbf{H}}\right)$ is singular hence we move to the second option.

For the second option, the most rapid increase possible is a Heaviside step function at θ_{s-h}, but Heaviside functions can cause unphysical oscillations at θ_{s-h}. Thus we need to choose a smooth step function such that as θ tends towards θ_{s-h} there is a smooth but rapid transition from $K\theta$ to a much larger K value. We choose smooth step function, given by

$$f(\theta) = f_{max}\left(1 - \frac{1}{1 + (\theta/\theta_{mid})^{k_s}}\right), \tag{5.93}$$

where θ_{mid} is the value of the midpoint of the increase, f_{max} is the maximum value, and k_s is the steepness. When $f_{max} = 1$, and in the limit $k_s \to \infty$ we recover a step function at θ_{mid}. We take value of the midpoint such that $\theta_{mid} = \theta_{s-h}$, however the choice of f_{max} and k_s is less obvious. They must be chosen such that the linear portion of the elastic torque $K\theta$ is minimally affected by this term (large k_s and f_{max}), but

they must also show a smooth increase with the time step, such that the change in the spring constant is smaller than the time step in the numerical implementation (small k_s and f_{max}). We thus alter the elastic torque to

$$\vec{\boldsymbol{L}}_{elas} = \left(K\theta + 100 \left(1 - \frac{1}{1 + \left(\frac{2\theta}{\pi}\right)^{70}} \right) \right) \hat{\mathbf{H}}, \tag{5.94}$$

which is shown in Fig. 5.15 for some example K values having chosen values of f_{max} and k_s that prohibit the flagellum from entering the body without minimal effects to the dynamics. We simplify notation by defining

$$K_{steric} = K\theta + 100 \left(1 - \frac{1}{1 + \left(\frac{2\theta}{\pi}\right)^{70}} \right). \tag{5.95}$$

5.6.2 Numerical implementation

For a given cell body and flagellum, the primary inputs are $\mathbf{R}_b$, $\mathbf{R}_f''$, $\vec{\boldsymbol{L}}_m$ (assuming all the flagellum are identical) and the point of attachment of these flagellum $\vec{\boldsymbol{r}}^{(i)}$. These quantities do not depend on the Euler angles and hence do not change in time. For a given start position of the cell body and the N_f flagellar filaments, we follow the procedure below with a fourth order Runge-Kutta method, developed in collaboration with Debasish Das.

1. Specify $\mathbf{R_b}$, $\mathbf{R_f}''$ and $\vec{\boldsymbol{r}}^{(i)}$ for N_f flagellum, $i = 1, 2, ..., N_f$.
2. Construct the matrices $\mathbf{A^{(i)}}$.
3. Specify the initial Euler angles ϕ_i, ψ_i and $\theta_i \neq 0$ to avoid the Euler angle singularity.
4. Construct the matrix $\mathbf{M}^{(i)}$ to convert a vector from helix frame to point of flagella attachment frame.
5. Use Eq. (5.54) to convert the Stokes drag law from helix to body centroid frame for each flagella, in other words, calculate $\mathbf{R_f}^{(i)}$ for each flagella.
6. Construct the matrix $\mathbf{G_{N_f}}$ using Eqs. (5.88) and (5.89).

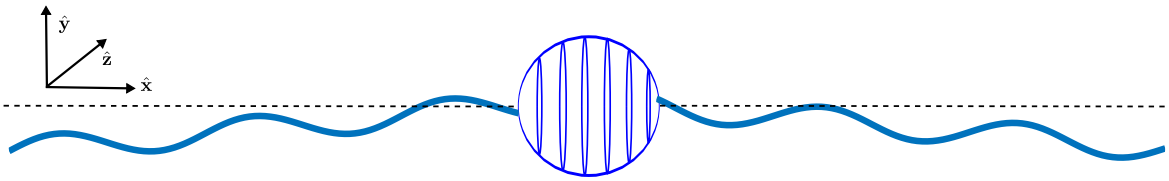

Fig. 5.16 Identical flagella are placed on either side of a spherical cell body.

7. Construct the elastic and motor torque vector

$$\begin{pmatrix} K_{steric}^{(1)}\hat{\mathbf{H}}_1 + \vec{\boldsymbol{L}}_m \\ K_{steric}^{(2)}\hat{\mathbf{H}}_2 + \vec{\boldsymbol{L}}_m \\ K_{steric}^{(3)}\hat{\mathbf{H}}_3 + \vec{\boldsymbol{L}}_m \\ \vdots \\ K_{steric}^{(N_f)}\hat{\mathbf{H}}_{N_f} + \vec{\boldsymbol{L}}_m \end{pmatrix}. \tag{5.96}$$

8. For the time derivatives of the Euler Angles using Eq. (5.74) for each flagella.

9. To find the body frame swimming speed and angular velocity we input the flagellar filament angular velocities into Eq. (5.60).

10. Finally to find the lab frame velocity we use $\mathbf{B_b}^{-1}$ defined as $\mathbf{B_b} = \mathbf{C_b}\mathbf{D_b}\mathbf{E_b}$ where $\mathbf{C_b}$ is a rotation about the $\hat{\mathbf{X}}$ axis by $\Omega_x t$, $\mathbf{D_b}$ is a rotation about the $\hat{\mathbf{Y}}$ axis by $\Omega_y t$ and $\mathbf{E_b}$ is a rotation about the $\hat{\mathbf{Z}}$ axis by $\Omega_z t$.

5.6.3 Two flagella: Pusher

Returning to the symmetric bacterium of the rod model, we place a flagellum on each side of a spherical body ($c = a$), as shown in Fig. 5.16. For a spherical body, the body resistance matrix R_b (Eq. (5.39)) simplifies, such that

$$R_b(1,1) = R_b(2,2) = R_b(3,3) = 6\pi\mu a, \tag{5.97}$$

$$R_b(4,4) = R_b(5,5) = R_b(6,6) = 8\pi\mu a^3. \tag{5.98}$$

As the neutral position of the spring at $\theta = 0$ is singular, we start our simulations with a small initial perturbation $\theta|_{t=0} = 0.05\pi$. The flagella are initially most closely aligned with the $\hat{\mathbf{X}}$-axis, and have identical flagella properties given by the standard *E. coli* parameters given in Table 5.1. We consider a pusher bacterium as found most commonly *in vivo*, such that L_m is negative.

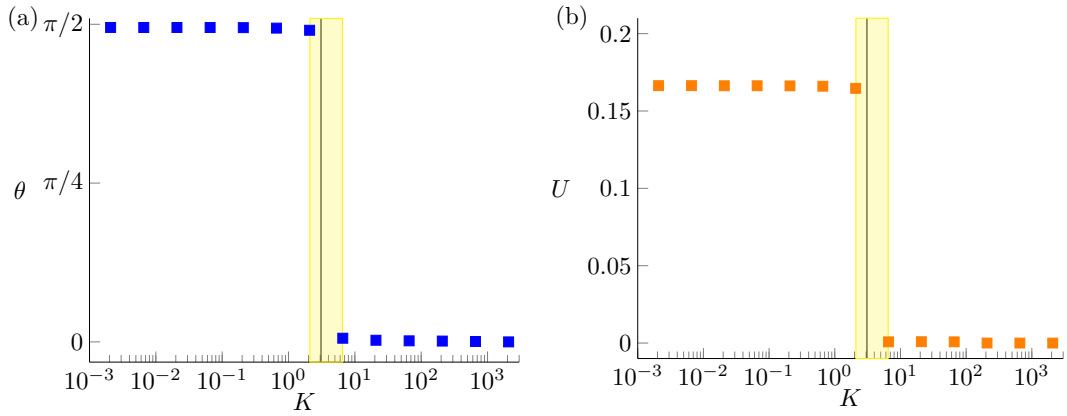

Fig. 5.17 The tilt angle θ and swimming speed U is shown for a range of K values, the black vertical lines show the critical spring constant from the analytic rod model.

As in the rod model we can plot the tilt angles θ and swimming speeds U for a variety of swimmers with different hook stiffnesses K as shown in Fig. 5.17. Similarly to the helix in flow results we use a moving average filter again ensuring that the run time is large enough for the oscillatory steady state to be reached. As we have moved to three dimensions, to define the steady state lab frame swimming speed we average of the velocity, and then normalise such that $U = \left|\left\langle \vec{\boldsymbol{U}} \right\rangle\right|$ gives the average speed of the bacterium. If we compare this to the root mean squared average $\left\langle \left|\vec{\boldsymbol{U}}\right| \right\rangle \neq |\left\langle \vec{\boldsymbol{U}} \right\rangle|$, which would tell us the speed of the bacterium along its lab frame path, meaning that a bacterium that swims in circles could have the same speed as a bacteria that swims in a straight line. Thus, the root mean squared velocity cannot distinguish between successful and unsuccessful swimming.

In Fig. 5.17, we see that there is a transition from negligible swimming to successful swimming when the hook is floppy enough, and that the critical spring constant at which this occurs matches well to the analytic results. The numerical simulations show the critical spring constant $2 < K_c < 8$ (yellow shaded region), compared to the analytic critical spring constant $K_c = 3.1$ (black line), more points are required between $2 < K < 8$ to pinpoint the exact numerical critical spring constant, these preliminary results point show good agreement between the two models, with the analytic spring constant at worst being only 3 times smaller than the one found with the numerical model.

Unlike the rod model the steady state swimming speed is not simply a function of θ. The precession angle for each flagella is $\phi = -0.41$ post-transition and the rotation rate of the flagella about its own axis is given by the rate of change of the roll angle

as $\dot{\psi} = 11$. These values together with the tilt angle θ change by less than 1% in the post transition region $K < 2$. Furthermore taking these values and inputing them into the rigid swimmer model we see an error of less than 1% between the swimming speeds gained from the rigid swimmer model and the full flagella torque balance model. Thus showing that only the average values of these steady states are important to the swimming speed and not the exact oscillatory dynamics of the steady state.

We further note the difference between the profile of the tilt angle θ, and the swimming speed U, compared to the rod model with the numerical model being more stark than the rod model. This could either be due to three-dimensional effects such as the rotation of the body, the precession of the helical filaments or the rotation of the flagella causing oscillatory steady states not present in the rod model.

5.7 Discussion

This chapter studied the tumbling-to-swimming transition observed *in vivo*. We showed both analytically and numerically that there is a critical spring constant below which a pusher bacterium swims and above which negligible swimming occurs, but how do our analytic and numerical values of K_c compare to real bacteria?

Using the definition of $K = EI/\ell_h$, where EI is the Young's modulus of the hook, and ℓ_h is the length of the hook, we can relate the critical torsional spring constant to the hook bending moduli measured in experiments. There are two current measurements of the bending stiffness of the flagellar hook. The earliest studied a range of different bacteria flagellar hooks [181], by extracting and staining the flagellar hooks, and observing their deformations due to thermal fluctuations with electron microscopy. In this study they found that the hook bending stiffness of peritrichously flagellated bacteria, *E. coli*, *Salmonella typhimurium*, and singly flagellated bacteria, *Vibrio cholerae*, *Vibrio parahaemolyticus* were very similar with $EI = 1.6 - 4.8 \times 10^{-28}$ Nm^2, with stiffer hooks found for singly flagellated bacteria. If we compare this to a later study on the bending stiffness of the singly flagellated bacteria *Vibrio alginolyticus* [82]. In this study the hook stiffness was measured by observing the flagellar filament motion of bacteria that are stuck to a surface, resulting in a hook stiffness of 22×10^{-26} Nm^2 when the flagellum rotation compresses the hook, and 3.6×10^{-26} Nm^2 when the flagellum does not rotate. Re-dimensionalising we find $K_c = 7.4 \times 10^{-19}$ Nm analytically and 5×10^{-19} Nm $< K_c < 19 \times 10^{-19}$ Nm numerically, and using $\ell_h = 55$ nm (Table 5.1) we find $EI = 4 \times 10^{-26}$ Nm^2 analytically and 3×10^{-26} Nm$^2 <$ EI $< 10 \times 10^{-26}$ Nm^2

numerically. We see that bacteria flagella are safely below the critical value and hence swim successfully.

Our simple analytic and numerical models correspond well, despite their differences, further work is needed to pin-point K_c numerically. In order to study the critical spring constant for a more realistic bacterium the extension to more realistic flagella numbers is required, *i.e.* 4-7 for *E. coli*. Additionally a puller swimmer needs to be investigated, the rod model predicts that a puller swimmer will never swim for any spring constant K, does the full numerical model predict the same?

In this chapter we explored the swimming of peritrichously flagellated bacteria, and find that the stiffness of the hook is crucial for successful swimming. If the hook is too stiff then the flagellar filaments cannot gather at one end of the cell body in order to bundle. Real bacteria flagella are safely below the critical value and hence swim successfully.

6

Conclusion and Further Work

> *We of today must conceive our relation to the rest of the universe as best we can; and even if our images must seem fantastic to future humans, they may none the less serve their purpose today.*
>
> – Olaf Stapledon, *Last and First Men*

> *Even if I should be right in this, I do not know whether my way of approach is really the best and simplest. But, in short, it was mine.*
>
> – Erwin Schrödinger, *What is Life?*

Low Reynolds locomotion is crucial for the survival and proliferation of both microscale and macroscale organisms. One of the easiest measurements one can make on a single swimmer is its swimming speed. While there are other important factors to successful swimming such as efficiency, and navigation towards more favourable environments, measurements on the swimming speed require little knowledge of the biology of microswimmers (or engineering in the case of biomimetic swimmers). Despite this, the study of swimming speeds of a variety of swimmers with varying elastic and complex fluid effects has not yet managed to create a clear picture as to these effects help or hinder swimming. Ideally from knowledge of the swimmer and fluid type we should be able to make accurate predictions of the swimming speed compared to an equivalent rigid swimmer in a Newtonian fluid, akin to studies on shapes falling in non-Newtonian fluids. However, these goals remain elusive. In this thesis we have probed four different swimmers to glean insights into the physical affects that may cause a swimmer to propel faster or slower in different fluids and with varying swimmer stiffness.

We first explored a rigid swimmer within a shear-thinning fluid. Using empirical modelling we built a non-Newtonian resistive-force theory for slender filaments in

shear-thinning fluids. Previous research on flagellar based swimming in shear-thinning fluids was constrained to small amplitude studies or complex numerical simulations, while with our model the swimming speed of more realistic amplitude swimmers can be investigated with only a simple addition to Newtonian resistive-force theory. Though this empirical model is only valid within a short range of actuation frequencies and fluid properties, it describes the physical effect of the thinned region close to the whip-like flagellum. This model was applied to a generic planar wave swimmer that we show is always slowed down within shear-thinning fluids (Figs 2.7 and 2.8). We attribute this to the drag shear-rate being much smaller than the thrust shear rate, hence the thrust is reduced more by the shear-thinning effects. The results of this simple planar wave swimmer match well with experimental results on the swimming of *C. elegans* without any fitting parameters (Fig 2.12). We discussed the two possible effects of swimming in a shear-thinning environment 1) due to swimming in a low viscosity region (soft-confinement) and 2) due to the thinned region around the rod. Interesting further work would be to study experimentally when each of the two competing shear-thinning fluid effects dominate the swimming speed result, and furthermore how well does this match with our regime of validity ($\Gamma\nu < 0.09$). For a given fluid (or swimmer) the swimming speed could be measured for a rigid propeller (such that the flow does not affect the shape of the swimmer) at varying actuation frequencies (or varying critical shear-rates $1/\Gamma$). Based on whether the swimmer goes faster or slower would demonstrate when these two effects occur, or indeed whether there are further additional effects of shear-thinning fluids that need to be considered such as end effects or detailed interactions between particles within the fluid and the swimmer.

Secondly, we moved to fluids with viscoelastic effects. By considering a rigid planar wave swimmer with all possible waveform modes we showed that swimming speed enhancement can be found swimming in a non-Newtonian verses a Newtonian fluid if there are waves travelling forwards and backwards with different oscillation frequencies (Eq. (3.34)). As the waves have different modes of oscillation the damping effects of viscoelasticity affect the wave mode more or less depending on the size of the oscillation mode. Swimming with both forwards and backwards waves is always slower for waves with only forward components for both Newtonian and non-Newtonian fluids. There are swimmers *in vivo* that have forwards and backwards modes however the wave modes have the same mode of oscillation, hence this speed enhancement mechanism is not applicable. Beyond a two mode swimmer, we were also able to show that the swimming speed and the direction of a three wave swimmer was altered by the viscoelasticity

of the fluid (Fig. 3.9) This indicates a possible rheometer design or swimmer sorting mechanism.

Thirdly, staying in viscoelastic fluid we determined another physical mechanism for enhanced propulsion, this time without the need for backward moving waves. We moved from the rigid swimmer limit considered by previous chapters to active swimming. Here the fluid affects the shape of the swimmer though a balance of elastic, viscous and active forces. The amplitude of the swimmer in a non-Newtonian fluid is larger than the amplitude in a Newtonian fluid for sufficiently large viscoelastic effects, due to reduced pressure on the swimmer in the non-Newtonian fluid. Under certain non-Newtonian fluid properties and elastic swimmer properties this increase in amplitude can overcome the viscoelastic damping effects (Fig. 4.1). Previous experimental and numerical results on swimming in viscoelastic fluids attributed enhancement to high amplitude and end effects, our results on small-amplitude swimmers in viscoelastic fluids show that swimming speed enhancement can arise even for infinite small amplitude swimmers.

For further work on swimming sheets in viscoelastic fluids, both of our studies on Taylor's swimming sheet in a viscoelastic fluid could be extended to other viscoelastic fluid models, such as those that include finite polymer lengths, and shear-thinning effects. A previous study showed that these were all the same up to 2nd order in the expansion of the amplitude [44], so we expect the results of the previous two chapters to hold for these more realistic models to second order in the expansion of the amplitude. Fourth order swimming has been considered in Newtonian fluids [9], but the extension to non-Newtonian fluids is currently missing. Furthermore swimming in shear-thinning viscoelastic fluids and constant viscosity viscoelastic fluids was found to be hindered and enhanced respectively experimentally [110]. Though this elastic sheet experiment matches our prediction that elasto-hydrodynamic effects enhance the swimming speed, calculation of a circular Taylor's swimming sheet would allow quantitative comparisons. Additionally, study of elasto-hydrodynamic effects as well as rigid swimmers in a shear-thinning viscoelastic fluid would allow access to further insights into the differences between the purely viscoelastic fluids studied previously in this thesis and a shear-thinning viscoelastic fluid in the small amplitude limit.

Finally, transitioning to Newtonian fluids we probed the effects of elasticity on microscale propulsion. We extended the previous planar wave swimmer studies to helical swimmers and moved from singly flagellated swimmers to multi-flagellated peritrichous bacteria. As the bacterium flagellar filament is much stiffer than the hook, we only consider the elastic effects of the hook. Using both a simple two dimensional rod model and a more realistic three dimensional helical flagellar filament we show that

there is a critical hook elasticity below which the bacterium swims. By ignoring the hydrodynamic effects of the flagellar filaments we are able to show that the gathering of flagella at one end of the body can be attributed to an elasto-hydrodynamic instability. Further extensions to this work include, more realistic flagella numbers, symmetric and non-symmetric bacteria, and un-bundling. The rod model successfully predicts the critical spring constant at which the bacterium transitions from a small amount of motion to successful swimming. To further compare the rod and helical swimmers there are further numerical studies we can undertake to test its applicability. Namely, comparing the critical spring constant for increasing flagellar filament lengths and increased motor torque.

To summarise, we have described four physical mechanisms that alter the swimming speed of a low Reynolds number organism. Whether these affects effect the lives of micro-swimmers is not obvious, but for each case the regime of validity has been discussed, and suggestions for further experimental and theoretical studies have been made. While some of the mechanisms behind swimming and flow generation may not yet be fully understood, our fascination with these microswimmers shows no sign of dwindling as the fields of physics and biology further intertwine.

References

[1] S. Vogel. *Life in Moving Fluids*. Princeton University Press, Princeton, NJ, 1996.

[2] C. Dobell and A. V. Leeuwenhoek. *Antony van Leeuwenhoek and his "little animals"*. Harcourt, Brace and company, New York, 1932.

[3] E. M. Purcell. Life at low Reynolds number. *Am. J. Phys.*, 45:3–11, 1977.

[4] E. M. Purcell. The efficiency of propulsion by rotating flagellum. *Proc. Natl. Acad. Sci. USA*, 94:11307–11311, 1997.

[5] C. Brennen and H. Winet. Fluid mechanics of propulsion by cilia and flagella. *Ann. Rev. Fluid. Mech.*, 9:339–398, 1977.

[6] A. Bilbao, E. Wajnryb, S. A. Vanapalli, and J. Blawzdziewicz. Nematode locomotion in unconfined and confined fluids. *Phys. Fluids*, 25:081902, 2013.

[7] S. Park, H. Hwang, S.-W. Nam, F. Martinez, R. H. Austin, and W. S. Ryu. Enhanced *Caenorhabditis elegans* locomotion in a structured microfluidic environment. *PLoS ONE*, 3(6):e2550, 2008.

[8] E. Lauga and T. R. Powers. The hydrodynamics of swimming microorganisms. *Rep. Prog. Phys.*, 72:096601–096637, 2009.

[9] G. I. Taylor. Analysis of the swimming of microscopic organisms. *Proc. R. Soc. London Ser. A*, 209:447–461, 1951.

[10] G. I. Taylor. The action of waving cylindrical tails in propelling microscopic organisms . *Proc. Roy. Soc. A*, 211:225–239, 1952.

[11] M. Sauzade, G. J. Elfring, and E. Lauga. Taylor's swimming sheet: Analysis and improvement of the perturbation series. *Physica D*, 240:1567–1573, 2011.

[12] J. R. Blake. A spherical envelope approach to ciliary propulsion. *J. Fluid Mech.*, 46(1):199–208, 1971.

[13] M. J. Lighthill. On the squirming motion of nearly spherical defomable bodies through liquids at very small Reynolds numbers . *Commun. Pur. Appl. Math.*, 109:118, 1952.

[14] T. J. Pedley. Spherical squirmers: Models for swimming micro-organisms. *IMA J. Appl. Math.*, 812:488–521, 2016.

[15] M. L. Ginger, N. Portman, and P. G. McKean. Swimming with protists: Perception, motility and flagellum assembly. *Nature Rev. Microbiol.*, 6:838–850, 2008.

[16] K. F. Jarrell and M. J. McBride. The surprisingly diverse ways that prokaryotes move. *Nature Rev. Microbiol.*, 6:466–476, 2008.

[17] M-J Kim, A. A. Julius, and E. Steager. *Microbiorobotics.* Micro & Nano Technologies Series. Elsevier, 2012.

[18] N. Cohen and J. H. Boyle. Swimming at low Reynolds number: A beginners guide to undulatory locomotion. *Contemp. Phys.*, 51:103–123, 2010.

[19] D. B. Dusenbury. *Living at Micro Scale: The Unexpected Physics of Being Small.* Harvard University Press, 2009.

[20] G. J. Hancock. The self-propulsion of microscopic organisms through liquids. *Proc. R. Soc. A*, 216:96–120, 1953.

[21] J. Gray. The movement of sea-urchin spermatozoa. *J. Exp. Biol.*, 32:775–801, 1955.

[22] J. Lighthill. Flagellar Hydrodynamics. *SIAM Review*, 18(2):161–230, 1976. doi: 10.1137/1018040.

[23] J. J. Blum and J. Lubliner. Biophysics of flagellar motility. *Ann. Rev. Biophys. Bioeng*, 2:181–219, 1973.

[24] G. K. Batchelor. Slender-body theory for particles of arbitrary cross-section in Stokes flow. *J. Fluid Mech.*, 44, 419-440.

[25] R. G. Cox. The motion of long slender bodies in a viscous fluid Part 1. General theory. *J. Fluid Mech.*, 44:791–810, 1970.

[26] R. E. Johnson. An improved slender-body theory for Stokes flow. *J. Fluid Mech.*, 99:411–431, 1980.

[27] B. Rodenborn, C.-H. Chen, H. L Swinney, B. Lui, and H. P. Zhang. Propulsion of microorganisms by a helical flagellum. *Proc. Natl. Acad. Sci. USA*, 110:E338–E347, 2013.

[28] R. E. Johnson and C. J. Brokaw. Flagellar hydrodynamics. A comparison between resistive-force theory and slender-body theory. *Biophys. J.*, 25:113–127, 1979.

[29] T. S. Yu, E. Lauga, and A. E. Hosoi. Experimental investigations of elastic tail propulsion at low Reynolds number. *Phys. Fluids*, 18:091701, 2006.

[30] B. M. Friedrich, I. H. Riedel-Kruse, J. Howard, and F. Julicher. High-precision tracking of sperm swimming fine structure provides strong test of resistive force theory. *J. Exp. Biol.*, 213:1226–1234, 2010.

[31] R. S. Berman, O. Kenneth, J. Sznitman, and A. M. Leshansky. Undulatory locomotion of finite filaments: Lessons from *C. elegans*. *New J. Phys.*, 15:075022, 2013.

[32] T. D. Montenegro-Johnson and E. Lauga. Optimal swimming of a sheet. *Phys. Rev. E*, 89:060701, 2014.

[33] L. J. Fauci and R. Dillon. Biofluidmechanics of reproduction. *Annu. Rev. Fluid Mech.*, 38:371–94, 2006.

[34] S. Y. Reigh, R. G. Winkler, and G. Gompper. Synchronization, slippage, and unbundling of driven helical flagella. *PLoS ONE*, 8(8):e70868, 2013.

[35] S. S. Suarez and A. A. Pacey. Sperm transport in the female reproductive tract. *Human. Reprod. Update*, 12:23–37, 2006.

[36] W. B. Wood. The Left–Right Polarity Puzzle: Determining Embryonic Handedness. *PLoS Biol.*, 3(8):e292, 2005.

[37] M. A. Sleigh, J. R. Blake, and N. Liron. The propulsion of mucus by cilia. *Am. Rev. Respir. Dis.*, 137:726–741, 1988.

[38] D. Bray. *Cell Movements*. Garland Publishing, 2000.

[39] S. Camalet and F. Jülicher. Physical aspects of axonemal beating and swimming. *New J. Phys.*, 2:24, 2000.

[40] R. Phillips, J. Kondev, J. Theriot, and H. G. Garcia. *Physical Biology of the Cell*. Garland Science, 2nd edition, 2012.

[41] S. L. Tamm. Ciliary motion in *Paramecium* : A scanning electron microscope study. *J. Cell Biol.*, 55(1):250–255, 1972.

[42] D. M. Woolley, R. F. Crockett, W. D. I. Groom, and S. D. Revell. A study of synchronisation between the flagella of bull spermatozoa, with related observations. *J. Exp. Biol.*, 212:2215–2223, 2009.

[43] E. A. Gaffney, H. Gadêlha, D. J. Smith, J. R. Blake, and J. C. Kirkman-Brown. Mammalian sperm motility: Observation and theory. *Annu. Rev. Fluid Mech.*, 43:501–28, 2011.

[44] E. Lauga. Propulsion in a viscoelastic fluid. *Phys. Fluids*, 19:083104, 2007.

[45] G. J. Elfring and E. Lauga. Hydrodynamic phase locking of swimming microorganisms. *Phys. Rev. Lett.*, 103:088101, 2009.

[46] S. Camalet, F. Jülicher, and J. Prost. Self-organized beating and swimming of internally driven filaments. *Phys. Rev. Lett.*, 82:1590, 1998.

[47] K. E. Machin. Wave propagation along flagella. *J. Exp. Biol.*, 35:796–806, 1958.

[48] R. H. Dillon and L. J. Fauci. An Integrative model of internal axoneme mechanics and external fluid dynamics in ciliary beating. *J. Theor. Biol.*, 207(3):415–430, 2000.

[49] C. J. Brokaw. Thinking about flagella oscillation. *Cell Motil. Cytoskel.*, 66:425–436, 2009.

[50] E. Lauga and C. Eloy. Shape of optimal active flagella. *J. Fluid Mech.*, 730, 2013.

[51] R. E. Goldstein, E. Lauga, A. I. Pesci, and M. R. E. Proctor. Elastohydrodynamic synchronization of adjacent beating flagella. *Phys. Rev. Fluids*, 1:073201, 2016.

[52] H. C. Fu, C. W. Wolgemuth, and T. R. Powers. Swimming speeds of filaments in nonlinearly viscoelastic fluids. *Phys. Fluids*, 21:033102, 2009.

[53] J. Sznitman, P. K. Purohit, P. Krajacic, T. Lamitina, and P. E. Arratia. Material properties of *Caenorhabditis elegans* swimming at low Reynolds number. *Biophys. J.*, 98:617–626, 2010.

[54] D. J. Smith, E. A. Gaffney, H. Gadêlha, N. Kapur, and J. C. Kirkman-Brown. Bend propagation in the flagella of migrating human sperm, and its modulation by viscosity. *Cell Motil. Cytoskeleton*, 66(4):220–36, 2009.

[55] A. A. Evans and E. Lauga. Fluid transport by active elastic membranes. *Phys. Rev. E*, 84:031924, February 2011.

[56] F. F. V. Chevance and K. T. Hughes. Coordinating assembly of a bacterial macromolecular machine. *Nature Rev. Microbiol.*, 6(6):455–465, 2008.

[57] D. Murat, M. Hérisse, L. Espinosa, A. Bossa, F. Alberto, and L.-F. Wu. Opposite and coordinated rotation of amphitrichous flagella governs oriented swimming and reversals in a magnetotactic *Spirillum*. *J. Bacteriol.*, 197:3275–3282, 2015.

[58] P. H. Raven and G. B. Johnson. *Part IX Viruses and Simple Organisms*. McGraw-Hill, 6th edition edition, 2002.

[59] B. E. Schirrmeister, de Vos Jurriaan M., A. Antonelli, and H. C. Bagheri. Evolution of multicellularity coincided with increased diversification of cyanobacteria and the Great Oxidation Event. *Proc. Nati. Acad. Sci. USA*, 110(5):1791–1796, 2013.

[60] A. Persat, C. D. Nadell, M. K. Kim, F. Ingremeau, A. Siryaporn, K. Drescher, N. S. Wingreen, B. L. Bassler, Z. Gitai, and H. A. Stone. The Mechanical World of Bacteria. *Cell*, 161(5):988–997, 2017.

[61] E. Lauga. Bacterial Hydrodynamics. *Annu. Rev. Fluid Mech.*, 48:105–130, 2016.

[62] S. Namdeo, S. N. Khaderi, and P. R. Onck. Numerical modelling of chirality-induced bi-directional swimming of artificial flagella. *Proc. Roy. Soc. A*, 470:0547, 2013.

[63] S. M. Block, D. F. Blair, and H. C. Berg. Compliance of bacterial optical polyhooks measured with tweezers. *Cytometry*, 12:492–496, 1991.

[64] F. A. Samatey, H. Matsunami, K. Imada , S. Nagashima, T. R. Shaikh, D. R. Thomas, J. Z. Chen, D. J. DeRosier, A. Kitao, and K. Namba. Structure of the bacterial flagellar hook and implication for the molecular universal joint mechanism. *Nature*, 431(7012):1062–1068, 2004.

[65] L. Turner, W. S. Ryu, and H. C. Berg. Real-time imaging of fluorescent flagellar filaments. *J. Bacteriol.*, 182(10):2793–2801, 2000.

[66] N. C. Darnton and H. C. Berg. Force-extension measurements on bacterial flagella: Triggering polymorphic transformations. *Biophys. J.*, 92(6):2230–2236, 2006.

[67] K. Son, D. R. Brumley, and R. Stocker. Live from under the lens: exploring microbial motility with dynamic imaging and microfluidics. *Nat. Rev. Micro.*, 13(12):761–775, 2015.

[68] S. B. Guttenplan, S. Shaw, and D. B. Kearns. The cell biology of peritrichous flagella in *Bacillus subtilis*. *Mol. Microbiol.*, 87(1):211–229, 2012.

[69] L. Ping. The asymmetric flagellar distribution and motility of *Escherichia coli*. *J. Mol. Biol*, 397:906–916, 2010.

[70] P. J. Mears, S. Koirala, C. V. Rao, I. Golding, and Y. R. Chemla. Escherichia coli swimming is robust against variations in flagellar number. *eLife*, 3:e01916, 2013.

[71] B. Scharf. Real-time imaging of fluorescent flagellar filaments of *Rhizobium lupini* H13-3: Flagellar rotation and pH-induced polymorphic transitions. *J. Bacteriol.*, 184(21):5979–5986, 2002.

[72] N. C. Darnton, L. Turner, S. Rojevsky, and H. C. Berg. On torque and tumbling in swimming *Escherichia coli*. *J. Bacteriol.*, 189(5):1756–1764, 2007. 10.1128/JB.01501-06.

[73] J. B. Keller and S. I. Rubinow. Swimming of flagellated microorganisms. *Biophys. J.*, 16(2 Pt 1):151–170, 1976.

[74] S. Chattopadhyay, R. Moldovan, C. Yeung, and X. L. Wu. Swimming efficiency of bacterium *Escherichia coli*. *Proc. Nati. Acad. Sci. USA*, 103(37):13712–13717, 2006.

[75] Y. Hyon, T. R. Powers, R. Stocker, and H. C. Fu. The wiggling trajectories of bacteria. *J. Fluid Mech.*, 705:58–76, 2012.

[76] M. Kong, Y. Wu, G. Li, and R. G. Larson. A bead-spring model for running and tumbling of flagellated swimmers: Detailed predictions compared to experimental data for *E. coli*. *Soft Matter*, (11):1572–1581, 2015.

[77] J. Hu, M. Yang, G. Gompper, and R. G. Winkler. Modelling the mechanics and hydrodynamics of swimming *E. coli*. *Soft Matter*, (11):7867–7876.

[78] P. Kanehl and T. Ishikawa. Fluid mechanics of swimming bacteria with multiple flagella. *Phys. Rev. E*, 89(4):042704, 2014.

[79] M. T. Brown, B. C. Steel, C. Silvestrin, D. A. Wilkinson, N. J. Delalez, C. N. Lumb, B. Obara, J. P. Armitage, and R. M. Berry. Flagellar hook flexibility is essential for bundle formation in swimming *Escherichia coli* cells. *J. Bacteriol.*, 194(13):3495–3501, 2012.

[80] M. Kim, J. C. Bird, A. J. Van Parys, K. S. Breuer, and T. R. Powers. A macroscopic scale model of bacterial flagellar bundling. *Proc. Nati. Acad. Sci. USA*, 100(26):15481–15485, 2003.

[81] H. Shum and E. A. Gaffney. The effects of flagellar hook compliance on motility of monotrichous bacteria: A modeling study. *Phys. Fluids*, 24(6):061901, 2012.

[82] K. Son, J. S. Guasto, and R. Stocker. Bacteria can exploit a flagellar buckling instability to change direction. *Nature Physics*, 9:494–498, 2013.

[83] F. A. Morrison. *Understanding Rheology*. Oxford University Press, 2001.

[84] J. R. Vélez-Cordero and E. Lauga. Waving transport and propulsion in a generalized Newtonian fluid. *J. Non-Newt. Fluid Mech.*, 199:37–50, 2013.

[85] M. Pakpour. *Rheology of Dry, Partially Saturated and Wet Granular Materials*. PhD thesis, Faculty of Science, University of Amsterdam, 2013.

[86] A. Borzacchiello, L. Ambrosio, P. Netti, and L. Nicolais. *Rheology of Biological Fluids and Their Substitues*. Marcel Dekker, Inc, 2004.

[87] N. Phan-Thien. *Understanding Viscoelasticity: An Introduction to Rheology*. Graduate Texts in Physics. Springer, 2012.

[88] H. R. Wallace. The dynamics of nemotode movement. *Annu. Rev. Phytopathol*, 6:91–114, 1967.

[89] C. Josenhans and S. Suerbaum. The role of motility as a virulence factor in bacteria. *Int. J. Med. Microbiol.*, 291:605–614, 2002.

[90] R. P. Chhabra. *Bubbles, Drops and Particles in non-Newtonian Fluids*. Taylor & Francis Group, LLC, 2007.

[91] D. Rodrigue, D. de Kee, and C. F. Chan Man Fong. The slow motion of a spherical particle in a Carreau fluid. *Chem. Eng. Comm.*, 154:203–215, 1996.

[92] S. W. Hopke and Slattery J. C. Upper and lower bounds on the drag coefficient of a sphere in an Ellis model fluid. *AIChE J.*, 16:224, 1970.

[93] M. B. Bush and N. Phan-Thien. Drag force on a sphere in creeping motion through a Carreau model fluid. *J. Non-Newt. Fluid Mech.*, 16:303–313, 1984.

[94] R. I. Tanner. Stokes paradox for a power-law fluid around a cylinder. *J. Non-Newt. Fluid Mech.*, 506:217–224, 1993.

[95] J-P. Hsu, C-F. Shie, and S. Tseng. Sedimentation of a cylindrical particle in a Carreau fluid. *J. Colloid Interf. Sci.*, 286:392–399, 2005.

[96] I. Machač, S. Bedřich, and R. Teichman. Fall of non-spherical particles in a Carreau model liquid. *Chem. Eng. Process*, 41:577–584, 2002.

[97] R. P. Chhabra, K. Rami, and P. H. T. Uhlherr. Drag on cylinders in shear thinning viscoelastic liquids. *Chem. Eng. Sci.*, 56:2221–2227, 2001.

[98] K. Cho and Y. I. Cho. Hydrodynamics of a vertically falling thin cylinder in non-Newtonian fluids. *J. Non-Newt. Fluid Mech.*, 45:105–145, 1992.

[99] N. A. Park and T. F. Irvine Jr. Measurements of rheological fluid properties with the falling needle viscometer. *Rev. Sci. Instrum.*, 59:2051–2058, 1988.

[100] O. Manero, B. Mena, and L. de Vargas. A note on the translation of a thin rod inside a cylinder. *Rheol. Acta*, 26:266–271, 1987.

[101] A. Unnikrishnan and R. P. Chhabra. Slow parallel motion of cylinders in non-Newtonian media: Wall effects and drag coefficient. *Chem. Eng. Process*, 286:121–125, 1990.

[102] S. H. Lee and L. G. Leal. Low-Reynolds-number flow past cylindrical bodies of arbitrary cross-sectional shape. *J. Fluid Mech.*, 164:401–427, 1986.

[103] J. R. Vélez-Cordero, D. Sámano, P. Yue, J. J. Feng, and R. Zenit. Hydrodynamic interaction between a pair of bubbles ascending in shear-thinning inelastic fluids. *J. Non-Newt. Fluid Mech.*, 166:118–132, 2011.

[104] H. C. Fu, V. B. Shenoy, and T. R. Powers. Low-Reynolds number swimming in gels. *Europhys. Lett.*, 91:24002, 2010.

[105] D. R. Hewitt and N. J. Balmforth. Taylor's swimming sheet in a yield-stress fluid. *J. Fluid Mech.*, under review.

[106] Y. Man and E. Lauga. Phase-separation models for swimming enhancement in complex fluids. *Phys. Rev. E*, 92:023004, 2015.

[107] Z. Peng, O. S. Pak, and G. J. Elfring. Characteristics of undulatory locomotion in granular media. *Phys. Fluids*, 28(3):031901, 2016.

[108] A. T. Brown, I. D. Vladescu, A. Dawson, T. Vissers, J. Schwarz-Linek, J. S. Lintuvuori, and W. C. K. Poon. Swimming in a crystal. *Soft Matter*, 12(1):131–140, 2016.

[109] M. Jabbarzadeh, Y. Hyon, and H. C. Fu. Swimming fluctuations of micro-organisms due to heterogeneous microstructure. *Phys. Rev. E*, 90:043021, 2014.

[110] M. Dasgupta, B. Liu, H. C. Fu, M. Berhanu, K. S. Breuer, T. R. Powers, and A. Kudrolli. Speed of a swimming sheet in Newtonian and viscoelastic fluids. *Phys. Rev. E*, 87:013015, 2013.

[111] J. Espinosa-Garcia, E. Lauga, and R. Zenit. Fluid elasticity increases the locomotion of flexible swimmers. *Phys. Fluids*, 25:031701, 2013.

[112] X. Shen and P. E. Arratia. Undulatory swimming in viscoelastic fluids. *Phys. Rev. Lett.*, 106:208101, 2011.

[113] B. Qin, A. Gopinath, J. Yang, J. P. Gollub, and P. E. Arratia. Flagellar kinematics and swimming of algal cells in viscoelastic fluids. *Scientific Reports*, 5:9190, 2015.

[114] B. Liu, T. R. Powers, and K. S. Breuer. Force-free swimming of a model helical flagellum in viscoelastic fluids. *Proc. Natl. Acad. Sci. USA*, 108:19516–19520, 2011.

[115] A. E. Patteson, A. Gopinath, M. Goulian, and P. E. Arratia. Running and tumbling with *E. coli* in polymeric solutions. *Scientific Reports*, 5:15761, 2015.

[116] V. A. Martinez, J. Schwarz-Linek, M. Reufer, L. G. Wilson, A. N. Morozov., and W. C. K. Poon. Flagellated bacterial motility in polymer solutions. *Proc. Nati. Acad. Sci. USA*, 111(50):17771–17776, 2014.

[117] S. E. Spagnolie, B. Liu, and T. R. Powers. Locomotion of helical bodies in viscoelastic fluids: Enhanced swimming at large helical amplitudes. *Phys. Rev. Lett.*, 111:068101, 2013.

[118] L. Zhu, M. Do-Quang, E. Lauga, and L. Brandt. Locomotion by tangential deformation in a polymeric fluid. *Phys. Rev. E*, 83:011901, 2011.

[119] L. Zhu, E. Lauga, and L. Brandt. Self-propulsion in viscoelastic fluids: Pushers vs. pullers. *Phys. Fluids*, 24:051902, 2012.

[120] M. P. Curtis and E. A. Gaffney. Three-sphere swimmer in a nonlinear viscoelastic medium. *Phys. Rev. E*, 87:043006, 2013.

[121] T. Normand and E. Lauga. Flapping motion and force generation in a viscoelastic fluid. *Phys. Rev E*, 78:061907, 2008.

[122] O. S. Pak, L. Zhu, L. Brandt, and E. Lauga. Micropropulsion and microrheology in complex fluids via symmetry breaking. *Phys. Fluids*, 24:103102, 2012.

[123] E. Lauga. Life at high Deborah number. *Europhys. Lett.*, 86:64001, 2009.

[124] E. Lauga. Life around the scallop theorem. *Soft Matter*, 7:3060–3065, 2011.

[125] J. C. Chrispell, L. J. Fauci, and M. Shelley. An actuated elastic sheet interacting with passive and active structures in a viscoelastic fluid. *Phys. Fluids*, 25:013103, 2013.

[126] J. Teran, L. Fauci, and M. Shelley. Viscoelastic fluid response can increase the speed and efficiency of a free swimmer. *Phys. Rev. Lett.*, 104:038101, 2010.

[127] B. Thomases and R. D. Guy. Mechanisms of elastic enhancement and hindrance for finite-length undulatory swimmers in viscoelastic fluids. *Phys. Rev. Lett.*, 113:098102, 2014.

[128] G. R. Fulford, D. F. Katz, and R. L. Powell. Swimming of spermatozoa in a linear viscoelastic fluid. *Biorheology*, 35:295–309, 1998.

[129] H. C. Fu, T. R. Powers, and C. W. Wolgemuth. Theory of swimming filaments in viscoelastic media. *Phys. Rev. Lett.*, 99:258101, 2007.

[130] E. E. Riley and E. Lauga. Small-amplitude swimmers can self-propel faster in viscoelastic fluids. *J. Theor. Biol.*, 382:345–355, 2015.

[131] G. J. Elfring and G. Goyal. The effect of gait on swimming in viscoelastic fluids. *J. Non-Newt. Fluid Mech.*, 234:8–14, 2016.

[132] E. E. Riley and E. Lauga. Enhanced active swimming in viscoelastic fluids. *Europhys. Lett.*, 108:34003, 2014.

[133] G. J. Elfring, O. S. Pak, and E. Lauga. Two-dimensional flagellar synchronization in viscoelastic fluids. *J. Fluid Mech.*, 646:505–515, 2010.

[134] E. J. Hemingway, A. Maitra, S. Banerjee, M. C. Marchetti, S. Ramaswamy, S. M. Fielding, and M. E. Cates. Active viscoelastic matter: From bacterial drag reduction to turbulent solids. *Phys. Rev. Lett.*, 114:098302, 2015.

[135] G. Li and A. M. Ardekani. Collective motion of microorganisms in a viscoelastic fluid. *Phys. Rev. Lett.*, 117:118001, 2016.

[136] C. Datt, L. Zhu, G. J. Elfring, and O. S. Pak. Squirming through shear-thinning fluids. *J. Fluid Mech.*, 784:R1, 2015.

[137] T. D. Montenegro-Johnson, D. J. Smith, and D. Loghin. Physics of rheologically-enhanced propulsion: Different strokes in generalized Stokes. *Phys. Fluids*, 25:081903, 2013.

[138] G. Li and A. M. Ardekani. Undulatory swimming in non-Newtonian fluids. *J. Fluid Mech.*, 784(R4), 2015.

[139] E. E. Riley and E. Lauga. Empirical resistive-force theory for slender biological filaments in shear-thinning fluids. *Phys. Rev. E*, accepted, 2017.

[140] N. Ali, Z. Asghar, O. Anwar Bég, and M. Sajid. Bacterial gliding fluid dynamics on a layer of non-Newtonian slime: Perturbation and numerical study. *J. Theor. Biol.*, 397:22–32, 2016.

[141] A. J. T. M. Mathijssen, T. N. Shendruk, J. M. Yeomans, and A. Doostmohammadi. Upstream Swimming in Microbiological Flows. *Phys. Rev. Lett.*, 116:028104, 2016.

[142] D. A. Gagnon, X. N. Shen, and P. E. Arratia. Undulatory swimming in fluids with polymer networks. *Europhys. Lett.*, 104:14004, 2013.

[143] D. A. Gagnon, N. C. Keim, and P. E. Arratia. Undulatory swimming in shear-thinning fluids: Experiments with *Caenorhabditis elegans*. *J. Fluid Mech.*, 758:758, 2014.

[144] D. A. Gagnon and P. E. Arratia. The cost of swimming in generalized Newtonian fluids: Experiments with *C. elegans*. *J. Fluid Mech.*, 800:753–765, 2016.

[145] J-S. Park, D. Kim, J. H. Shin, and D. A. Weitz. Efficient nematode swimming in a shear thinning colloidal suspension. *Soft Matter*, 12:1892, 2016.

[146] S. Gomez, F. Godinez, E. Lauga, and R. Zenit. Helical propulsion in shear-thinning fluids. *J. Fluid Mech.*, 812:R3, 2016.

[147] G. Li and A. M. Ardekani. Undulatory swimming in non-Newtonian fluids. *J. Fluid Mech.*, 784:R4, 2015.

[148] T. Zhang and D. I. Goldman. The effectiveness of resistive force theory in granular locomotion. *Phys. Fluids*, 26:101308, 2014.

[149] S. Kim and S. J. Karrila. *Microhydrodynamics: Principles and Selected Applications*. Butterworth-Heinemann Series in Chemical Engineering. Butterworth-Heinemann, 1991.

[150] B. Tomases and R. D. Guy. Mechanisms of elastic enhancement and hindrance for finite-length undulatory swimmers in viscoelastic fluids. *Phys. Rev. Lett.*, 113:098102, 2014.

[151] S. Childress. *Mechanics of Swimming and Flying*. Cambridge Studies in Mathematical Biology. Cambridge University Press, 1981.

[152] R. Vogel and H. Stark. Motor-driven bacterial flagella and buckling instabilities. *Eur. Phys. J. E*, 35(15), 2012.

[153] T. R. Powers. Role of body rotation in bacterial flagellar bundling. *Phys. Rev. E*, 65:040903, 2002.

[154] J. Yang, C. W. Wolgemuth, and G. Huber. Kinematics of the swimming of *Spiroplasma*. *Phys. Rev. Lett.*, 102:218102, 2009.

[155] E. Passov and Y. Or. Dynamics of Purcell's three-link microswimmer with a passive elastic tail. *Eur. Phys. J. E*, 35:78, 2012.

[156] Marcos, H. C. Fu, T. R. Powers, and R. Stocker. Separation of microscale chiral objects by shear flow. *Phys. Rev. Lett.*, 102:158103, 2009.

[157] M. K. Kim, K. Drescher, O. S. Pak, B. L. Bassler, and H. A. Stone. Filaments in curved streamlines: Rapid formation of *Staphylococcus aureus* biofilm streamers. *New J. Phys.*, 16:065024, 2014.

[158] J. G. Oldroyd. On the formulation of rheological equations of state. *Proc. R. Soc. London Ser. A*, 200:523, 1950.

[159] B. Liu, T. R. Powers, and K. S. Breuer. Force-free swimming of a model helical flagellum in viscoelastic fluids. *PNAS*, 108:19516, 2011.

[160] D. A. Gagnon, N. C. Keim, X. Shen, and P. E. Arratia. Fluid-induced propulsion of rigid particles in wormlike micellar solutions. *Phys. Fluids*, 26:103101, 2014.

[161] S. Alben and M. Shelley. Coherent locomotion as an attracting state for a free flapping body. *Proc. Natl. Acad. Sci. USA*, 102:11163–11166, 2004.

[162] N. Vandenberghe, J. Zhang, and S. Childress. Symmetry breaking leads to forward flapping flight. *J. Fluid Mech.*, 506:147–155, 2004.

[163] E. Lauga. Continuous breakdown of Purcell's scallop theorem with inertia. *Phys. Fluids*, 19:061703, 2007.

[164] S. Wang and A. Ardekani. Inertial squirmer. *Phys. Fluids*, 24:101902, 2012.

[165] A. S. Khair and N. G. Chisholm. Expansions at small Reynolds numbers for the locomotion of a spherical squirmer. *Phys. Fluids*, 26:011902, 2014.

[166] D. R. Brumley, K. Y. Wan, M. Polin, and R. E. Goldstein. Flagellar synchronization through direct hydrodynamic interactions. *eLife*, 3:e02750, 2014.

[167] Y. Yang and X. Lu. *Drosophila sperm* motility in the reproductive tract. *Biol. Reprod.*, 84:1005–1015, 2011.

[168] C. H. Wiggins and R. E. Goldstein. Flexive and propulsive dynamics of elastica at low Reynolds number. *Phys. Rev. Lett.*, 80, 1998.

[169] I. H. Reidel-Kruse, A. Hilfinger, J. Howard, and F. Jülicher. How molecular motors shape the flagellar beat. *HFSP J.*, 1(3):192–208, 2007.

[170] S. S. Suarez, D. F. Katz, D. H. Owen, J. B. Andrew, and R. L. Powell. Evidence for the function of hyperactivated motility in sperm. *Biol. Reprod*, 44:375, 1991.

[171] P. V. Bayly and K. S. Wilson. Analysis of unstable modes distinguishes mathematical models of flagellar motion. *J. R. Soc. Interface*, 12:0124, 2015.

[172] R. Ma, G. S. Klindt, I. H. Riedel-Kruse, F. Jülicher, and B. M. Friedrich. Active phase and amplitude fluctuations of flagellar bending. *Phys. Rev. Lett.*, 113:048101, 2014.

[173] J. S. Guasto, K. A. Johnson, and J. P. Gollub. Oscillatory flows induced by microorganisms swimming in two dimensions. *Phys. Rev. Lett.*, 105:168102, 2010.

[174] G. J. Elfring. *Symmetry Breaking and Synchronization at Small Scales*. PhD thesis, Engineering Sciences (Mechanical Engineering), 2012.

[175] C. J. Brokaw. Direct measurements of sliding between outer doublet microtubulesin swimming sperm flagella. *Science*, 243:1593, 1989.

[176] H. C. Fu, C. W. Wolgemuth, and T. R. Powers. Beating patterns of filaments in viscoelastic fluids. *Phys. Rev. E*, 78:041913, 2008.

[177] H. C. Berg. *E. coli in Motion*. Biological and Medical Physics, Biomedical Engineering. Springer-Verlag New York, 1 edition, 2004.

[178] G. N. Cohen-Ben-Lulu, N. R. Francis, E. Shimoni, D. Noy, Y. Davidov, K. Prasad, Y. Sagi, G. Cecchini, R. M. Johnstone, and M. Eisenbach. The bacterial flagellar switch complex is getting more complex. *EMBO J.*, 27(7012):1134–44, 2008.

[179] Marcos. *Bacteria in shear flow*. PhD thesis, Dept. of Mechanical Engineering., 2011.

[180] Y. Sowa and R. M. Berry. Bacterial flagellar motor. *Q. Rev. Biophys.*, 41(2):103–132, 2008.

[181] A. Sen, R. K. Nandy, and A. N. Ghosh. Elasticity of flagellar hooks. *J. Electron Microsc.*, 53(3):305–309, 2004.